

Designed scattering by composite nanostructures

How to design a nanostructure to scatter light in the direction you want

Kotte, T.P.S.

DOI

[10.4233/uuid:e72c7add-e137-438e-946a-9c614d9c60a3](https://doi.org/10.4233/uuid:e72c7add-e137-438e-946a-9c614d9c60a3)

Publication date

2025

Document Version

Final published version

Citation (APA)

Kotte, T. P. S. (2025). *Designed scattering by composite nanostructures: How to design a nanostructure to scatter light in the direction you want*. [Dissertation (TU Delft), Delft University of Technology]. <https://doi.org/10.4233/uuid:e72c7add-e137-438e-946a-9c614d9c60a3>

Important note

To cite this publication, please use the final published version (if applicable). Please check the document version above.

Copyright

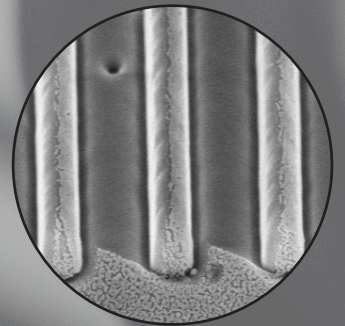
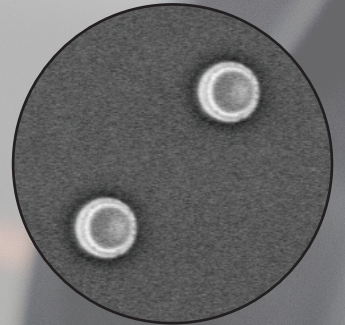
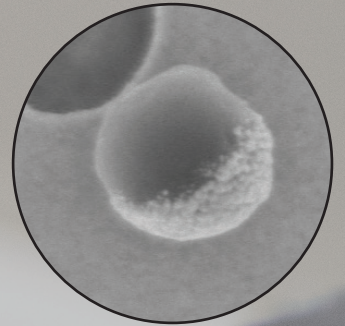
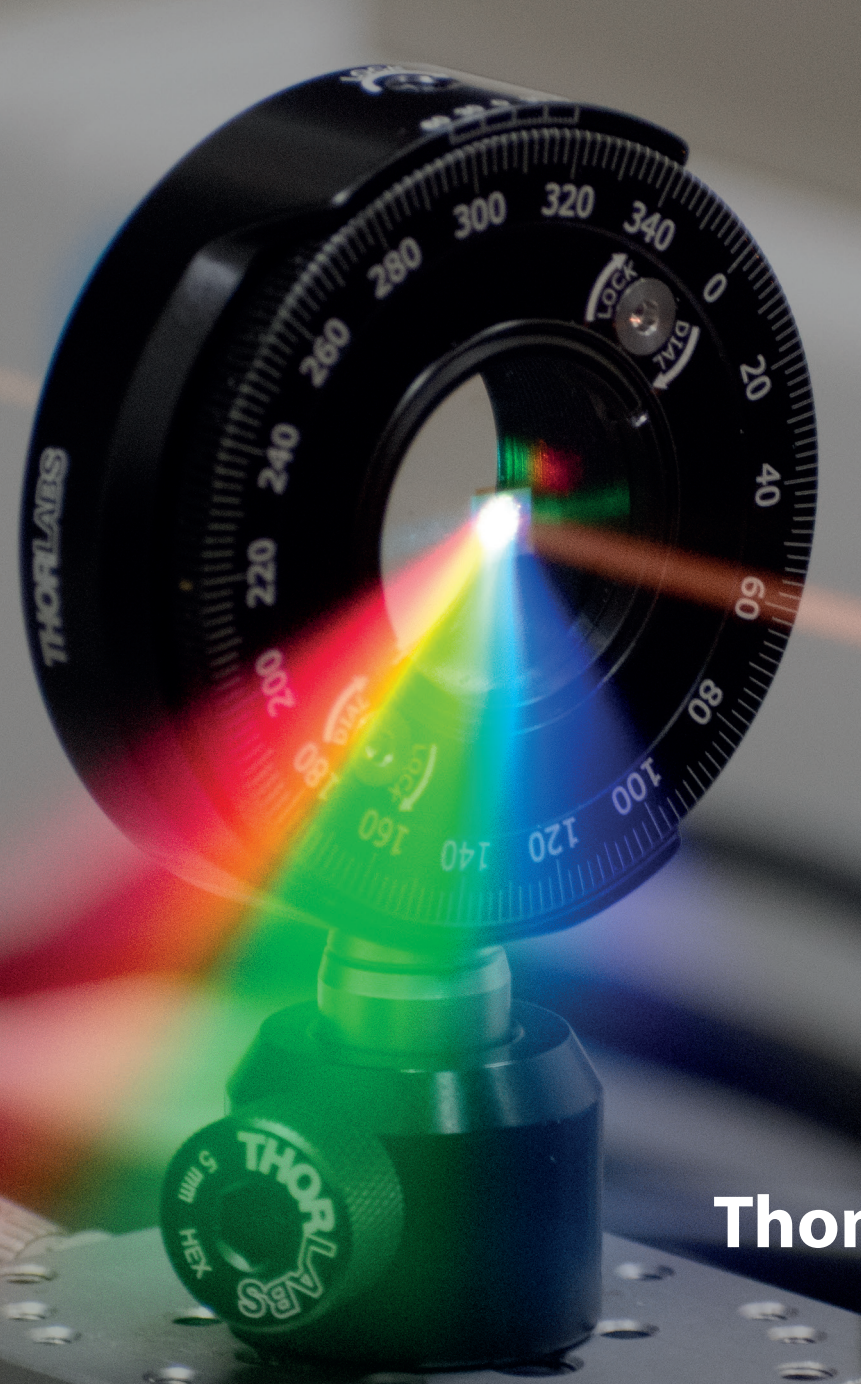
Other than for strictly personal use, it is not permitted to download, forward or distribute the text or part of it, without the consent of the author(s) and/or copyright holder(s), unless the work is under an open content license such as Creative Commons.

Takedown policy

Please contact us and provide details if you believe this document breaches copyrights. We will remove access to the work immediately and investigate your claim.

Designed scattering by composite nanostructures

How to design a nanostructure to scatter light in the direction you want



Thomas Kotte

DESIGNED SCATTERING BY COMPOSITE NANOSTRUCTURES

HOW TO DESIGN A NANOSTRUCTURE TO SCATTER LIGHT IN
THE DIRECTION YOU WANT

DESIGNED SCATTERING BY COMPOSITE NANOSTRUCTURES

HOW TO DESIGN A NANOSTRUCTURE TO SCATTER LIGHT IN
THE DIRECTION YOU WANT

Dissertation

for the purpose of obtaining the degree of doctor
at Delft University of Technology
by the authority of the Rector Magnificus Prof.dr.ir. T.H.J.J. van der Hagen;

Chair of the Board for Doctorates
to be defended publicly on
Wednesday 3 December 2025 at 10:00 o'clock

by

Thomas Pieter Sebastiaan KOTTE

Master of Science in Applied Physics, Delft University of Technology, the Netherlands
born in Zwolle, the Netherlands.

This dissertation has been approved by the promotor.

Composition of the doctoral committee:

Rector Magnificus,	chairperson
Em. prof. dr. H.P. Urbach,	Delft University of Technology, promotor
Dr. A.J.L. Adam,	Delft University of Technology, copromotor

Independent members:

Dr. I.Z. Esmail Zadeh	Technische Universiteit Delft
Prof. dr. ir. T. Van der Sar	Technische Universiteit Delft
Prof. dr. W.L. Vos	Universiteit Twente
Dr. Z. Xi	University of Science and Technology of China
Prof. dr. A.F. Koenderink	AMOLF
Prof. dr. W.M.J.M. Coene	Technische Universiteit Delft, reserve member



Keywords: scattering, directional scattering, Mie theory, resonant photonics, nanofabrication, diffraction gratings, Monte Carlo simulations

Printed by: Ridderprint | www.ridderprint.nl

Front & Back: Photo of the measurement of a transmission grating. Inset are some SEM photos of the nanostructures that were fabricated as part of this thesis.

Copyright © 2025 by T.P.S. Kotte

ISBN 978-94-6384-880-0

An electronic version of this dissertation is available at
<http://repository.tudelft.nl/>.

CONTENTS

Summary	vii
Samenvatting	xi
1 Introduction	1
1.1 Manipulation of light	1
1.2 Nanoparticles in physics, chemistry and biology	3
1.3 Outline of the thesis.	4
2 Solving scattering problems	5
2.1 All about cross sections	6
2.2 The Lippmann-Schwinger integral equation	8
2.3 Mie theory	11
2.4 Transfer matrix method	16
2.5 Finite element methods.	20
2.6 Multipole analysis.	21
2.6.1 Exact multipolar decomposition	21
2.6.2 The decomposed discrete dipole approximation.	24
2.6.3 Mixing of multipole contributions	24
2.7 Summary	25
3 Directional scattering by nanostructures	27
3.1 Scattering properties of nanoparticles	28
3.1.1 Effect of different materials	28
3.1.2 Effect of size	32
3.1.3 Effect of geometry	34
3.2 Scattering properties of composite nanoparticles.	38
3.2.1 Coreshell nanoparticles	40
3.2.2 Core-semishell nanoparticles	44
3.2.3 Other geometries	50
3.3 Directional scattering and gratings	50
3.3.1 Metal composite elements	55
3.3.2 Embedded composite gratings.	58
3.4 Summary and outlook	61
4 Fabrication of composite nanostructures	63
4.1 Colloid nanoparticles	64
4.1.1 Production of core-semishell particles	65
4.1.2 Production of etched composite nanoparticles	70
4.2 Fabrication of gratings	72
4.3 Summary and outlook	83

5	Measurements of scattering composite nanostructures	85
5.1	Measurement setup for single nanoparticles	86
5.2	Postprocessing of measurements	88
5.3	Measurements of composite nanoparticles	90
5.4	Grating measurement setup	93
5.5	Grating measurement results	94
5.5.1	Polarization along the grating lines	94
5.5.2	Polarization perpendicular to the grating lines	104
5.6	Summary and outlook	106
6	Volumetric scattering by nanoparticles	107
6.1	Scattering and entropy	108
6.2	Monte-Carlo simulations	111
6.3	Monte-Carlo results	113
6.3.1	Uniform scatterers	113
6.3.2	Directional scatterers	116
6.3.3	Directional scatterers with absorption	119
6.4	Summary and outlook	120
7	Conclusion	121
7.1	Conclusions	121
7.2	Outlook and recommendations	122
A	Mathematical identities and derivations	125
A.1	Vector identities and tensors	125
A.2	Derivation of the 3D Greens function for a dipole	125
A.3	Electric field of a general current distribution	127
A.4	Far field approximation	127
A.5	Vector spherical harmonics	128
A.6	Lorentz reciprocity	129
A.7	Electric and magnetic octupole expressions	130
B	FEM simulations using COMSOL	135
B.1	Modelling of core-shell particles	135
B.2	COMSOL modelling of core-semishell particles	137
B.3	Modelling of a composite nanoparticle on a substrate	137
B.4	Grating simulations	140
B.4.1	Simulations of a single grating element	140
B.4.2	Simulations of gratings	142
	Acknowledgements	143
	List of Publications	145
	Data availability	147
	References	149
	Curriculum Vitae	157

SUMMARY

Traditionally, lenses and mirror are used to manipulate light. Using the principles of reflection and refraction, light can be redirected. Lenses can be used to focus light down to a spot or for imaging, while mirrors can be used to redirect the light.

A more advanced method of redirecting light is by the use of a diffraction grating. Such a grating consists of a pattern of closely spaced grooves that redirects the light into specific directions depending on the color of the light. A transmission grating for example, redirects red light at a larger angle than blue light. Therefore, gratings are often used in spectroscopy to determine the combination of colors a light source is made up of.

SCATTERING OF LIGHT

The scattering of light is caused by the interaction of light with particles that are approximately the same size as the wavelength of the light itself. We see the result of this everyday when observing that the sky is blue. Traditionally, scattering is avoided in optical elements; it is much easier to work with polished materials, where refraction (as in lenses and prisms) and reflection (for mirrors) govern the propagation of light.

When only dealing with refraction and reflection, the propagation of light can then be explained by treating light as rays. The direction of these rays can be derived using the Snell-Descartes Law from high-school physics.

In contrast, scattering is a result of the wave-like nature of light. Generally, this makes the propagation quite hard to predict at a macro scale, where the interaction with many tiny particles or very small surface-irregularities needs to be considered.

In recent decades, however, researchers' focus has shifted from the limitations that scattering imposes to the opportunities it offers. Some things can be achieved through scattering that cannot be achieved without it. Ongoing development of fabrication processes allows for the production of particles smaller than the wavelength of visible light and continuously increasing precision. This allows for the control of the scattering to be within the reach of experimental scientists.

As mentioned before, the color of the sky is due to scattering of light. This can serve as a good example of how scattering works. When light is incident on particles which has approximately the same size as the wavelength of the light, it does not simply get reflected, refracted or transmitted. At this scale, we have to take into account that light is an electromagnetic wave. Particles in the air are made up of molecules containing electrons. These electrons start oscillating due to the electric and magnetic fields of the wave. This oscillation in turn generates electromagnetic waves which travel in different directions. Part of the incoming light is thus redirected in an arbitrary direction.

It turns out that this happens more for light with shorter wavelengths. Then, zooming out to the size of the atmosphere, what do we see? Everywhere in the

atmosphere these tiny particles exist, redirecting part of the light coming from the sun in a random direction. This happens more for light which is towards the blue part of the rainbow than the red part (since blue has a shorter wavelength). As a result, we see blue light coming from everywhere we look in the atmosphere. This effect becomes even more clear during a sunrise or sunset, since the light from the sun needs to travel through a larger part of the atmosphere before it reaches your eyes, more and more of the blue part of the spectrum is stripped away by this scattering resulting in a beautiful red sun just before it dips below the horizon.

DIRECTIONAL SCATTERING

The redirecting of light with small structures has been done for a long time. Often, repeating structures such as gratings are used to redirect light. The repeating structure makes it so that in some directions, the light from the structures interferes constructively, while in other directions destructively. Such structures can be made quite effective, redirecting light into a small cone of angles.

The direction that the light is scattered in, depends on the pitch of the repeating structure compared to the wavelength of the light. As a result, white light that is incident on such a structure would be split up into a rainbow, where each transmitted color has a different direction. This can be both an advantage and a disadvantage: if we would like to know what the spectrum is of a certain light source, a grating would be perfect for that. On the other hand, if we would like to create a lens using these structures, the focus for each color would be at a different position. This creates a problem if such a lens is used for a camera.

For the redirection of light, we consider broadband applications where all colors of (visible) light are used. Therefore, we will initially not consider these repeating structures. Instead, we will consider individual scattering particles, after which we will look at the collective response of these particles. Although the scattering by such particles is known to be determined by the geometry and refractive index of the nanoparticle, the exact relation is not known. Because of this, no method exists to design a nanoparticle such that it scatters light in a particular direction. This thesis will attempt to find such a method. In addition, we will show how a highly efficient grating can be created using the directional scattering of individual particles.

METHODS AND RESULTS OF THIS THESIS

To achieve these goals, we will develop a method for designing a single nanoparticle that scatters in a preferential direction for a broadband spectrum. This method is then used to design a nanoparticle that redirects visible light through scattering. We found that broadband directional scattering can be achieved by combining an absorbing and non-absorbing material in a single nanoparticle. This is due to the introduction of a phase difference in the scattered field by the different materials that make up the nanoparticle.

The nanoparticles are then produced using nanofabrication techniques and measured in the lab to confirm the theory with measurements. For this, we used a design that combines the materials fused silica and gold. We found that the measurements agree with the developed theory.

The theory is also applied to diffraction gratings, where a design is made for a highly efficient transmission diffraction grating. In this case, the grating lines are created by combining glass with a metal or semiconductor material. The gratings are then produced using nanofabrication techniques such as electron beam pattern generation and dry etching. The gratings are then measured and their performance is compared with the theory.

The measurements showed worse performance for the gratings that incorporate metal. This is likely due to the increased absorption in the ultra thin metal layers that were used. For the gratings that are made with titanium nitride, a semiconductor material, we did see the expected enhanced performance.

Finally, we developed a numerical Monte Carlo method to evaluate whether it is possible to create a volume containing nanoparticles that scatters an incident beam of light into a specific direction; the original idea of the PhD project. We found that this is not possible without without significant loss of light, which is undesirable for the applications this idea was aimed for.

SAMENVATTING

Traditioneel worden lenzen en spiegels gebruikt om licht te manipuleren. Door gebruik te maken van de principes van reflectie en breking, kan licht worden gemanipuleerd. Lenzen kunnen worden gebruikt om licht te focussen tot een punt en gebruikt wordt voor beeldvorming, terwijl spiegels kunnen worden gebruikt om het licht van richting te laten veranderen.

Een geavanceerdere methode om licht te manipuleren maakt gebruik van een diffractietralie. Zo'n tralie bestaat uit een patroon van dicht op elkaar geplaatste groeven dat het licht in verschillende richtingen afbuigt, afhankelijk van de kleur van het licht. Bijvoorbeeld: een transmissietralie bijvoorbeeld buigt rood licht af onder een grotere hoek dan blauw licht. Daarom worden tralies vaak in spectroscopie gebruikt om te bepalen uit welke combinatie van kleuren een lichtbron bestaat.

VERSTROOIING VAN LICHT

Verstrooiing van licht wordt veroorzaakt door de interactie van licht met deeltjes die ongeveer even groot zijn als de golflengte van het licht zelf. We zien het resultaat hiervan elke dag: het is de reden waarom de lucht blauw is. Normaliter wordt verstrooiing in de optica vermeden; het is veel eenvoudiger om te werken met gepolijste materialen, waarbij breking (zoals in lenzen en prisma's) en reflectie (zoals bij spiegels) het gedrag van licht bepalen.

Wanneer men zich enkel bezighoudt met breking en reflectie, kan de voortplanting van licht worden verklaard door licht als stralen te beschouwen. De richting van deze stralen kan worden beschreven met de Wet van Descartes-Snellius geleerd op de middelbare school.

Verstrooiing daarentegen is een gevolg van de golfachtige aard van licht. Dit maakt de voortplanting over het algemeen moeilijk te voorspellen op macroschaal, waarbij interactie met veel kleine deeltjes, of zeer kleine oppervlaktestructuren in rekening moet worden gebracht.

Echter, in de afgelopen decennia is de focus van onderzoekers verschoven van de beperkingen die verstrooiing oplegt naar de mogelijkheden die het biedt. Sommige dingen kunnen juist dankzij verstrooiing worden bereikt, die anders onmogelijk zouden zijn. De voortdurende ontwikkeling van fabricagetechnieken maakt het mogelijk om deeltjes te produceren die kleiner zijn dan de golflengte van zichtbaar licht, met een steeds toenemende precisie. Hierdoor komt het beheersen van verstrooiing binnen het bereik van experimentele wetenschappers.

Zoals eerder vermeld, is de kleur van de lucht te danken aan de verstrooiing van licht. Dit kan dienen als een goed voorbeeld van hoe verstrooiing werkt. Wanneer licht deeltjes raakt die ongeveer even groot zijn als de golflengte van het licht, wordt het niet simpelweg gereflecteerd, gebroken of doorgelaten. Op deze schaal moeten

we er rekening mee houden dat licht een elektromagnetische golf is. Deeltjes in de lucht bestaan uit moleculen die elektronen bevatten. Deze elektronen beginnen te trillen onder invloed van de elektrische en magnetische velden van de golf. Deze trilling genereert op haar beurt elektromagnetische golven die in verschillende richtingen reizen. Een deel van het invallende licht wordt dus in een willekeurige richting gestuurd.

Het blijkt dat dit effect sterker is voor licht met kortere golflengtes. Wanneer we vervolgens uitzoomen naar de schaal van de atmosfeer, wat zien we dan? Overal in de atmosfeer bevinden zich deze kleine deeltjes die een deel van het licht van de zon in willekeurige richtingen afbuigen. Dit gebeurt meer voor licht aan de blauwe kant van het spectrum dan aan de rode kant (aangezien blauw een kortere golflengte heeft). Als gevolg hiervan zien we blauw licht vanuit alle richtingen in de lucht. Dit effect wordt nog duidelijker bij zonsopkomst of zonsondergang, omdat het zonlicht dan door een groter deel van de atmosfeer moet reizen voordat het je oog bereikt. Steeds meer van het blauwe deel van het spectrum wordt door verstrooiing verwijderd, wat resulteert in een prachtig rode zon vlak voordat deze onder de horizon verdwijnt.

DIRECTIONELE VERSTROOIING

Het manipuleren van licht met behulp van kleine structuren wordt al lange tijd gedaan. Vaak worden herhalende structuren, zoals tralie, gebruikt om licht een andere richting op te sturen. Door de herhaling van de structuur interfereert het licht in bepaalde richtingen constructief, terwijl het in andere richtingen destructief interfereert. Dergelijke structuren kunnen zeer goed gemaakt worden en het licht in een smalle verzameling van hoeken afbuigen.

De richting waarin het licht wordt verstrooid, hangt af van de afstand (de zogenoemde pitch) tussen de herhalende elementen, in vergelijking met de golflengte van het licht. Als gevolg daarvan wordt wit licht dat op zo'n structuur valt opgesplitst in een regenboog, waarbij elke kleur in een andere richting wordt afgebogen. Dit kan zowel een voordeel als een nadeel zijn: als we het spectrum van een bepaalde lichtbron willen bepalen, is een tralie daar perfect voor. Aan de andere kant, als we met deze structuren een lens willen maken, zal het brandpunt voor elke kleur op een andere positie liggen. Dit wordt een probleem wanneer een dergelijke lens bijvoorbeeld in een camera wordt gebruikt.

Voor het afbuigen van licht, beschouwen wij breedbandtoepassingen waarbij alle kleuren van het (zichtbare) licht worden gebruikt. Daarom zullen we in eerste instantie deze herhalende structuren buiten beschouwing laten. In plaats daarvan beschouwen we individuele verstrooiende deeltjes, waarna we kijken naar de collectieve respons van deze deeltjes. Hoewel bekend is dat de verstrooiing door zulke deeltjes wordt bepaald door de geometrie en de brekingsindex van het nanodeeltje, is de exacte relatie hiervan niet bekend. Hierdoor bestaat er momenteel geen methode om een nanodeeltje zo te ontwerpen dat het licht in een specifieke richting verstrooit. Deze thesis zal proberen zo'n methode te vinden. Daarnaast zullen we laten zien hoe een zeer efficiënt tralie gecreëerd kan worden door gebruik te maken van de directionele verstrooiing van individuele deeltjes.

METHODEN EN RESULTATEN VAN DE THESIS

Om deze doelen te bereiken, zullen we een methode ontwikkelen voor het ontwerp van een enkel nanodeeltje dat licht in een voorkeursrichting verstrooit. Deze methode wordt vervolgens gebruikt om een nanodeeltje te ontwerpen dat zichtbaar licht afbuigt door middel van verstrooiing. We zijn erachter gekomen dat breedbandige directionele verstrooiing bereikt kan worden door een absorberend en niet-absorberend materiaal te combineren in één nanodeeltje. Dit is komt door de introductie van een faseverschil in het verstrooide veld door de verschillende materialen waar het nanodeeltje uit bestaat.

De nanodeeltje worden vervolgens geproduceerd met behulp van verschillende nanofabricagetechnieken, deze worden dan in het lab gemeten om de theory met metingen te bevestigen. Hiervoor hebben we een ontwerp gebruikt waar silica glas en goud in zit. We hebben vastgesteld dat de metingen overeenkomen met de ontwikkelde theorie.

Deze theorie is ook toegepast op diffractie tralies, waar een ontwerp voor een zeer efficiënte transmissie diffractie tralie uit kwam. Hierbij worden de tralie lijnen gemaakt door glas te combineren met een metaal of halfgeleider materiaal. De tralies worden vervolgens gemaakt met behulp van nanofabricagetechnieken zoals elektronenbundellithografie en droog etsen. De tralies worden vervolgens gemeten en hun prestaties vergeleken met de theorie.

De metingen lieten een slechtere prestatie zien voor tralies met metaal. Dit komt waarschijnlijk door de toename in absorptie door de ultra dunne lagen metaal die gebruikt zijn. Voor tralies die met titaniumnitride, een halfgeleider materiaal, gemaakt zijn hebben we wel de verwachte verbeterde prestatie gezien.

Als laatste hebben we een numerieke Monte Carlo methode ontwikkeld om te bepalen of het mogelijk is om een volume met nanodeeltjes te maken welke een inkomende bundel licht afbuigen in een specifieke richting; het originele idee van het promotieproject. We hebben bepaald dat dit niet mogelijk is zonder een aanzienlijke hoeveelheid licht te verliezen, iets dat onwenselijk is voor de toepassing waar dit idee voor bedacht was.

1

INTRODUCTION

LIGHT has such a prevalent part in our daily lives, it is easy to forget how important it is. We rely for a large part on light to make sense of our environment using our eyes. Going further than that: without the light from the sun, life on earth would not be possible. Optics, the part of science that deals with study of light has also been incredibly important to science as a whole: allowing us to develop all kind of sensors, harvest energy from the sun and see so much more than just with our naked eyes, from the discovery of micro-organisms to entire galaxies. In this thesis, I hope to contribute to the incredibly beautiful scientific field that optics is.

1.1. MANIPULATION OF LIGHT

The manipulation of light is a crucial aspect of modern technology. Obvious examples of its use is in microscopes and telescopes, but it also very important for telecommunication, sensors, display technology and the fabrication of computer chips.

Traditionally, lenses, mirrors and prisms are used to manipulate light, relying on the laws of reflection and refraction. Most modern technologies still rely on these principles, and it is still extensively being studied in the field of geometrical optics. However, there are applications in which the inherent bulkiness of these components are unwanted, and other techniques need to be explored.

One such technique is by taking advantage of the wave-like nature of light. A commonly used example of this is a diffraction grating. Such a grating consist of evenly spaced narrow grooves. Due to the repeating structure, light hitting different parts of the structure can interfere. As a result, light is redirected in a different direction depending on the wavelength of the light. Because of this wavelength dependence, gratings are often used to determine the spectrum of a light source.

Another way of taking advantage of the wave-like nature of light is by reducing the thickness of a lens. From this point of view, all the lens does is to introduce a phase difference onto the incident waves. Once the phase difference is larger than 2π , the

thickness can be reduced (see [Figure 1.1](#)). This does leave some challenges regarding the fabrication of such lenses, especially when they are made of glass.

Similar to this, a so-called metalens can be created[1]. Very small structures (in the order of the wavelength of light) can introduce a phase difference depending on their geometry. With this, a phase profile can be generated over a large area, similar to that of a normal lens made of glass. The advantage of such a lens is that they are effectively two dimensional, which can be especially useful in applications where the space for optical elements is limited, or where weight is a consideration. Many studies are currently being done towards metalenses, as it still proves difficult to produce an achromatic lens with a large numerical aperture due to the presence of Fresnel zones[2].

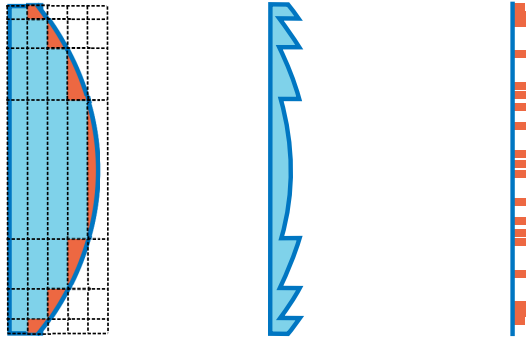


Figure 1.1: Traditional plano-convex lens horizontally divided in parts of 2π phase. Orange parts are the only contributing to phase change (a). Fresnel lens made of only the orange parts of the traditional lens (b). Graphical representation of a 2D metalens achieving the same phase change (c).

Instead of relying on all these very small structures to introduce a phase difference together, we could use the scattering of light by these structures directly. Then, the directionality does not originate from the collective contributions of the structures, but rather from the single elements. For visible light, the size of these structures are in the order of a few hundred nanometers. Because of this, we call them nanoparticles or nanostructures. The objective then is to design a nanoparticle that scatters light in a specific direction.

The advantage of the single nanoparticle is that they can be integrated into a volume. Light propagating through the volume can then be manipulated on the macroscale. This could have applications in LEDs, where light can be redirected such that it can be coupled out of the LED, improving energy efficiency and providing more control over the angular intensity distribution. Another application would be in diffusers, where the properties of the diffuser can be tailor-made. From this follows the aim of this thesis: **to design a volume with nanoparticles that has a desired scatter behaviour.**

1.2. NANOPARTICLES IN PHYSICS, CHEMISTRY AND BIOLOGY

Nanoparticles have been used for many applications, taking advantage of their special properties due to their small size.

In physics, nanoparticles have mainly been used for their scattering characteristics. Nanoparticles are able to resonantly scatter light at specific wavelengths, enhancing the color of the medium it is used in. One use for nanoparticles is the enhancement of the emission of fluorescent in blue pumped white LEDs. The nanoparticles are able to concentrate the electric field, enhancing the emission of light, while at the same time able to effectively couple the light out of the LED[3, 4]. Similarly, nanoparticles can be used to enhance the efficiency of solar cells. Through the same enhancement of the electric field, the absorption of light by solar cells can be increased[5].

In biology three major areas can be defined where nanoparticle are used. These areas are drug and gene delivery, sensing and imaging.

Examples include the delivery of drugs and contrast agents: a study was done where fluorophores inside of capped mesoporous silica nanoparticles are delivered to cancer cells. Due to the presence of certain compounds in cancer cells which can remove the caps, the fluorophores are released inside the cancer cells[6].

A surprising application of nanoparticles in biology is something we have all had contact with in the past few years: the lateral flow tests for Covid-19. In these selftests, gold nanoparticles are used to show the test result as lines. The red color of these lines on the selftest is caused by the nanoparticles. A simply explanation of how this works, goes as follows: A sample pad is used upon which one side a fluid is put with the liquid sample to be tested for Covid-19 antigens. Through capillary forces, the solution is pulled through the sample pad. First, the solution encounters antibodies which are attached to the gold nanoparticles. These antibodies can bind to the virus material in the liquid sample.

These antibodies are then dragged towards the two lines of the test. The first line has another set of antibodies which are immobilized, these can also bind to the virus material. Therefore, if there is virus material in the liquid sample, the gold nanoparticles would get stuck here. Then the rest of the material continues on towards the second line. Here, another set of immobilized antibodies is placed. However, these antibodies do not bind to the virus material, but rather to the gold nanoparticles. The result is that for a positive test, you will see two lines of gold nanoparticles which are red in color. For a negative test you will only see gold nanoparticles on the second line as they would only be able to attach there.

Besides self-tests, the application of organic nanoparticles in Covid-19 vaccines has been investigated for the delivery and protection of the active substance of the vaccine[7].

In chemistry nanoparticles are often used as a catalyst, one example is the use of copper nanoparticles as a catalyst in the synthesis of organic chemicals[8].

1.3. OUTLINE OF THE THESIS

In this chapter, we have explained the basics of manipulating light and gave an introduction to nanoparticles. Furthermore, we explained why we are looking into the scattering of individual nanoparticles. The rest of the thesis is organized as follows:

- **In Chapter 2**, we will look into methods that are used to determine the scattering properties of nanoparticles. First, the analytical methods are presented for the specific cases they are valid for. Next, some numerical methods are presented. Finally, a method is presented for understanding the directional scattering using a multipole decomposition.
- **In Chapter 3**, a method is investigated and developed for designing nanoparticles that scatter light in a particular direction. Initially, simple geometries are considered. Since these cannot satisfy our conditions, more complex geometries are considered from which a design is made. Based on these findings, a design for a highly efficient broadband grating is presented.
- **In Chapter 4**, the fabrication of the designed nanoparticles is investigated. Several methods are considered and their practical results are presented. The advantages and disadvantages of the production methods is also discussed. The results of the fabrication of both the nanoparticles and gratings are shown.
- **In Chapter 5**, a method of measuring the scattering by nanoparticles is presented. Furthermore, the results from the designed and fabricated nanoparticles are compared to their theoretical scatter patterns. Also, a method for measuring the grating efficiency is presented. The measurements of the fabricated gratings are shown and compared to a standard glass grating.
- **In Chapter 6**, the volumetric scattering by the designed nanoparticles are considered in theory. In this chapter, a start is made for using these nanoparticles at a macro scale. First, a method is developed for determining the scattering by many nanoparticles and then used for the designed nanoparticles.
- **In Chapter 7**, conclusions are drawn for the overall thesis and an outlook and recommendations are given for future research on this topic.

2

SOLVING SCATTERING PROBLEMS



The physicist in preparing for his work needs three things: mathematics, mathematics, and mathematics.

Wilhelm Conrad Röntgen[9]



FOR most purposes, a scattering problem can be defined as follows: let us consider a particle occupying some space Ω in an otherwise completely homogeneous medium. Then, if we have an incident time-harmonic field given by $E^{\text{inc}}(\mathbf{r})$, what would the resulting fields be due to the scattering of light by the particle? Such a problem is important for designing optical components at the nanoscale, like nano-antennas[10–17], metasurfaces[18–24] and waveguides[3]. The incident field is generally known in this case, and the objective is to design the particles in such a way that the light is scattered into a desired direction. The inverse problem is being studied in the field of metrology[25]. In this case, limited knowledge exists about the scattered fields and the challenge is to determine what particle (size and/or material) is responsible for the scattered field. Such problems are hard to solve since they are ill-posed: there may not be a solution if the measurement is not accurate enough, or many solutions could exist. Often, some assumptions about the particle need to be made beforehand to arrive at a solution.

In this chapter, several methods of solving scattering problems are presented. First, we will take a look at well-known methods: using the Lippman-Schwinger integral equation (Section 2.2), and Mie theory (Section 2.3). Then, we will consider numerical methods: the T-matrix method (Section 2.4) and Finite Element Methods (Section 2.5). Finally, we will look at the multipole decomposition (Section 2.6), a tool which enables a more intuitive way of understanding scattering.

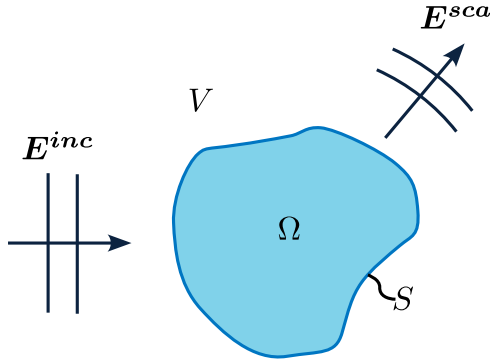


Figure 2.1: Drawing of a scattering problem. An electric field E^{inc} is incident on a particle occupying a volume Ω , bounded by a surface S inside the infinite volume V . As a result, the field E^{sca} is scattered away from the particle.

2.1. ALL ABOUT CROSS SECTIONS

In order to understand the scattering by particles and the results from the methods we will discuss, we need to understand the concept of optical cross sections. Cross sections are used as a measure to what extent an electromagnetic wave is affected by an object in its path. Comparing this to the geometrical cross section of the object from the perspective of the electromagnetic wave, can tell us a lot about the interaction.

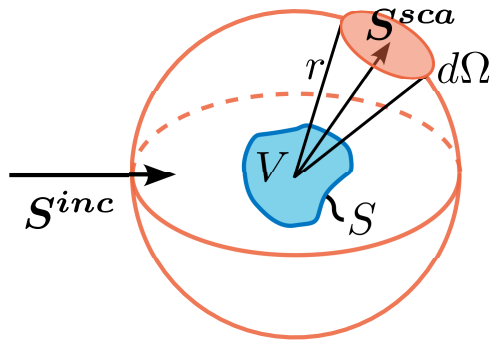


Figure 2.2: Drawing for the derivation of the scattering and absorption cross section. An electromagnetic wave with Poynting vector S^{inc} is incident on a particle with volume V and surface S , as a result an electromagnetic wave is scattered with Poynting vector S^{sca} . For the derivation of the cross sections, a sphere with radius r is constructed around the particle and a solid angle $d\Omega$ is defined

Let us consider a time-harmonic electromagnetic wave propagating towards an arbitrary particle as in [Figure 2.2](#). Due to the presence of the particle, some of the light will be scattered. From here, we can define the differential cross section[26] by comparing the scattered power radiated into a solid angle with the total incident power per unit area. First we define a sphere with radius r , the total incident power per unit area is given by $|S^{inc}|$ with S^{inc} the Poynting vector associated with the incident wave. The scattered power into a solid angle $d\Omega$ is then given by $S^{sca} \cdot \hat{r} r^2 d\Omega$. By dividing these

terms, we get the differential cross section:

$$\frac{d\sigma_{\text{sca}}}{d\Omega} = \frac{\hat{\mathbf{r}} \cdot \mathbf{S}^{\text{sca}}}{|\mathbf{S}^{\text{inc}}|/r^2}. \quad (2.1)$$

Integrating the above expression over all angles produces the scattering cross section:

$$\sigma_{\text{sca}} = \int_{\Omega} r^2 \frac{\hat{\mathbf{r}} \cdot \mathbf{S}^{\text{sca}}}{|\mathbf{S}^{\text{inc}}|} d\Omega. \quad (2.2)$$

Of course, some of the energy carried by the incident electromagnetic wave could be absorbed. We can use the conservation of energy to define the absorption cross section. Energy conservation in the context of electromagnetic field is given by

$$\int_V \nabla \cdot \mathbf{S} d^3r + \frac{d}{dt} \int_V u_{\text{EM}} d^3r = - \int_V \mathbf{j} \cdot \mathbf{E} d^3r. \quad (2.3)$$

Here, \mathbf{j} is the current density vector and \mathbf{E} the electric field within the volume V , and u_{EM} is the electromagnetic energy density, which given by

$$u_{\text{EM}} = \frac{1}{2} \epsilon_0 (\mathbf{E} \cdot \mathbf{E} + c^2 \mathbf{B} \cdot \mathbf{B}). \quad (2.4)$$

Applying the divergence theorem and rearranging the terms, we get

$$\int_S \hat{\mathbf{n}} \cdot \langle \mathbf{S} \rangle dA = - \int_V \langle \mathbf{j} \cdot \mathbf{E} \rangle d^3r - \frac{d}{dt} \int_V u_{\text{EM}} d^3r, \quad (2.5)$$

where $\hat{\mathbf{n}}$ is the unit normal on S pointing outwards with respect to the volume V .

If positive, the left side of the above equation is the amount of energy exiting the volume. Therefore, the right side can be interpreted as energy being generated and hence the integrals on the right-hand side without the minus sign is the energy that is dissipated in the volume V . Similar to the scattering cross section (Equation 2.2), we can use this to define the absorption cross section:

$$\sigma_{\text{abs}} = \frac{1}{|\mathbf{S}^{\text{inc}}|} \int_V \mathbf{j} \cdot \mathbf{E} d^3r + \frac{d}{dt} \int_V u_{\text{EM}} d^3r. \quad (2.6)$$

We can simplify this expression by getting rid of the second integral by averaging over one period of the electromagnetic wave, since the integral will then be constant with respect to time. We obtain the time-averaged absorption cross section:

$$\langle \sigma_{\text{abs}} \rangle = \frac{1}{|\mathbf{S}^{\text{inc}}|} \int_V \langle \mathbf{j} \cdot \mathbf{E} \rangle d^3r. \quad (2.7)$$

From here, the extinction cross section can be defined as the equivalent cross section of the amount of energy that is removed from the incident electromagnetic wave by the particle:

$$\sigma_{\text{ext}} = \sigma_{\text{sca}} + \sigma_{\text{abs}}. \quad (2.8)$$

If we would like to use the simpler, time-averaged absorption cross section, we will also have to define the time-averaged scattering cross section:

$$\langle \sigma_{\text{sca}} \rangle = \int_{\Omega} r^2 \frac{\hat{\mathbf{r}} \cdot \langle \mathbf{S}^{\text{sca}} \rangle}{|\mathbf{S}^{\text{inc}}|} d\Omega. \quad (2.9)$$

The time-averaged extinction cross section is then given by

$$\langle \sigma_{\text{ext}} \rangle = \langle \sigma_{\text{sca}} \rangle + \langle \sigma_{\text{abs}} \rangle. \quad (2.10)$$

In this thesis, we will only consider time-harmonic fields. So, from this point on, when referring to the scattering, absorption and extinction cross sections we are referring to the time-averaged versions in [Equation 2.9](#), [Equation 2.7](#) and [Equation 2.10](#), even when the brackets are not used.

The way to interpret these cross sections is by comparing them to the geometrical cross section of a particle. We will start by looking at a very large particle (compared to the wavelength of the incident wave).

A good example would be to take a macroscopically sized, solid, non-transparent object upon which visible light is incident. Let us take a golfball as an example. When a beam of light hits the golfball, a shadow is cast behind the golfball. Furthermore, the light hitting the golfball is reflected in many different directions. It is tempting to say that the scattering cross section is equal to that of the geometrical cross section of the golfball, this is however not the case.

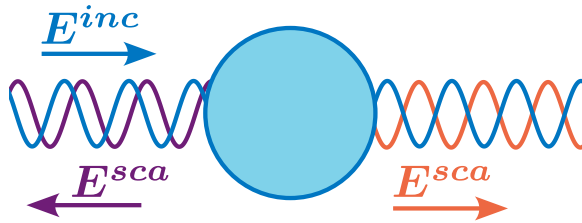


Figure 2.3: A golfball scattering light so that it produces a shadow on the back side. To produce a full shadow, the amount of light scattered must be proportional to 2 times the geometrical scattering cross section. One part which reflects the incident light back, and one which interferes destructively with the incident light. The direction of the propagating fields is shown with arrows.

Of course, the reflected light power relative to the incident power by the golfball is exactly the geometrical cross section, however this does not account for the shadow being cast by the golfball. For this we effectively need a second source in the ball to exactly destructively interfere with the light which would continue to propagate without the golfball. This, added to the cross section from the reflection would result in a total scattering cross section of two times the geometrical cross section. A drawing of this situation is shown in [Figure 2.3](#).

2.2. THE LIPPMANN-SCHWINGER INTEGRAL EQUATION

Let us go back to the problem statement at the start of this chapter. To derive an expression for the scattered field, we will first add some additional details. To start, let

us again assume that the fields are time-harmonic ($\propto e^{-i\omega t}$, with $\omega > 0$). Furthermore, we will assume that the relative permittivity of the medium is given by ϵ_{med} and that of the scatterer given by $\epsilon(\mathbf{r})$. Since we consider scattering at optical frequencies, we will assume that the relative permeability is unity, as is the case for most materials. Also, we will not consider any non-linear effects. These assumptions are summarized in Figure 2.4.

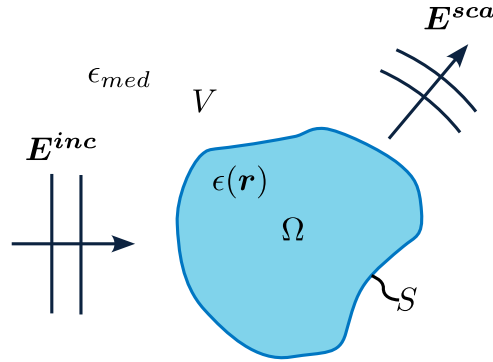


Figure 2.4: Drawing of a scattering problem. A time-harmonic electric field E^{inc} is incident on a particle occupying a volume Ω with relative permittivity $\epsilon(\mathbf{r})$, bounded by a surface S inside the infinite volume V with relative permittivity ϵ_{med} . As a result, the field E^{sca} is scattered away from the particle.

A nice expression which separates the total electric field into an incident and scattered field is given by the Lippmann-Schwinger integral equation. To get to this equation, we start from the macroscopic Maxwell equations[27]:

$$\nabla \times \mathbf{E} = i\omega \mathbf{B}, \quad (2.11)$$

$$\nabla \cdot (\epsilon_0 \epsilon(\mathbf{r}) \mathbf{E}) = \rho, \quad (2.12)$$

$$\nabla \times \mathbf{H} = -i\omega \epsilon_0 \epsilon(\mathbf{r}) \mathbf{E} + \mathbf{J}, \quad (2.13)$$

$$\nabla \cdot \mathbf{H} = 0, \quad (2.14)$$

with \mathbf{E} the complex electric field, \mathbf{B} the complex magnetic field, ϵ_0 the permittivity of vacuum, $\epsilon(\mathbf{r})$ the relative permittivity. We also included the total electric current density \mathbf{J} and the charge density ρ .

From here, we will separate the total electric field into the incident field and the scattered field:

$$\mathbf{E} = \mathbf{E}^{\text{inc}} + \mathbf{E}^{\text{sca}} \quad (2.15)$$

Apart from the currents at a large distance that radiate the incident field, there are no currents and charges. Hence, $\mathbf{J} = 0$ and $\rho = 0$. The incident field is a solution to the Maxwell equations, without sources and without the scatterer. Therefore, $\epsilon(\mathbf{r}) = \epsilon_{\text{med}}$ and $\mathbf{J} = 0$.

For the scattered field we have

$$\nabla \times \mathbf{H}^{\text{sca}} = \nabla \times \mathbf{H} - \nabla \times \mathbf{H}^{\text{inc}} \quad (2.16)$$

$$= -i\omega\epsilon_0\epsilon(\mathbf{r})\mathbf{E} + i\omega\epsilon_0\epsilon_{\text{med}}\mathbf{E}^{\text{inc}} \quad (2.17)$$

$$= -i\omega\epsilon_0\epsilon(\mathbf{r})\mathbf{E} + i\omega\epsilon_0\epsilon_{\text{med}}(\mathbf{E} - \mathbf{E}^{\text{sca}}) \quad (2.18)$$

$$= -i\omega\epsilon_0\epsilon_{\text{med}}\mathbf{E}^{\text{sca}} - i\omega\epsilon_0(\epsilon(\mathbf{r}) - \epsilon_{\text{med}})\mathbf{E}. \quad (2.19)$$

Thus, the scattered field satisfies Equation 2.13 with

$$\mathbf{J}(\mathbf{r}) = -i\omega\epsilon_0(\epsilon(\mathbf{r}) - \epsilon_{\text{med}})\mathbf{E}. \quad (2.20)$$

The current density is related to the polarization field through

$$\mathbf{J} = \frac{\partial \mathbf{P}}{\partial t}. \quad (2.21)$$

Here, \mathbf{P} is the polarization field. The polarization is then given by

$$\mathbf{P} = \epsilon_0[\epsilon(\mathbf{r}) - \epsilon_{\text{med}}]\mathbf{E}. \quad (2.22)$$

In Appendix A, we have shown that the Green's tensor \overline{G}_E maps the polarization to the electric field. Therefore, the scattered electric field can be written as

$$\mathbf{E}^{\text{sca}}(\mathbf{r}) = \int \overline{G}_E(\mathbf{r}, \mathbf{r}_0)\mathbf{P}(\mathbf{r}_0)d^3r_0 \quad (2.23)$$

$$= \int \epsilon_0[\epsilon(\mathbf{r}_0) - \epsilon_{\text{med}}]\overline{G}_E(\mathbf{r}, \mathbf{r}_0)\mathbf{E}(\mathbf{r}_0)d^3r_0. \quad (2.24)$$

Then, the total field is given by

$$\mathbf{E}(\mathbf{r}) = \underbrace{\int_{\Omega} \epsilon_0[\epsilon(\mathbf{r}_0) - \epsilon_{\text{med}}]\overline{G}_E(\mathbf{r}, \mathbf{r}_0)\mathbf{E}(\mathbf{r}_0)d^3r_0}_{\mathbf{E}^{\text{sca}}} + \mathbf{E}^{\text{inc}}(\mathbf{r}). \quad (2.25)$$

The Green's tensor can be derived by calculating the electric field generated by an electric dipole (Equation A.33). Since we are only interested in the scattered far field, we will use the expression for the Green's tensor where

$$\frac{r}{\lambda} > \left(\frac{D}{\lambda}\right)^2. \quad (2.26)$$

The field is then given by

$$\mathbf{E}^{\text{sca}}(\mathbf{r}) = \frac{k^2}{4\pi\epsilon_{\text{med}}r} e^{ikr} \int e^{ik\hat{\mathbf{r}}\cdot\mathbf{r}_0} [\epsilon(\mathbf{r}) - \epsilon_{\text{med}}] \hat{\mathbf{r}} \times [\hat{\mathbf{r}} \times \mathbf{E}(\mathbf{r}_0)] d^3r_0. \quad (2.27)$$

This equation can be simplified further, since we are generally only interested in the intensity (as a function of the spherical coordinates θ and ϕ) of the scattered field. Therefore, we only consider the magnitude of the scattered field, which is given by

$$|\mathbf{E}^{\text{sca}}(\mathbf{r})| = \frac{k^2}{4\pi\epsilon_{\text{med}}r} \int |[\epsilon(\mathbf{r}) - \epsilon_{\text{med}}]\mathbf{E}(\mathbf{r}_0)| d^3r_0. \quad (2.28)$$

Equation 2.25 is called the Lippman-Schwinger integral equation. This equation is a very nice description of the problem as the total field is split up into an incident field and a scattered field. The downside however, is that the total field also appears in the integral for the scattered field, making this equation difficult to solve.

Several methods of solving this equation have been suggested, for example the Born series and the Born-Padé series[28]. The simplest is to use the first Born approximation, where we approximate the total field inside the particle by the incident field so that

$$\mathbf{E}(\mathbf{r}) \approx \int_{\Omega} \epsilon_0 [\epsilon(\mathbf{r}_0) - \epsilon_{\text{med}}] \bar{G}_E(\mathbf{r}, \mathbf{r}_0) \mathbf{E}(\mathbf{r}_0) d^3 r_0 + \mathbf{E}^{\text{inc}}(\mathbf{r}_0). \quad (2.29)$$

Now, the right side is known and the electric field can be calculated with relative ease. However, this only works when the particle has a very low contrast compared to the medium (in practice this means less than a 1% difference in refractive index).

2.3. MIE THEORY

An analytical method exists for determining the scattering by infinitely long cylinders and by spheres called Mie theory[25, 29, 30]. For the case of a sphere which we will consider here, Mie theory solves the problem of light scattering by decomposing the incoming and scattered waves into spherical harmonics.

To start, let us consider a dielectric sphere with radius a in vacuum, centered at the origin of the coordinate system.

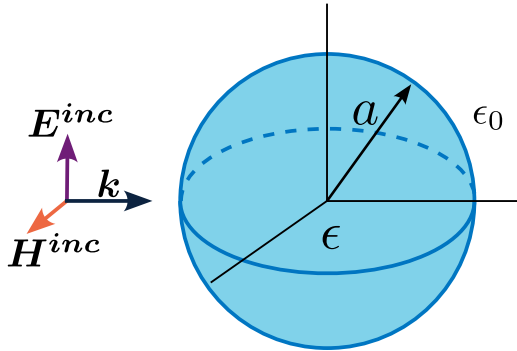


Figure 2.5: plane-wave incident on a spherical particle with relative permittivity ϵ and radius a . The particle is inside vacuum with permittivity ϵ_0 .

In homogeneous and isotropic materials, where no sources are present, the electric and magnetic fields satisfy the following equations:

$$\nabla^2 \mathbf{E} + k^2 \mathbf{E} = 0, \quad (2.30)$$

$$\nabla^2 \mathbf{H} + k^2 \mathbf{H} = 0. \quad (2.31)$$

The solutions to these equation can be written with the help of the solutions to the scalar Helmholtz equation given by

$$\nabla^2 \psi + k^2 \psi = 0. \quad (2.32)$$

Then, the following vectors are solutions to the vector Helmholtz equation:

$$\mathbf{L} = \nabla \psi, \quad (2.33)$$

$$\mathbf{M} = \nabla \times (\mathbf{r}\psi), \quad (2.34)$$

$$\mathbf{N} = \frac{1}{k} \nabla \times \mathbf{M}. \quad (2.35)$$

The \mathbf{L} vector represent longitudinal waves, while the \mathbf{M} and \mathbf{N} vectors represent transversal waves that satisfy the vector Helmholtz equation

$$\nabla \times \nabla \times \mathbf{E} - k^2 \mathbf{E} = 0. \quad (2.36)$$

In order to find the expressions for these vector fields, we will need to find the solution for the scalar Helmholtz equation. This is done in spherical coordinates, so that we can easily apply the boundary conditions for the spherical dielectric particle later.

Using separation of variables, it can be shown that a solution to the scalar Helmholtz equation is equal to

$$\psi = \sum_{l=0}^{\infty} \sum_{m=-l}^l \psi_{l,m}(r, \theta, \varphi) = \sum_{l=0}^{\infty} \sum_{m=-l}^l \gamma_{l,m} z_l(kr) Y_l^m(\theta, \varphi). \quad (2.37)$$

with the coefficients $\gamma_{l,m}$, $z_l(kr)$ any of the spherical Bessel functions j_l , y_l , the spherical Hankel function of the first kind $h_l^{(1)}$ and the second kind $h_l^{(2)}$ with order l , and $Y_l^m(\theta, \varphi)$ the spherical harmonics given by

$$Y_l^m(\theta, \varphi) = P_l^m(\cos \theta) e^{im\varphi}. \quad (2.38)$$

Here, P_l^m are the associated Legendre polynomials with degree l and order m . From here, will use the subscript l, m to indicate the used degree and order of the vector spherical harmonics as well.

For the \mathbf{L} , \mathbf{M} and \mathbf{N} vector spherical harmonics, the z_l in [Equation 2.37](#) is replaced by the spherical Hankel function of the first kind in the case of outgoing spherical waves. In the case of incoming spherical waves, it is replaced by the spherical Hankel function of the second kind. The complete expressions can be found in [Appendix A](#).

We also introduce the regularized spherical vector harmonics \mathbf{RgL} , \mathbf{RgM} and \mathbf{RgN} , where z_l in [Equation 2.37](#) is replaced by the spherical Bessel function j_l . The reason we introduce these functions is because the other three spherical Bessel functions are singular at the origin ($r = 0$).

Furthermore, it is convenient to separate [Equation 2.38](#) into an even and an odd part:

$$Y_{e,l}^m(\theta, \varphi) = P_l^m(\cos \theta) \cos(m\varphi), \quad (2.39)$$

$$Y_{o,l}^m(\theta, \varphi) = P_l^m(\cos \theta) \sin(m\varphi). \quad (2.40)$$

We will do the same for the spherical vector harmonics, where the subscript e and o will designate whether the even or odd part is used.

It can be shown that any electromagnetic field free of divergence¹ can be expanded in a sum of vector spherical harmonics:

$$\mathbf{E} = \sum_{l=0}^{\infty} \sum_{m=-l}^l a_{e,l,m} \mathbf{N}_{e,l,m}(kr, \theta, \phi) + b_{o,l,m} \mathbf{M}_{o,l,m}(kr, \theta, \phi). \quad (2.41)$$

Note that we only consider the fields outside of the particle here, for fields inside the particle we would have to use the regularized vector spherical harmonics to prevent the singularity from occurring.

This allows us to solve the vectorial Helmholtz equation separately for each mode given by l, m . The coefficients $a_{e,l,m}$ and $b_{o,l,m}$ can be calculated by using the orthogonality of the vector spherical harmonics, which results in the following equations[30]:

$$a_{e,l,m} = \frac{\int \mathbf{E} \cdot \mathbf{N}_{e,l,m} \sin \theta d\theta d\phi}{\int |\mathbf{N}_{e,l,m}|^2 \sin \theta d\theta d\phi} \quad (2.42)$$

$$b_{o,l,m} = \frac{\int \mathbf{E} \cdot \mathbf{M}_{o,l,m} \sin \theta d\theta d\phi}{\int |\mathbf{M}_{o,l,m}|^2 \sin \theta d\theta d\phi} \quad (2.43)$$

We can separate the total fields in the incident field and the scattered field:

$$\mathbf{E} = \mathbf{E}^{\text{inc}} + \mathbf{E}^{\text{sca}}, \quad (2.44)$$

$$\mathbf{H} = \mathbf{H}^{\text{inc}} + \mathbf{H}^{\text{sca}}. \quad (2.45)$$

The incoming field can then be decomposed according to [Equation 2.41](#):

$$\mathbf{E}^{\text{inc}} = \sum_{l=0}^{\infty} \sum_{m=-l}^l a_{e,l,m}^{\text{inc}} \mathbf{RgN}_{e,l,m}(kr, \theta, \phi) + b_{o,l,m}^{\text{inc}} \mathbf{RgM}_{o,l,m}(kr, \theta, \phi). \quad (2.46)$$

Here we use the regularized spherical harmonics vectors, since the field cannot have a singularity in $r = 0$.

Similarly, for the field inside the dielectric particle

$$\mathbf{E}^{\text{par}} = \sum_{l=0}^{\infty} \sum_{m=-l}^l a_{e,l,m}^{\text{par}} \mathbf{RgN}_{e,l,m}(kr, \theta, \phi) + b_{o,l,m}^{\text{par}} \mathbf{RgM}_{o,l,m}(kr, \theta, \phi). \quad (2.47)$$

Finally for the scattered field outside the particle, we can write

$$\mathbf{E}^{\text{sca}} = \sum_{l=0}^{\infty} \sum_{m=-l}^l a_{e,l,m} \mathbf{N}_{e,l,m}(kr, \theta, \phi) + b_{o,l,m} \mathbf{M}_{o,l,m}(kr, \theta, \phi). \quad (2.48)$$

¹We only consider transversal fields, since the divergence of the electric field vanishes both inside and outside the sphere.

Unlike before, we cannot use the regularized vectors here. Because the scattered fields are outgoing spherical waves, they can be fully described by the Hankel function of the first kind $h_l^{(1)}$ in Equation 2.37. Similar expressions exist for the magnetic field.

To solve the coefficients we are interested in (the ones describing the scattered field), we need to solve for the boundary conditions at $r = a$, given by the matching conditions:

$$\hat{n} \times (\mathbf{E}^{\text{inc}} + \mathbf{E}^{\text{sca}} - \mathbf{E}^{\text{par}}) = 0, \quad (2.49)$$

$$\hat{n} \times (\mathbf{H}^{\text{inc}} + \mathbf{H}^{\text{sca}} - \mathbf{H}^{\text{par}}) = 0, \quad (2.50)$$

$$\hat{n} \cdot (\epsilon_0 \mathbf{E}^{\text{inc}} + \epsilon_0 \mathbf{E}^{\text{sca}} - \epsilon \mathbf{E}^{\text{par}}) = 0, \quad (2.51)$$

$$\hat{n} \cdot (\mathbf{H}^{\text{inc}} + \mathbf{H}^{\text{sca}} - \mathbf{H}^{\text{par}}) = 0. \quad (2.52)$$

For a linearly x -polarized plane-wave travelling in the z -direction[30],

$$\mathbf{E}^{\text{inc}} = E_0 e^{ikr \cos(\theta)} \hat{\mathbf{x}} = E_0 \sum_{l=1}^{\infty} i^l \frac{2l+1}{l(l+1)} (\mathbf{M}_{o,l,1} - i \mathbf{N}_{e,l,1}) \quad (2.53)$$

incident on the dielectric sphere with radius a , the solution is given by

$$\mathbf{E}^{\text{sca}} = E_0 \sum_{l=1}^{\infty} \frac{2l+1}{l(l+1)} (i a_{e,l,1} \mathbf{N}_{e,l,1}(kr, \theta, \phi) - b_{o,l,1} \mathbf{M}_{o,l,1}(kr, \theta, \phi)), \quad (2.54)$$

with

$$a_{e,l,1} = \frac{n^2 j_l(n\alpha) \frac{\partial}{\partial \alpha} [\alpha j_l(\alpha)] - j_l(\alpha) \frac{\partial}{\partial \alpha} [n\alpha j_l(n\alpha)]}{n^2 j_l(n\alpha) \frac{\partial}{\partial \alpha} [\alpha h_l^{(1)}(\alpha)] - h_l^{(1)}(\alpha) \frac{\partial}{\partial \alpha} [n\alpha j_l(n\alpha)]}, \quad (2.55)$$

$$b_{o,l,1} = \frac{j_l(n\alpha) \frac{\partial}{\partial \alpha} [\alpha j_l(\alpha)] - j_l(\alpha) \frac{\partial}{\partial \alpha} [n\alpha j_l(n\alpha)]}{j_l(n\alpha) \frac{\partial}{\partial \alpha} [\alpha h_l^{(1)}(\alpha)] - h_l^{(1)}(\alpha) \frac{\partial}{\partial \alpha} [n\alpha j_l(n\alpha)]}, \quad (2.56)$$

where $\alpha = ka$, and j_l are the spherical Bessel functions (which is equal to the real part of the Hankel functions of the first kind).

Using Equation 2.9 and Equation 2.10, we can also calculate the scattering and extinction cross section[30]:

$$\sigma_{\text{sca}} = \frac{2\pi}{k^2} \sum_{l=1}^{\infty} (2l+1) (|a_{e,l,1}|^2 + |b_{o,l,1}|^2), \quad (2.57)$$

$$\sigma_{\text{ext}} = \frac{2\pi}{k^2} \sum_{l=1}^{\infty} (2l+1) \text{Re}\{a_{e,l,1} + b_{o,l,1}\}. \quad (2.58)$$

When we look at the plots of the vector spherical harmonics \mathbf{M} and \mathbf{N} , we see how the fields are decomposed. Figure 2.6 shows the vector spherical harmonics for the first few orders. Let us look specifically at the vector spherical harmonics of $l = 1..3$ and $m = 1$, which are supported by a spherical particle when a linearly polarized plane-wave

is incident propagating in the z -direction. We can recognize the electric and magnetic dipoles, quadrupoles and octupoles. N are the vector fields related to the electric multipoles and M are the vector fields related to the magnetic multipoles. Mie theory decomposes the fields into these multipole contributions: using Equation 2.57, the exact contribution of each multipole to the scattered field can be determined.

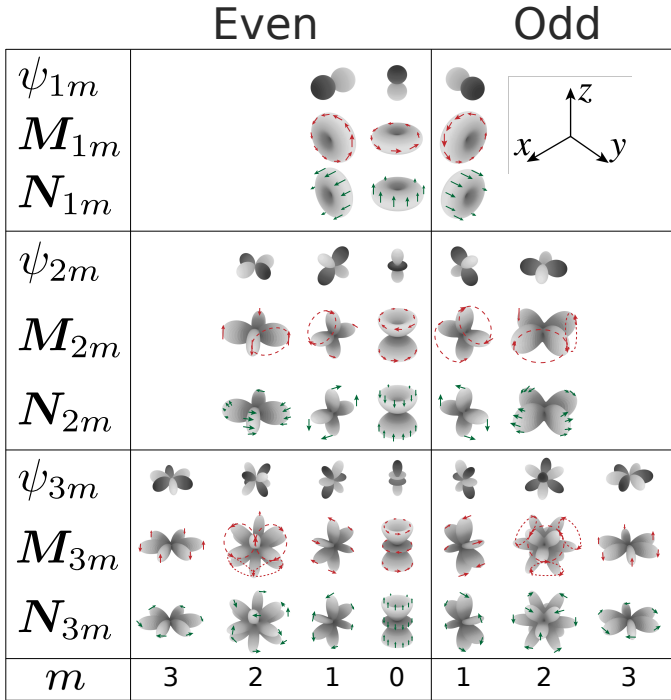


Figure 2.6: Even and odd versions of the first few vector spherical harmonics, the direction of the vector field is indicated in the figure with arrows.

(Adapted from <https://commons.wikimedia.org/wiki/File:VSHwiki.svg>)

2.4. TRANSFER MATRIX METHOD

Since most particles are not spheres, a method is needed to calculate the scattering by particles with arbitrary geometry. To this end, P. Waterman developed the Transfer matrix method[31–35]. The main idea of this method is to describe the scattering process as a matrix operation on the incident electric field:

$$\mathbf{E}^{\text{sca}} = T\mathbf{E}^{\text{inc}}. \quad (2.59)$$

The matrix T is then fully determined by the material and geometry of the scatterer.

We start by defining the scattering particle which occupies a volume Ω . This volume is then bounded by a closed surface S . The volume outside of S we will call V (see Figure 2.1). We assume that the space in which the particle is embedded is homogeneous, isotropic, non-magnetic and that no sources are present and all fields are time-harmonic. Like before, the electric field satisfies the Helmholtz equation:

$$\nabla^2 \mathbf{E} + k^2 \mathbf{E} = 0. \quad (2.60)$$

Following the approach by Waterman, let us initially assume that the particle is a perfect electric conductor. As a result, the fields inside the particle are equal to zero. The fields outside the conductor can be separated in an incident field and a scattered field like we did before (Equation 2.44 and Equation 2.45). Because the particle is a perfect conductor, the tangential components of the electric field on the surface S are zero. We introduce the magnetic current density

$$\mathcal{M} = -\hat{n} \times \mathbf{E} = -\hat{n} \times (\mathbf{E}^{\text{inc}} + \mathbf{E}^{\text{sca}}) = 0. \quad (2.61)$$

The magnetic field does not have to be zero on the surface of a perfect electric conductor. So, for the induced surface current density we have

$$\mathbf{J} = \hat{n} \times \mathbf{H} = \hat{n} \times (\mathbf{H}^{\text{inc}} + \mathbf{H}^{\text{sca}}). \quad (2.62)$$

Using the equivalence theorem, we can consider these currents as the sources of the electric and magnetic fields. Furthermore, we can rewrite the previous equations so we have:

$$\mathcal{M} = \hat{n} \times (-\mathbf{E}^{\text{inc}}) - \hat{n} \times \mathbf{E}^{\text{sca}} = 0, \quad (2.63)$$

$$\mathbf{J} = -\hat{n} \times (-\mathbf{H}^{\text{inc}}) + \hat{n} \times \mathbf{H}^{\text{sca}}. \quad (2.64)$$

Note that the initial problem of a particle which is a perfect electric conductor is equivalent to the perfectly conducting surface S , with current sources \mathcal{M} and \mathbf{J} producing the fields \mathbf{E}^{sca} and \mathbf{H}^{sca} in the volume outside the surface (in V) and the fields $-\mathbf{E}^{\text{inc}}$ and $-\mathbf{H}^{\text{inc}}$ in the volume inside the surface (in Ω). This is often called the extended boundary condition.

It is important to note that the incident and scattered fields are solutions to the Helmholtz equation in the volume V . Because of this, now that we have used the equivalence theorem, the medium of the volume Ω must be the same as the medium in volume V . If we then take into account the incident field which is not produced by

the sources \mathcal{M} and \mathbf{J} , we end up with fields equal to zero inside the volume Ω . This is the reason why the T-matrix method is also known as the null field method. A graphical representation of the above steps is shown in Figure 2.7.

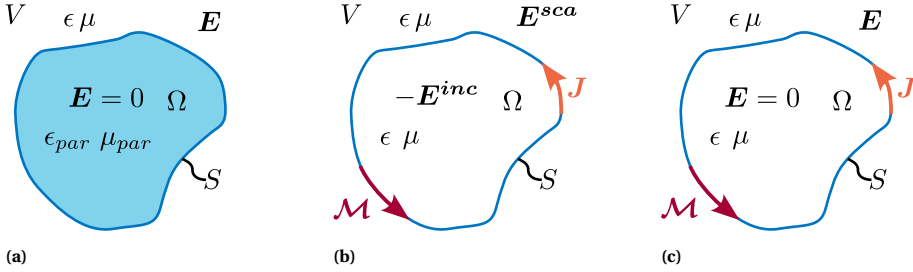


Figure 2.7: Schematic demonstration of the equivalence theorem with ϵ and ϵ_{par} the permittivity of the medium and the particle respectively and μ and μ_{par} the magnetic permeability of the medium and the particle respectively. (a) The assumption that the particle is a perfect electric conductor. (b) The equivalent problem, with the current sources \mathcal{M} and \mathbf{J} on the surface S . (c) The previous step taking into account the incident field.

Now that we have sources on a surface which radiate into an unbounded medium, we can use the following equations to calculate the resulting fields[36]:

$$\mathbf{E}^{\text{sca}} = \frac{i}{\omega \mu \epsilon} \nabla \times \nabla \times \mathbf{A}, \quad (2.65)$$

with the vector potential \mathbf{A} in the Lorentz gauge given by

$$\mathbf{A} = \mu \int_S \mathbf{J}(\mathbf{r}') G(\mathbf{r}, \mathbf{r}') dS', \quad (2.66)$$

where $G(\mathbf{r}, \mathbf{r}')$ is the free space Green's Function

$$G(\mathbf{r}, \mathbf{r}') = \frac{e^{-ik|\mathbf{r}-\mathbf{r}'|}}{4\pi|\mathbf{r}-\mathbf{r}'|}, \quad (2.67)$$

which satisfies the equation

$$\nabla^2 G(\mathbf{r}, \mathbf{r}') - k^2 G(\mathbf{r}, \mathbf{r}') = -\delta(\mathbf{r} - \mathbf{r}'). \quad (2.68)$$

The expression for the total field becomes

$$\mathbf{E}(\mathbf{r}) = \mathbf{E}^{\text{inc}}(\mathbf{r}) + \nabla \times \nabla \times \int_S \mathbf{J}(\mathbf{r}') \frac{i}{\omega \epsilon} \frac{e^{-ik|\mathbf{r}-\mathbf{r}'|}}{4\pi|\mathbf{r}-\mathbf{r}'|} dS'. \quad (2.69)$$

Before, we have determined that the total field in the volume Ω should be zero. Therefore, the above equation determines the surface current vector \mathbf{J} : it must be such that the scattered field cancels the incident field inside Ω . To solve this equation, we will expand it in the spherical vector harmonics \mathbf{M} and \mathbf{N} , as we did before in our discussion of Mie theory in Section 2.3.

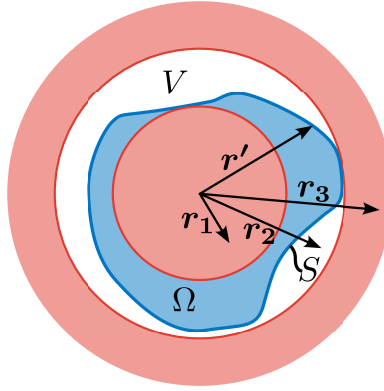


Figure 2.8: Schematic representation of the problem with the Green's Function. For the inscribing sphere and circumscribing sphere marked orange (for r_1 and r_3), the Green's Function is well defined. However, between these areas it is not since we can have the case where $r' = r$.

To do this, we will rewrite the Green's function above (Equation 2.68) in the form of vector spherical harmonics (often called the free space Green's dyadic). This Green's function is represented as a tensor (indicated by \bar{G}), the scalar product with the surface current vector then becomes a dot product. The free space Green's dyadic is given by the tensor[34]

$$\bar{G}(\mathbf{r}, \mathbf{r}') = \bar{I}G(\mathbf{r}, \mathbf{r}') = ik \sum_{l,m} (-1)^m \begin{cases} \mathbf{M}_{l,m}(kr, \theta, \phi) \mathbf{R}g \mathbf{M}_{l,m}(kr', \theta', \phi') \\ + \mathbf{N}_{l,m}(kr, \theta, \phi) \mathbf{R}g \mathbf{N}_{l,m}(kr', \theta', \phi') & \text{for } r > r' \\ \mathbf{R}g \mathbf{M}_{l,m}(kr, \theta, \phi) \mathbf{M}_{l,m}(kr', \theta', \phi') \\ + \mathbf{R}g \mathbf{N}_{l,m}(kr, \theta, \phi) \mathbf{N}_{l,m}(kr', \theta', \phi') & \text{for } r < r' \end{cases}, \quad (2.70)$$

where \bar{I} is the identity matrix.

The irrotational terms, which are normally present in this equation have been removed, since they will not contribute due to the curl operations in Equation 2.69.

Moreover, we need to be careful with this substitution: while the Green's dyadic has no singularities, the Green's function given by Equation 2.67 does at $r = r'$. As a result, the expansion is only valid within an inscribed sphere and outside a circumscribed sphere, because these are the only cases in which $r \neq r'$ as shown in Figure 2.8.

Fortunately, this problem can be solved by using the concept of analytic continuation. How this is done is outside of the scope of this thesis, but it has been shown in the original paper on the T matrix method by Waterman[31]. By reversing the order of integration and differentiation and calculating the double curl in Equation 2.69, we get the following expression for the scattered field:

$$\mathbf{E}^{\text{sca}} = \int_S \mathbf{J}(\mathbf{r}') \frac{i}{\omega \epsilon} \left[\nabla(\nabla \cdot \bar{G}) - \nabla^2 \bar{G} \right] dS'. \quad (2.71)$$

The divergence² of the Green's dyadic is zero, as it is composed of \mathbf{M} and \mathbf{N} vectors, which are the curls of different functions (Equation 2.34 and Equation 2.35). Using Equation 2.70 in Equation 2.71, we get

$$\mathbf{E}^{\text{sca}} = \frac{-ik^2}{\omega\epsilon} \int_S \mathbf{J}(\mathbf{r}') \cdot \bar{\mathbf{G}}(\mathbf{r}, \mathbf{r}') dS'. \quad (2.72)$$

We expand the incident field into regular spherical harmonics, as before:

$$\mathbf{E}^{\text{inc}} = \sum_{l=0}^{\infty} \sum_{m=-l}^l a_{l,m}^{\text{inc}} \mathbf{RgN}(kr, \theta, \phi) + b_{l,m}^{\text{inc}} \mathbf{RgM}(kr, \theta, \phi). \quad (2.73)$$

Combining Equation 2.70, Equation 2.72 and Equation 2.73, we get a set of equations for the coefficients of the incident field:

$$\begin{bmatrix} a_{l,m}^{\text{inc}} \\ b_{l,m}^{\text{inc}} \end{bmatrix} = -\frac{k^3}{\omega\epsilon} \int_S \mathbf{J}(\mathbf{r}') \cdot \begin{bmatrix} \mathbf{M}_{l,m}(k, \mathbf{r}') \\ \mathbf{N}_{l,m}(k, \mathbf{r}') \end{bmatrix} dS' \text{ for } r \in \Omega. \quad (2.74)$$

Next, we expand the surface current density in regular spherical vector harmonics. We start by expanding the electric field:

$$\mathbf{E} = \sum_{l=0}^{\infty} \sum_{m=-l}^l a_{l,m}^{\text{par}} \mathbf{RgN}(k_{\text{par}} r, \theta, \phi) + b_{l,m}^{\text{par}} \mathbf{RgM}(k_{\text{par}} r, \theta, \phi). \quad (2.75)$$

From the electric field, we can calculate the magnetic field using Equation 2.35 and Equation 2.36:

$$\mathbf{H} = \frac{1}{i\omega\mu} \nabla \times \mathbf{E} = -i \sqrt{\frac{\epsilon}{\mu}} \sum_{l=0}^{\infty} \sum_{m=-l}^l a_{l,m}^{\text{par}} \mathbf{RgM}(k_{\text{par}} r, \theta, \phi) + b_{l,m}^{\text{par}} \mathbf{RgN}(k_{\text{par}} r, \theta, \phi). \quad (2.76)$$

Substituting $\mathbf{J} = \hat{\mathbf{n}} \times \mathbf{H}$ and the above equation in Equation 2.74 and using the scalar triple product, we get for the coefficients in the sum

$$a_{l,m}^{\text{inc}} = -i a_{l,m}^{\text{par}} k^2 \int_S \hat{\mathbf{n}} \cdot \mathbf{RgN}_{l,m} \times \mathbf{M}_{l,m} dS' - i b_{l,m}^{\text{par}} k^2 \int_S \hat{\mathbf{n}} \cdot \mathbf{RgM}_{l,m} \times \mathbf{M}_{l,m} dS', \quad (2.77)$$

$$b_{l,m}^{\text{inc}} = -i a_{l,m}^{\text{par}} k^2 \int_S \hat{\mathbf{n}} \cdot \mathbf{RgN}_{l,m} \times \mathbf{N}_{l,m} dS' - i b_{l,m}^{\text{par}} k^2 \int_S \hat{\mathbf{n}} \cdot \mathbf{RgM}_{l,m} \times \mathbf{N}_{l,m} dS'. \quad (2.78)$$

From these equations, the coefficients of the magnetic field and thus the surface current density \mathbf{J} can be calculated. From there, the scattered field can be calculated using Equation 2.72. If we expand the scattered field into vector spherical harmonics as in Equation 2.48, the coefficients are related to the coefficients of the internal field through

$$a_{l,m}^{\text{sca}} = -i a_{l,m}^{\text{par}} k^2 \int_S \hat{\mathbf{n}} \cdot \mathbf{RgN}_{l,m} \times \mathbf{RgM}_{l,m} dS' - i b_{l,m}^{\text{par}} k^2 \int_S \hat{\mathbf{n}} \cdot \mathbf{RgM}_{l,m} \times \mathbf{RgM}_{l,m} dS', \quad (2.79)$$

$$b_{l,m}^{\text{sca}} = -i a_{l,m}^{\text{par}} k^2 \int_S \hat{\mathbf{n}} \cdot \mathbf{RgN}_{l,m} \times \mathbf{RgN}_{l,m} dS' - i b_{l,m}^{\text{par}} k^2 \int_S \hat{\mathbf{n}} \cdot \mathbf{RgM}_{l,m} \times \mathbf{RgN}_{l,m} dS'. \quad (2.80)$$

²See Appendix A for the definition of the divergence of a tensor

Combining Equation 2.77, Equation 2.78, Equation 2.79 and Equation 2.80, we can relate the coefficient of the scattered field to the coefficients of the incident field. Truncating the sums, this can be written as a matrix operation, where the matrix components are composed of integrals over the surface of the scatterer. With that, we have succeeded in our objective to write the scattered field according to Equation 2.59.

The method to calculate the scattered field produced by a dielectric particle is analogous to the discussed procedure. The surface integrals will include a contribution of the magnetic surface current \mathbf{M} . The scattered field is then given by

$$\mathbf{E}^{\text{sca}} = -\nabla \times \mathbf{F} + \frac{i}{\omega\mu\epsilon} \nabla \times \nabla \times \mathbf{A} \quad (2.81)$$

instead of Equation 2.65, with

$$\mathbf{F} = \int_S \mathcal{M}(\mathbf{r}') G(\mathbf{r}, \mathbf{r}') dS'. \quad (2.82)$$

It is important to note that if the sums over l, m in Equation 2.73 and Equation 2.75 run from 1 to ∞ , this method gives an analytical and exact relation between the incident and scattered fields. Calculating these however, requires truncation of these sums over l . The maximum value of N which is calculated is determined by the size of the geometry that is considered compared to the wavelength. As a rule of thumb, $N \geq ka$ with k the wavenumber and a the smallest radius of a sphere circumscribing the geometry.[33]

Furthermore, since the T matrix is calculated using an inverted matrix, the precision at which this inverted matrix is calculated is important. Since the original matrix can have very small but important contributions, these details can be lost due to truncation of the computed number because of the limited number of bits used in the calculation. In other words, the condition number of the matrix that needs to be inverted is very large.

This is especially important for geometries with large aspect ratios, as such geometries deviate the most from a sphere. Intuitively, this makes sense; it is awkward to use spherical functions to describe the scattering of an object that is not spherical. This makes it so that the used expansion in spherical harmonics requires more terms, which introduces computational instabilities. For geometries with sharp corners, this method is completely incompatible.

2.5. FINITE ELEMENT METHODS

Another method of solving scattering problems is by the use of Finite Element Methods (FEM). For scattering problems the vector wave-equation is solved by splitting the scatterer and a region around the scatterer up in smaller parts called finite elements. The assumption is made that as the elements become smaller, the approximated solution converges towards the solution of the problem. Thus, to obtain a usable solution, the elements need to be sufficiently small. Furthermore, the correct boundary conditions and material properties need to be prescribed.

Software packages such as COMSOL are used to simplify this process. Within the software, the equations to be solved, material properties and boundary conditions can be submitted. The separation of the region into different elements (called meshing) is done by the software, taking into account the shape of the scatterer and the material properties. Generally, at least 20 elements per wavelength in the material are needed. Sometimes, some adjustments need to be made by the user to ensure that the calculations by the software converge to an accurate solution. The downside of using such software is that, especially for three dimensional geometries, it takes a lot of computational resources to solve and hence also a lot of time. Furthermore, the size of the considered scatterer is limited by the available computational resources.

2.6. MULTIPOLE ANALYSIS

It should be noted that with all of the above methods, only Mie theory can provide a decomposition of multipole moments. These multipole moments can be a great tool in understanding the origin of obtained far-field scatter patterns. Methods exist which overcome this shortcoming, even allowing results from FEM simulations to be used to calculate the individual multipole contributions. One method derives exact analytical expressions for the multipole expressions. An expansion of spherical Bessel functions is then used to make the equations more usable. A second method decomposes a volume into many different dipoles. From there, using a Taylor expansion, expressions for the multipole moments are derived.

2.6.1. EXACT MULTIPOLAR DECOMPOSITION

This method has been developed by researchers from the Karlsruhe Institute of Technology in a series of papers[37–39]. They start by considering a current density in some region of space embedded in a homogeneous isotropic medium. We assume that the current density is bounded, hence for some $R > 0$, the current density distribution $\mathbf{J}(\mathbf{r}, t) = 0$ for $|\mathbf{r}| > R$. In the context of this thesis, this bounded region would include the scatterer. The current density can be written in terms of a Fourier transform (both in time and space):[37]

$$\mathbf{J}(\mathbf{r}, t) = \text{Re} \left[\frac{1}{\sqrt{2\pi}} \int_0^\infty \mathbf{J}_\omega(\mathbf{r}) e^{-i\omega t} d\omega \right], \quad (2.83)$$

$$= \frac{1}{(2\pi)^2} \text{Re} \left[\int_0^\infty e^{-i\omega t} d\omega \int_0^\infty \mathbf{J}_\omega(\boldsymbol{\kappa}) e^{i\boldsymbol{\kappa} \cdot \mathbf{r}} d^3 \boldsymbol{\kappa} \right], \quad (2.84)$$

with $\mathbf{J}_\omega(\boldsymbol{\kappa})$ the 3D Fourier transform in space given by

$$\mathbf{J}_\omega(\boldsymbol{\kappa}) = \frac{1}{\sqrt{(2\pi)^3}} \int \mathbf{J}_\omega(\mathbf{r}) e^{-i\boldsymbol{\kappa} \cdot \mathbf{r}} d^3 \mathbf{r}. \quad (2.85)$$

Here, $\boldsymbol{\kappa}$ is the vector representing reciprocal space, not to be confused with the wavenumber \mathbf{k} .

Now, we require the theorem from the paper Fernandez-Corbaton et. al.[37] that is a critical part of the derivation: The (transverse) electromagnetic fields outside the source are uniquely determined by the complex amplitudes of the 3D Fourier transform

of $J_\omega(\boldsymbol{\kappa})$, where the spatial frequencies $\boldsymbol{\kappa}$ are on the sphere with radius $|\boldsymbol{\kappa}| = \omega/c$ in reciprocal space.³ The Fourier transform of the current density can then be written as

$$\mathbf{J}_\omega(\hat{\boldsymbol{\kappa}}) = \frac{1}{\sqrt{(2\pi)^3}} \int \mathbf{J}_\omega(\mathbf{r}) e^{-i\frac{\omega}{c}\hat{\boldsymbol{\kappa}}\cdot\mathbf{r}} d^3\mathbf{r}. \quad (2.86)$$

The current density is then decomposed into an orthonormal basis of spherical harmonics, these are the three families of multipolar functions in momentum space[39]:

$$\mathbf{J}_\omega(\hat{\boldsymbol{\kappa}}) = \sum_{l,m} a_{l,m}^\omega \mathbf{Z}_{l,m}(\hat{\boldsymbol{\kappa}}) + b_{l,m}^\omega \mathbf{X}_{l,m}(\hat{\boldsymbol{\kappa}}) + c_{l,m}^\omega \mathbf{W}_{l,m}(\hat{\boldsymbol{\kappa}}), \quad (2.87)$$

with

$$\mathbf{X}_{l,m}(\hat{\boldsymbol{\kappa}}) = \frac{1}{\sqrt{l(l+1)}} \mathbf{L} Y_{l,m}(\hat{\boldsymbol{\kappa}}), \quad (2.88)$$

$$\mathbf{Z}_{l,m}(\hat{\boldsymbol{\kappa}}) = i\hat{\boldsymbol{\kappa}} \times \mathbf{X}_{l,m}(\hat{\boldsymbol{\kappa}}), \quad (2.89)$$

$$\mathbf{W}_{l,m}(\hat{\boldsymbol{\kappa}}) = \hat{\boldsymbol{\kappa}} Y_{l,m}(\hat{\boldsymbol{\kappa}}), \quad (2.90)$$

where \mathbf{L} is \hbar^{-1} times the angular momentum operator of wave mechanics given by[27]

$$\mathbf{L} = \frac{1}{i}(\mathbf{r} \times \nabla) \quad (2.91)$$

The $\mathbf{Z}_{l,m}$, $\mathbf{X}_{l,m}$ and $\mathbf{W}_{l,m}$ terms are associated with the $N_{l,m}$, $\mathbf{M}_{l,m}$ and $\mathbf{L}_{l,m}$ vector spherical harmonics[39] we saw earlier in Section 2.3. We also saw that only the $N_{l,m}$ and $\mathbf{M}_{l,m}$ terms contribute to radiating electromagnetic waves, so we will disregard $c_{l,m}^\omega$ when deriving the multipole contributions to the scattered field. However, they cannot be omitted from Equation 2.87 as the considerations for the scattered field do not apply to the current density vector. That is to say, in general, the current density is not free of divergence. The coefficients in Equation 2.87 are then determined by:

$$a_{l,m}^\omega = \int \mathbf{Z}_{lm}^\dagger(\hat{\boldsymbol{\kappa}}) \mathbf{J}_\omega(\hat{\boldsymbol{\kappa}}) d\hat{\boldsymbol{\kappa}}, \quad (2.92)$$

$$b_{l,m}^\omega = \int \mathbf{X}_{lm}^\dagger(\hat{\boldsymbol{\kappa}}) \mathbf{J}_\omega(\hat{\boldsymbol{\kappa}}) d\hat{\boldsymbol{\kappa}}, \quad (2.93)$$

where \dagger indicates the conjugate transpose.

Substituting Equation 2.86 in Equation 2.92 and Equation 2.93 results in

$$a_{l,m}^\omega = \frac{1}{\sqrt{(2\pi)^3}} \int \mathbf{Z}_{lm}^\dagger(\hat{\boldsymbol{\kappa}}) \int \mathbf{J}_\omega(\mathbf{r}) e^{-i\frac{\omega}{c}\hat{\boldsymbol{\kappa}}\cdot\mathbf{r}} d^3\mathbf{r} d\hat{\boldsymbol{\kappa}}, \quad (2.94)$$

$$b_{l,m}^\omega = \frac{1}{\sqrt{(2\pi)^3}} \int \mathbf{X}_{lm}^\dagger(\hat{\boldsymbol{\kappa}}) \int \mathbf{J}_\omega(\mathbf{r}) e^{-i\frac{\omega}{c}\hat{\boldsymbol{\kappa}}\cdot\mathbf{r}} d^3\mathbf{r} d\hat{\boldsymbol{\kappa}}. \quad (2.95)$$

The exponential in these expressions can be expanded in spherical harmonics using the plane-wave expansion, which is given by[37]

$$e^{-i\frac{\omega}{c}\hat{\boldsymbol{\kappa}}\cdot\mathbf{r}} = 4\pi \sum_{l'm'} (-i)^{l'} Y_{l'm'}^*(\hat{\mathbf{r}}) Y_{l'm'}(\hat{\boldsymbol{\kappa}}) j_{l'}(kr), \quad (2.96)$$

³This theorem originates from a paper by Devaney and Wolf[40], which uses results from an earlier paper by Whittaker[41]

with $\hat{\mathbf{r}} = \frac{\mathbf{r}}{|\mathbf{r}|}$ and where * indicates the complex conjugate. This results in the following expressions:

$$a_{lm}^\omega = \frac{4\pi}{\sqrt{(2\pi)^3}} \sum_{l'm'} (-i)^{l'} \int \mathbf{Z}_{lm}^\dagger(\hat{\mathbf{k}}) Y_{l'm'}(\hat{\mathbf{k}}) d\hat{\mathbf{k}} \int \mathbf{J}_\omega(\mathbf{r}) Y_{l'm'}^*(\hat{\mathbf{r}}) j_l(kr) d^3\mathbf{r}, \quad (2.97)$$

$$b_{lm}^\omega = \frac{4\pi}{\sqrt{(2\pi)^3}} \sum_{l'm'} (-i)^{l'} \int \mathbf{X}_{lm}^\dagger(\hat{\mathbf{k}}) Y_{l'm'}(\hat{\mathbf{k}}) d\hat{\mathbf{k}} \int \mathbf{J}_\omega(\mathbf{r}) Y_{l'm'}^*(\hat{\mathbf{r}}) j_l(kr) d^3\mathbf{r}. \quad (2.98)$$

The resulting expressions for the coefficients of the electric and magnetic dipoles ($l = 1$) then become:

$$\begin{bmatrix} a_\omega^{11} \\ a_\omega^{10} \\ a_\omega^{1-1} \end{bmatrix} = -\frac{1}{\pi\sqrt{3}} \int \mathbf{J}_\omega(\mathbf{r}) j_0(kr) d^3\mathbf{r} \quad (2.99)$$

$$\begin{bmatrix} b_\omega^{11} \\ b_\omega^{10} \\ b_\omega^{1-1} \end{bmatrix} = -\frac{\sqrt{3}}{2\pi} \int \hat{\mathbf{r}} \times \mathbf{J}_\omega(\mathbf{r}) j_1(kr) d^3\mathbf{r} \quad (2.100)$$

By using the small source approximation, and using a Taylor expansion for the spherical Bessel functions in the above equations ($j_0(kr) \approx 1$ and $j_1(kr) \approx kr/3$), we recover the well known equations for the electric and magnetic dipole[26]:

$$\begin{bmatrix} a_\omega^{11} \\ a_\omega^{10} \\ a_\omega^{1-1} \end{bmatrix} = -\frac{1}{\pi\sqrt{3}} \int \mathbf{J}_\omega(\mathbf{r}) d^3\mathbf{r} = -\frac{1}{\pi\sqrt{3}} \mathbf{p} \quad (2.101)$$

$$\begin{bmatrix} b_\omega^{11} \\ b_\omega^{10} \\ b_\omega^{1-1} \end{bmatrix} = -\frac{k}{2\pi\sqrt{3}} \int \mathbf{r} \times \mathbf{J}_\omega(\mathbf{r}) d^3\mathbf{r} = -\frac{k}{\pi\sqrt{3}} \mathbf{m} \quad (2.102)$$

Comparing these equations with [Equation 2.99](#) and [Equation 2.100](#) we arrive at the exact equations for the electric and magnetic dipoles:

$$\mathbf{p}_{exact} = \int \mathbf{J}_\omega(\mathbf{r}) j_0(kr) d^3\mathbf{r}, \quad (2.103)$$

$$\mathbf{m}_{exact} = \frac{3}{2} \int \mathbf{r} \times \mathbf{J}_\omega(\mathbf{r}) \frac{j_1(kr)}{kr} d^3\mathbf{r}. \quad (2.104)$$

Similarly, the exact expressions can be recovered for the quadrupole contributions:

$$Q_{\alpha\beta}^e = \frac{-3}{i\omega} \left[\int \left[3(r_\beta J_\alpha^\omega + J_\beta^\omega r_\alpha) - 2(\mathbf{r} \cdot \mathbf{J}_\omega) \delta_{\alpha\beta} \right] \frac{j_1(kr)}{kr} d^3\mathbf{r} \right. \\ \left. + 2k^2 \int \left[5r_\alpha r_\beta (\mathbf{r} \cdot \mathbf{J}_\omega) - (r_\alpha J_\beta + r_\beta J_\alpha) r^2 - r^2 (\mathbf{r} \cdot \mathbf{J}_\omega) \delta_{\alpha\beta} \right] \frac{j_3(kr)}{(kr)^3} d^3\mathbf{r} \right], \quad (2.105)$$

$$M_{\alpha\beta}^e = \int \left[r_\alpha (\mathbf{r} \times \mathbf{J}_\omega)_\beta + r_\beta (\mathbf{r} \times \mathbf{J}_\omega)_\alpha \right] \frac{j_2(kr)}{(kr)^2} d^3\mathbf{r}. \quad (2.106)$$

The papers referenced do not include the octupole expressions. As these do have contributions for the size of particles we will consider in [Chapter 3](#), we have calculated

these ourselves, using the method laid out in the papers. The results of these are shown in [Section A.7](#).

The total scattering cross section is then given by[38]

$$\sigma_{\text{sca}} \approx \frac{k_0^4}{6\pi\epsilon_0^2|\mathbf{E}_{\text{incl}}|^2} |\mathbf{p}|^2 + \frac{k_0^2 k^2}{6\pi\epsilon_0^2 c |\mathbf{E}_{\text{incl}}|^2} |\mathbf{m}|^2 + \frac{k_0^4 k^2}{720\pi\epsilon_0^2 |\mathbf{E}_{\text{incl}}|^2} |\overline{\mathbf{Q}}|^2 + \frac{k_0^2 k^4}{720\pi\epsilon_0^2 c^2 |\mathbf{E}_{\text{incl}}|^2} |\overline{\mathbf{M}}|^2 \quad (2.107)$$

2.6.2. THE DECOMPOSED DISCRETE DIPOLE APPROXIMATION

Since an analytical solution to the optical response of a nanoparticle only exists for special cases (such as Mie theory for spherical particles), numerical analysis tools such as FEM and FDTD are used to calculate the fields. In the general case however, with these methods it is difficult to distinguish the resonance frequencies related to the different multipole moments. The decomposed discrete dipole approximation (DDDA) is a method which makes this possible.

The idea of the discrete dipole approximation is to consider an arbitrary-shaped nanoparticle as a collection of point dipoles at different positions according to the geometry of the particle[42, 43]. The dipole moment induced by each point dipole can then be expressed as

$$\mathbf{p}_j = \alpha_p \mathbf{E}_0(\mathbf{r}_j) + \alpha_p \frac{k_0^2}{\epsilon_0} \sum_{l \neq j}^N \overline{\mathbf{G}}(\mathbf{r}_j, \mathbf{r}_l) \mathbf{p}_l, \quad (2.108)$$

with \mathbf{E}_0 the incident electric field, α_p the polarizability of the scatterer and $\overline{\mathbf{G}}$ the Green's tensor of the medium surrounding the scatterer. Using the optical theorem, the extinction cross section can be found to be[42]

$$\sigma_{\text{ext}} = \frac{k}{\epsilon_0 \epsilon_{\text{med}} |\mathbf{E}_0|^2} \text{Im} \sum_{j=1}^N \mathbf{E}_0^*(\mathbf{r}_j) \cdot \mathbf{p}_j. \quad (2.109)$$

The expression which is summed over can then be Taylor expanded around \mathbf{r}_0 . From the obtained terms, the multipole expressions can be recovered.

2.6.3. MIXING OF MULTIPOLE CONTRIBUTIONS

As we have seen in [Section 2.3](#), the different resonances that the nanoparticles exhibit have an associated far-field scatter pattern. These scatter patterns can be combined to create non-trivial scattering.

The first investigation of combining multipole components was done by Kerker et al.[44]. In this paper, researchers investigated scattering in the special case where the relative electric permittivity and magnetic permeability of a sphere are equal (i.e. $\epsilon = \mu$). The scattered field can be calculated using Mie theory as in [Section 2.3](#). As a result, the a_l and b_l coefficients of [Equation 2.54](#) are equal. An expression can then be derived for the cross section related to the back scattered field:

$$\sigma_{\text{bsc}} = \frac{\pi}{k^2} \left| \sum_{l=1}^{\infty} (2l+1)(-1)^l (a_l - b_l) \right|^2. \quad (2.110)$$

The case described above, where $a_l = b_l$, is called the Kerker condition. This is the case where the electric and magnetic dipole, quadrupole, octupole, et cetera are equal, resulting in zero backscattering. However, different combinations are possible, which results in more interesting scattering behaviour. For example, conditions could be reached where the coefficient for the electric quadrupole and magnetic dipole is equal. This is an example of the extended Kerker conditions. These will be explored further in [Chapter 3](#).

2.7. SUMMARY

In this chapter, we have presented several methods of calculating the scattered field by a homogeneous particle. Most of the methods are numerical, as the cases where an analytical solution can be found are limited to the infinite cylinder and the perfect sphere.

Furthermore, we have seen that the decomposition in spherical vector harmonics is a powerful tool to determine the scattered far-field, and provides an intuitive way to think about how the far field scattering pattern is related to resonances in the particle. Through the spherical vector harmonics, the scattered field can be decomposed into electric and magnetic dipoles, quadrupoles, octupoles and so on. When the magnitude of different multipole contributions are chosen in a special way, non-trivial far-field patterns can be generated.

The advantages and disadvantages of the discussed methods in this chapter are summarized in [Table 2.1](#).

Method	Advantages	Disadvantages
Born approximation	Analytical solution	Only valid for very low contrast
Mie theory	Analytical solution	Only valid for (multilayer) spheres and infinite cylinders
Transfer matrix method	Fast numerical method	Only applicable in spheroid geometries with limited aspect ratios
Finite Element Methods	Applicable to any geometry and material Commercial software available for easy problem definition	Long computation times
Exact multipolar decomposition	Analytical expressions for multipole resonances	Internal fields need to be known
Decomposed discrete dipole approximation	Numerical method which gives multipole decomposition	Long computation times

Table 2.1: Table of methods to solve scattering problems and their advantages and disadvantages.

In the next chapter, we will use the software COMSOL which uses FEM to calculate the fields scattered by a nanoparticle. The multipole decomposition is then done using the analytical expression discussed in [Section 2.6.1](#). The reason for choosing COMSOL is because it makes the problem definition very easy, which is too great of an advantage to ignore. Because we will be trying many different geometries and materials, the flexibility of the software is very beneficial. The expressions of the multipole decomposition can also be directly implemented in the software, providing us with a good understanding of the scattering characteristics of the particles we simulate. With this, we will be able to come to a design of a nanoparticle with desired scattering properties.

3

DIRECTIONAL SCATTERING BY NANOSTRUCTURES

“ Physics is essentially an intuitive and concrete science.
Mathematics is only a means for expressing
the laws that govern phenomena.

Albert Einstein[9]”

IN [Chapter 2](#), we have introduced different methods one can use to solve a scattering problem. In this chapter, we will apply some of these techniques to get more understanding of the scattering properties of nanoparticles and their application to diffraction gratings¹. This is not an easy pursuit; in most cases, there is no clear relation between the shape of nanoparticles and their scatter behaviour. By calculating the scatter pattern of different nanoparticles, we will attempt to derive a rule of thumb for the design of a nanoparticle which scatters light in a specific direction.

First, we will investigate the effects of using different materials, sizes and geometries of particles in [Section 3.1](#). Then, we take a look at composite nanoparticles in [Section 3.2](#), where the use of multiple materials gives us more degrees of freedom. From there, we will specifically look at the application of composite nanoparticles in a grating configuration in [Section 3.3](#).

¹[Section 3.2](#) of this chapter is the extended version of the methods in our paper *Broadband directional scattering through a phase difference acquired in composite nanoparticles*[45], while [Section 3.3](#) is the extended version of the methods in our paper *Method for designing highly efficient composite transmission gratings*[46]

3.1. SCATTERING PROPERTIES OF NANOPARTICLES

The research into scattering by nanoparticles has taken off in the last two decades thanks to the field of plasmonics, in which the light-matter interaction of metallic nanoparticles has been investigated. Metallic nanoparticles can support very strong resonances in the visible spectrum, which has applications in spectroscopy [47], sensing [48] and LEDs [3]. The downside of metallic nanoparticles is that a lot of energy is absorbed by the material. Looking for further applications, research has shifted to dielectric nanoparticles which can also support resonances. These resonances are generally weaker, but where the plasmonic resonances are only electric, dielectric nanoparticles can additionally support magnetic resonances.

A good way to get a quick understanding about these resonances is by going through some examples of metallic and dielectric nanoparticles. By using the multipole analysis presented in Section 2.6, the scattering properties are easily understood. We will consider three parameters separately: the effect of material choice, size and geometry.

3.1.1. EFFECT OF DIFFERENT MATERIALS

METALS

Following the chronological advance of this area of research, we will start with metallic nanoparticles. Metals have a complex permittivity function and therefore have losses associated with them. Materials which are used often include gold, aluminum and silver, as these material exhibit resonances in the visible spectrum.

As a case study, we start with a silver nanoparticle following the methods described in Section 2.5. Let us consider a spherical silver nanoparticle in vacuum with a diameter of 120 nm. A linearly polarized plane-wave is incident upon the particle with wavelength in the optical spectrum. Using the software COMSOL we can calculate the near field. Next, using the equations found in Section 2.6.1, we can calculate scattering cross sections of the different multipole contributions and the extinction cross section. The results are shown in Figure 3.1. In Appendix B the specifics for the simulations can be found.

From the figure, we can see the strong resonance (centered around 420 nm) that is typical for a metallic nanoparticle. This resonance is mainly caused by the electric dipole. Another peak can be observed at around 360 nm, which has contributions both of the electric dipole and quadrupole. For this peak, we can see a distinct difference between the sum of the scattering cross sections and the extinction cross section. The difference being the amount of light being absorbed by the particle (see Section 2.1 for details).

Also note the y -axis; while for macroscopic spheres the scattering cross section is twice the geometrical cross section (see Section 2.1), for a silver nanoparticle it is over six times the geometrical cross section. From this, one can understand why plasmonics is such an active field of study. If we look at the scattered near field and far field at resonance that are shown in Figure 3.2, we can recognize the patterns related to the spherical harmonics shown in Figure 2.6. The near field and the far field at resonance ($\lambda = 415$ nm) show the characteristic shape of an electric dipole.

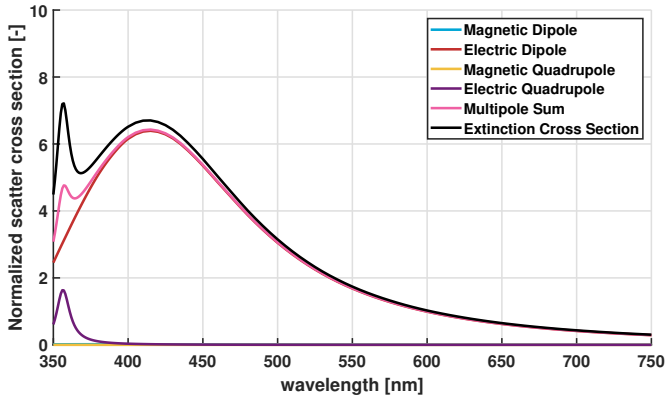


Figure 3.1: Plot of the multipole scattering cross section of the resonances being supported by a silver nanosphere with a diameter of 120 nm. The cross sections are normalized with respect to the geometrical cross section.

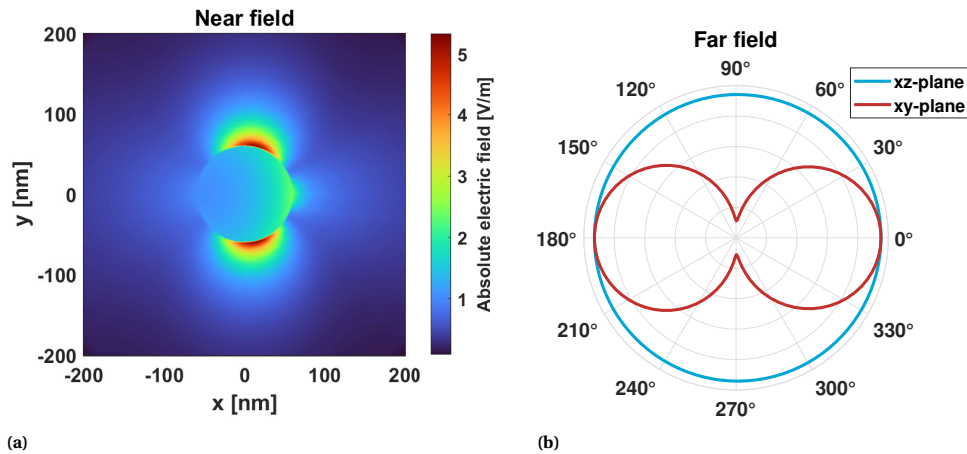


Figure 3.2: (a) Scattered electric near field and (b) far field patterns of a silver nanosphere with a diameter of 120 nm, when a y polarized plane-wave is incident travelling in the x direction. The fields are shown at resonance of the electric dipole, occurring at a wavelength of $\lambda = 415$ nm.

DIELECTRICS

The other class of materials are dielectrics, for which the permittivity is (mostly) real. For dielectrics, we will differentiate between high-index dielectrics and a low-index dielectrics. Commonly used high-index dielectrics include galliumarsenide (GaAs), (crystalline) silicon (Si) and galliumphosphide (GaP). Commonly used low-index dielectrics include titania (TiO_2), aluminumoxide (Al_2O_3 or sapphire) and silica (SiO_2) or glass.

3

We will first look at a high-index dielectric. We will take the same configuration as before, but replace the silver particle by one made of crystalline silicon (the diameter of the sphere stays the same: 120 nm). The results are shown in [Figure 3.3](#).

What stands out immediately in contrast to the metallic nanoparticle ([Figure 3.1](#)), is the presence of the magnetic dipole. This is a great advantage of dielectrics: since this class of materials can support magnetic modes, more control over the interaction with light is possible. Also note the magnitude of the normalized scattering cross section, which is comparable to the silver particle at resonance. At resonance ($\lambda = 521$ nm), the magnetic dipole can be recognized in the near field and far field plots shown in [Figure 3.4](#).

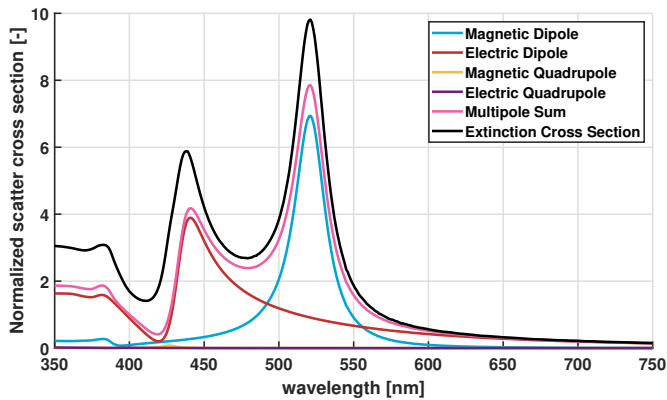


Figure 3.3: Plot of the multipole scattering cross section of the resonances being supported by a silicon nanosphere with a diameter of 120 nm. The cross sections are normalized with respect to the geometrical cross section.

Note the difference in the near field. For a metallic particle, the fields cannot penetrate into the particle, while this is possible for a dielectric particle. This is the reason why magnetic resonances can be supported by dielectric particles. Also note the asymmetry in the x -direction in both the near field and the far field; this is because these fields are not solely determined by the magnetic dipole. From [Figure 3.3](#) we can see that there is also an electric dipole contribution at the wavelength the fields are plotted.

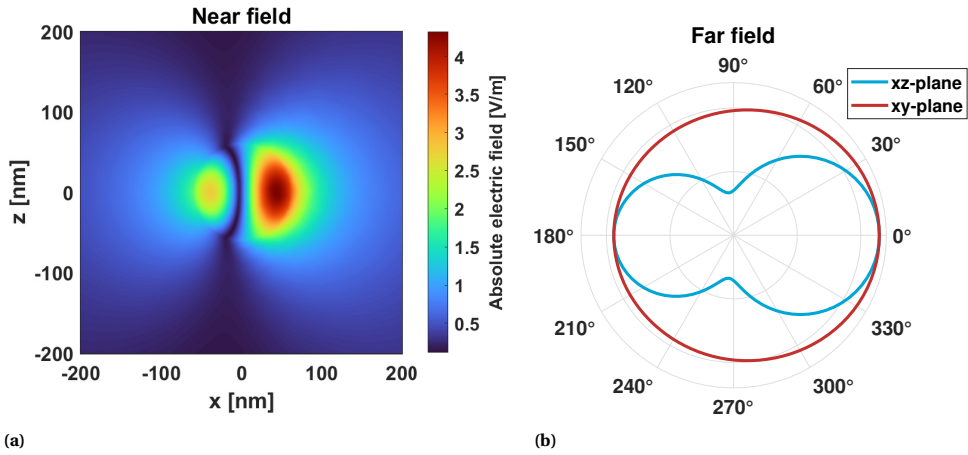


Figure 3.4: (a) Scattered electric near field and (b) far field patterns of a silicon nanosphere with a diameter of 120 nm, when a y -polarized plane-wave is incident travelling in the x -direction. The fields are shown at resonance of the magnetic dipole, occurring at a wavelength of $\lambda = 521$ nm.

What happens if the index of the particle is lowered? Let us change the material to titania, which has an index of around 2.6 versus 4 for silicon in the visible spectrum. Because the index is so much lower, we will have to compensate by making the particle larger so that the resonances stay in the visible spectrum. Therefore, we will change the diameter from 120 nm to 240 nm.

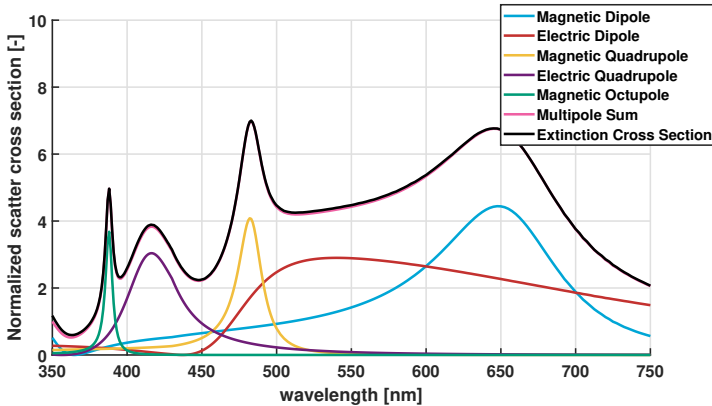


Figure 3.5: Plot of the multipole scattering cross section of the resonances being supported by a titania nanosphere with a diameter of 240 nm. The cross sections are normalized with respect to the geometrical cross section.

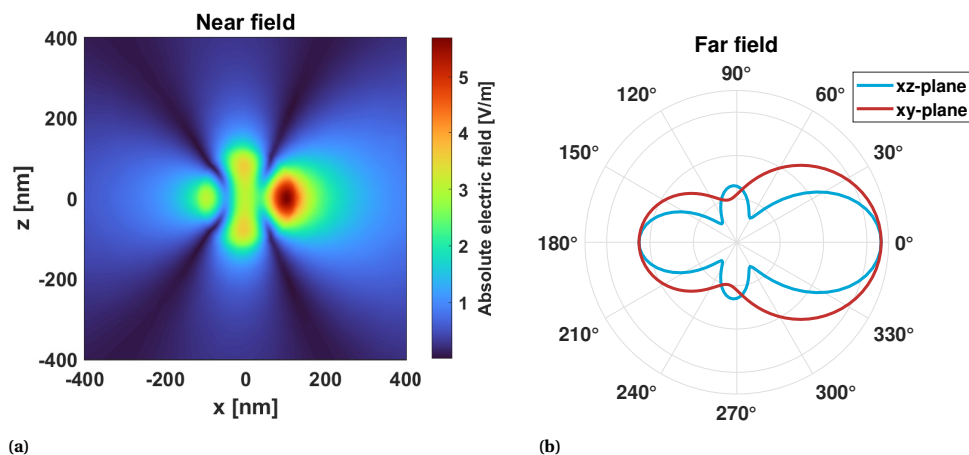


Figure 3.6: (a) Scattered electric near field and (b) far field patterns of a titania nanosphere with a diameter of 240 nm, when a y -polarized plane-wave is incident travelling in the x -direction. The fields are shown at a wavelength of $\lambda = 483$ nm.

While resonance peak can still be observed, one can see that these peaks are composed of multiple underlying multipole contributions. This is due to the lowering of the index: resonance peaks get spread out over a larger bandwidth, and as a result, different multipole resonances will overlap. This is most obvious for the electric dipole, where no real peak can be discerned. While for the previous examples, clear resonances could be seen and their associated near field and far field distributions were easily recognized. This is not the case here as can be seen in Figure 3.6, where the fields are plotted at $\lambda = 483$ nm. A far field distribution as seen here is characteristic for low-index particle in the Mie scattering regime. If we would be using silica instead (refractive index of ~ 1.46), we would observe further broadening and even more overlap of the resonances.

3.1.2. EFFECT OF SIZE

The size of the nanoparticles of the previous section were not chosen by accident, size has an important impact on the scattering properties of a particle. Were we to scale up the particle to a macroscopic scale, we would expect that nothing really interesting happens. The *scattering* can then be determined through simple reflection and refraction laws.

Scaling the particle all the way down, it occupies such a small region of space that barely any scattering can be observed. So what happens in between? As we have already seen; the scattering is governed by resonances. So the question becomes: what happens to these resonances when the size of the particle is changed?

Of course, when we talk about small or large in physics, it always needs to be compared to something. For scattering particles, the comparison is the wavelength of the light. More accurately, the wavelength of the light inside the particle. This makes sense: if the particle is very large compared to the wavelength, the incident light can be approximated by a ray, so we are in the domain of geometrical optics. On the other

hand, if the particle is very small compared to the wavelength, the particle can be considered as just a small perturbation, resulting in hardly any scattering.

These considerations make it possible to see the effect of size not by changing the actual size of the particle, but by changing the incident wavelength. So, to the the effect of size, like before, let us take a spherical particle with a diameter of $d = 1 \mu\text{m}$. We take the refractive index to be a constant $n = 4$, and sweep over a large bandwidth for the incident wavelength from 500 nm to 6000 nm.

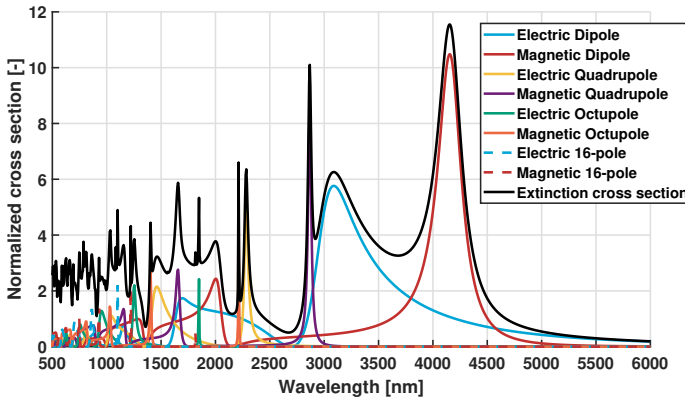


Figure 3.7: Plot of the multipole scattering cross section of the resonances being supported by a nanosphere with refractive index $n = 4$ and a diameter of $1 \mu\text{m}$. The cross sections are normalized with respect to the geometrical cross section. While higher order modes than 16-poles are supported for wavelengths shorter than 1200 nm, they are not shown in this graph.

In the graph (Figure 3.7), small particles would be on the right, while large particles are on the left. We see that the cross section seems to converge to two times the geometrical cross section for large particles (short wavelengths) as expected from Section 2.1. Furthermore, for small particles (long wavelengths) the amount of scattering is very low. Notably, the only contribution is the electric dipole. This is the so-called Rayleigh scattering regime, the same scattering that is responsible for the blue colour of the sky.

Now, let us shift our focus to what happens in between, going from small to large particles (from right to left on the graph of Figure 3.7). We see that initially there are well defined resonance peaks, as we would expect from a high index dielectric particle. First, we encounter the magnetic dipole, and then the electric dipole resonance peak. If we keep going to larger and larger particles, we encounter higher order multipoles, with very sharp peaks. Moving even further, we see that the electric and magnetic dipoles come back, until at a certain point the scattering is determined by a complex sum of different multipole contributions.

As we have seen in the previous section, for low-index particles, we would expect this mixing of multipole contributions to be worse. Indeed, if we look at Figure 3.8, where the refractive index $n = 1.5$, we see that this is the case. Note that we have changed the size of the particle to be $d = 2 \mu\text{m}$, to compensate for the change in refractive index.

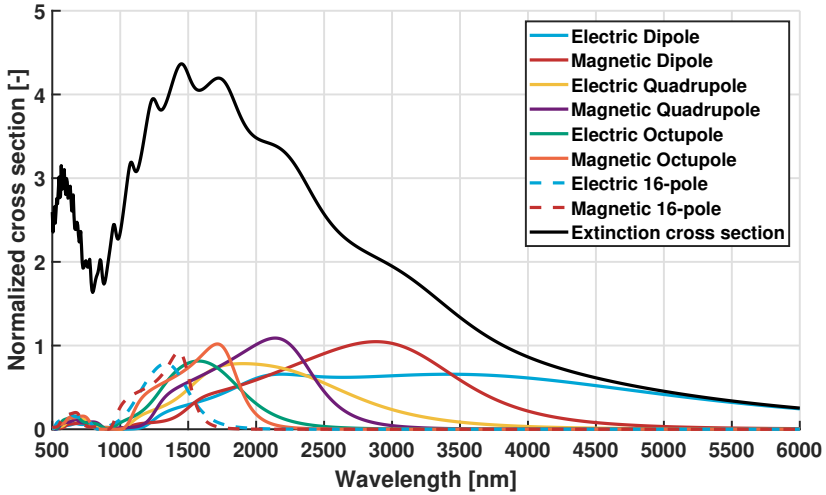


Figure 3.8: Plot of the multipole scattering cross section of the resonances being supported by a nanosphere with refractive index $n = 1.5$ and a diameter of $2 \mu\text{m}$. The cross sections are normalized with respect to the geometrical cross section. While higher order modes than 16-poles are supported for wavelengths shorter than 1500 nm , they are not shown in this graph.

3.1.3. EFFECT OF GEOMETRY

The geometry of a particle also has a substantial impact on its scatter properties. From the equations in the previous chapter describing the different multipoles (Equation 2.103, Equation 2.104, Equation 2.106, and Equation 2.105), this is expected. This is because different multipole contributions have different field and charge distributions. As a consequence, in what capacity these distributions can be supported depends directly on the geometry of the scatterer.

To investigate the effect of changing the geometry, we have to make sure that the total volume of the particle remains constant as we change the geometry. Otherwise, the we will also see the effects from the previous section on size change. Therefore, we will use a model in which we start with a sphere with radius $r = 80 \text{ nm}$, which we will transform into an ellipsoid by stretching it in the direction of the polarization of the incident light as illustrated in Figure 3.9.

When doing this, we will decrease the size of the ellipsoid in the other dimensions, such that the volume will be the same as that of the starting sphere. A refractive index of $n = 4$ is chosen for the particle such that many multipole contributions are visible. The result of the simulations are shown in Figure 3.10.

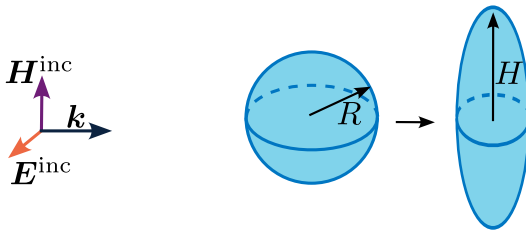


Figure 3.9: Schematic representation of the stretching of a nanosphere such that the volume of the nanoparticle stays constant. By analyzing the change in the resonances supported by the changing structure, we can isolate the effect of the geometry on the scattering behaviour.

To get more insight, this result can be split up into the contributions of the different multipole resonances, shown in [Figure 3.11](#). From [Figure 3.10](#) and [Figure 3.11](#) we can see that the behaviour of the resonances change significantly with changing geometry. The increase of broadening of the electric dipole resonance makes sense: the longer the spheroid, the more it approximates an antenna. Moreover, the electric dipole resonance shifts towards longer wavelengths as the antenna becomes longer. However, the other changing resonances cannot be explained with such ease.

For example, the magnetic dipole initially has a slight shift towards the longer wavelengths, then it quickly changes and shifts towards shorter wavelengths. In addition, a second resonance peak shows up which shifts towards the initial peak as the spheroid gets longer.

To further investigate the resonance behaviour, we can stretch the geometry in a different direction. We will see that this impacts the electric and magnetic resonances differently. Results from stretching the volume along the direction of the H-field are shown in [Figure 3.12](#). Again, we will split this result up into the contributions of the different multipole resonances in [Figure 3.13](#).

After stretching the sphere in the other direction, along the direction of the incident magnetic field ([Figure 3.12](#) and [Figure 3.13](#)), we see that the resonances behave completely different from before. This makes sense, we are not effectively creating an antenna anymore. The resonances all shift towards shorter wavelengths, because the width of the particle is becoming smaller. However, the second peak which appears for the magnetic dipole shifts in the opposite direction.

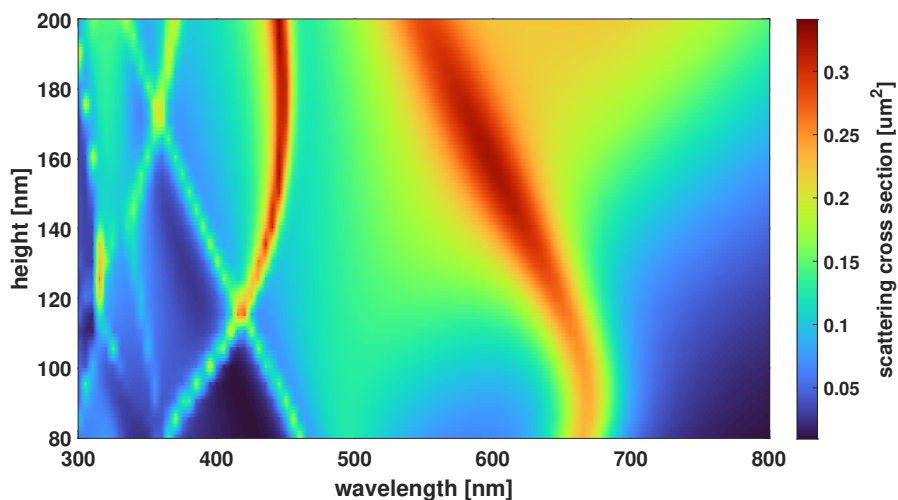


Figure 3.10: Scattering cross section as function of wavelength and height of a spheroid nanoparticle. The spheroid is elongated along the direction of the electric field.

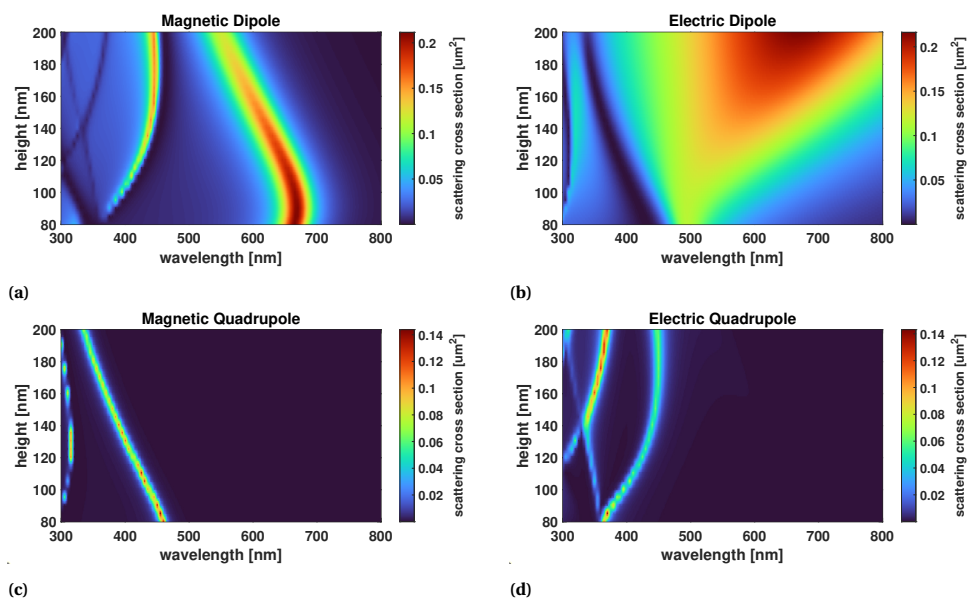


Figure 3.11: Cross sections of (a) the magnetic dipole, (b) the electric dipole, (c) the magnetic quadrupole, and (d) the electric quadrupole as a function of the height of a spheroid nanoparticle with $n = 4$. The spheroid is elongated along the direction of the electric field.

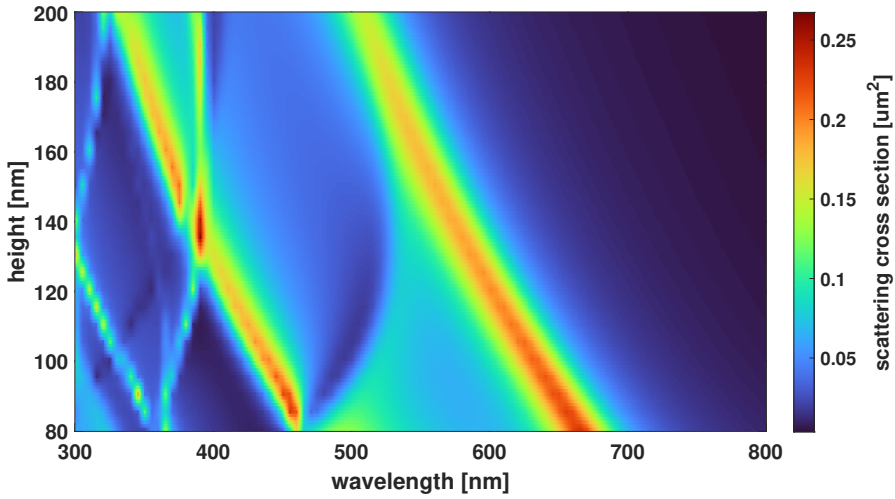


Figure 3.12: Scattering cross section as function of wavelength and height of a spheroid nanoparticle. Spheroid is elongated along the direction of the magnetic field.

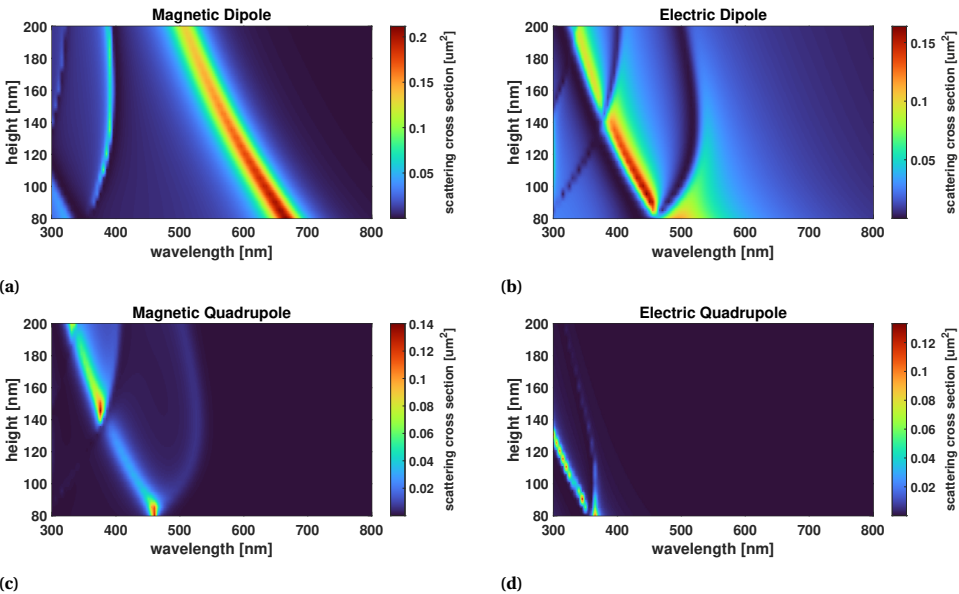


Figure 3.13: Cross sections of (a) the magnetic dipole, (b) the electric dipole, (c) the magnetic quadrupole, and (d) the electric quadrupole as a function of the height of a spheroid nanoparticle with $n = 4$. Spheroid is elongated along the direction of the magnetic field.

It is important to note that the crossing of multipole resonances can be observed due to the change in geometry. From [Section 2.6.3](#), we know this can be used to generate non-trivial far-field scatter patterns. However, from the figures above where the geometry is still rather simple, one can understand that the effect of geometry on these resonances is incredibly complex. Especially moving towards more complicated geometries, the resonances become even more unpredictable. The decomposition of these resonances does help with understanding the scatter behaviour. Furthermore, we see that the magnetic quadrupole splits up into two weaker resonance peaks.

3.2. SCATTERING PROPERTIES OF COMPOSITE NANOPARTICLES

From the previous section, we saw that no clear relation can be found between the shape and material of a nanoparticle and the multipole resonances (and therefore its scattering behaviour). It is possible to give a good estimation of whether a particle will have a high scattering cross section and whether the scattering is governed by resonances. However, it is not possible to predict the scatter pattern without performing numerical simulations.

Ways of manipulating specific resonances include the removal of material where the fields related to the resonances are strongest[49]. However, this can still have some effect on the other resonances which are present and results in geometries which are difficult to manufacture. More than often, a method of trial and error is employed.

As the space of possible geometries is enormous, getting a particle to scatter into a desired direction is a guessing game. This is one of the reasons why techniques involving artificial intelligence are used[50, 51]. However, these techniques still have large limitations as they are only able to predict the scattering by nanoparticles which have a geometry which is inside the solution space spanned by their training set. The size of such a set is still limited by numerical techniques and their associated time and computational resources.

An alternative is to explore possibilities outside of these resonances, using multiple materials as shown in [Figure 3.14](#) gives us a lot more design freedom. This freedom needs to be used in a smart way, otherwise the increased solution space would only be a detriment.

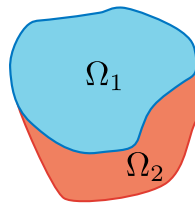


Figure 3.14: A composite nanoparticle comprised of two closed volumes Ω_1 and Ω_2 , each volume is composed of a different material.

First, we will consider the scattering by the two different materials independently. In order to do that, we will make use of the Lippmann-Schwinger equation to calculate the scattered field, which is given by [Equation 2.25](#). The relative permittivity with respect

to vacuum of the two materials and the medium is given by $\varepsilon_i(\mathbf{r})$, which is assumed to be isotropic. For convenience, we will use a spherical coordinate system with radial distance r , polar angle θ and azimuthal angle ϕ . The scattered field as function of the position vector \mathbf{r} can then be written as the sum of the two parts Ω_1 and Ω_2 :

$$\mathbf{E}^{\text{sc}}(\mathbf{r}) = k^2 \int_{\Omega_1} G^E(\mathbf{r}, \mathbf{r}_0) (\varepsilon_1 - \varepsilon_{\text{med}}) \mathbf{E}(\mathbf{r}_0) d^3 r_0 + k^2 \int_{\Omega_2} G^E(\mathbf{r}, \mathbf{r}_0) (\varepsilon_2 - \varepsilon_{\text{med}}) \mathbf{E}(\mathbf{r}_0) d^3 r_0 \quad (3.1)$$

where k is the wavenumber in the medium, ε_{med} the permittivity of the medium, \mathbf{E} the electric field vector, \mathbf{r}_0 the position vector over which is integrated. $G(\mathbf{r}, \mathbf{r}_0)$ is the scalar Green's function, since we will disregard polarization effects. The result of the above integrals are complex numbers, so the sum can result in interference. For large $|\mathbf{r}|$, this interference is dependent on the direction (θ, ϕ) , which results in directional scattering.

If the internal fields of the particle are known, this equation can be used to obtain the scattered field of each part of the particle. Later, we will use FEM to calculate these fields for particles that do not abide to the upcoming approximations.

For now, we will assume that the particle has a very low contrast with respect to the surrounding medium, such that

$$|\varepsilon_i - \varepsilon_{\text{med}}| kL \ll 1, \text{ where } i = 1, 2, \quad (3.2)$$

with L the characteristic length of the particle. In this case, we can use the first Born approximation (i.e. $\mathbf{E}(\mathbf{r}_0) = \mathbf{E}^{\text{inc}}(\mathbf{r}_0)$ inside the integral where \mathbf{E}^{inc} is the incident field), avoiding the need to know the exact internal field of the particle, so that

$$\mathbf{E}^{\text{sc}}(\mathbf{r}) = k^2 \int_{\Omega_1} G^E(\mathbf{r}, \mathbf{r}_0) (\varepsilon_{\Omega_1} - \varepsilon_{\text{med}}) \mathbf{E}^{\text{inc}}(\mathbf{r}_0) d^3 r_0 + k^2 \int_{\Omega_2} G^E(\mathbf{r}, \mathbf{r}_0) (\varepsilon_{\Omega_2} - \varepsilon_{\text{med}}) \mathbf{E}^{\text{inc}}(\mathbf{r}_0) d^3 r_0. \quad (3.3)$$

When considering a plane-wave travelling in the x -direction which is incident on the nanoparticle,

$$\mathbf{E}^{\text{inc}}(\mathbf{r}_0) = \mathbf{E}_0 e^{ikr_0 \sin \theta_0 \cos \phi_0}, \quad (3.4)$$

we can write:

$$\mathbf{E}^{\text{sc}}(\mathbf{r}) = k^2 \int_{\Omega_1} G^E(\mathbf{r}, \mathbf{r}_0) (\varepsilon_{\Omega_1} - \varepsilon_{\text{med}}) \mathbf{E}_0 e^{ikr_0 \sin \theta_0 \cos \phi_0} d^3 r_0 + k^2 \int_{\Omega_2} G^E(\mathbf{r}, \mathbf{r}_0) (\varepsilon_{\Omega_2} - \varepsilon_{\text{med}}) \mathbf{E}_0 e^{ikr_0 \sin \theta_0 \cos \phi_0} d^3 r_0. \quad (3.5)$$

Here, we used the spherical coordinates

$$r = \sqrt{x^2 + y^2 + z^2} \quad (3.6)$$

$$\theta = \arctan\left(\frac{\sqrt{x^2 + y^2}}{z}\right) \quad (3.7)$$

$$\phi = \arctan\left(\frac{y}{x}\right). \quad (3.8)$$

In 3D, the Green's function for the far-field is given by:

$$G^E(\mathbf{r}, \mathbf{r}_0) = \frac{e^{ik|\mathbf{r}-\mathbf{r}_0|}}{4\pi|\mathbf{r}-\mathbf{r}_0|} \approx \frac{e^{ik|\mathbf{r}-\mathbf{r}_0|}}{4\pi r} \quad (3.9)$$

with, in spherical coordinates,

$$|\mathbf{r}-\mathbf{r}_0| = \sqrt{r^2 + r_0^2 - 2rr_0[\cos(\phi-\phi_0)\sin\theta\sin\theta_0 + \cos\theta\cos\theta_0]}. \quad (3.10)$$

Using the Taylor expansion at $x=0$ for $\sqrt{1+x}$, we can rewrite this as

$$|\mathbf{r}-\mathbf{r}_0| \approx r \left\{ 1 - \frac{r_0}{r} [\cos(\phi-\phi_0)\sin\theta\sin\theta_0 + \cos\theta\cos\theta_0] + \mathcal{O}\left(\frac{r_0^2}{r^2}\right) \right\} \quad (3.11)$$

For now, let us only consider the forward direction: $\phi=0$, $\theta=\frac{\pi}{2}$. Then we can simplify Equation 3.5:

$$\mathbf{E}^{\text{sc}}(r, 0, \pi/2) = \mathbf{E}_0(\varepsilon_{\Omega_1} - \varepsilon_{\text{med}}) \frac{k^2 e^{ikr}}{4\pi r} \int_{\Omega_1} d^3 r_0 + \mathbf{E}_0(\varepsilon_{\Omega_2} - \varepsilon_{\text{med}}) \frac{k^2 e^{ikr}}{4\pi r} \int_{\Omega_2} d^3 r_0 \quad (3.12)$$

The resulting integrals are simply the volumes that the different parts of the nanoparticle occupy. Therefore, the phase difference between the contributions of the two regions - and therefore the scattered fields of the two parts of the nanoparticle - is only governed by the $(\varepsilon_i - \varepsilon_{\text{med}})$ terms. If we can achieve a phase difference of π , the scattered field of the two parts will destructively interfere, resulting in no scattering in the forward direction. This can be achieved by choosing the constituent materials so that the electric permittivity of the surrounding medium is in between that of the different constituents in the lossless case. Other phase differences can be achieved by using materials with complex permittivity.

3.2.1. CORESHELL NANOPARTICLES

To check whether this phase difference is as predicted by the first Born approximation, we will consider particles with increased contrast, for which Equation 3.2 does not hold. The easiest geometry where a particle is made up of two components with different materials are core-shell nanoparticles. The scattering by such a geometry can still be determined analytically using extended Mie theory[52].

To introduce a phase difference in the different materials, we will start with a core-shell nanoparticle which is completely dielectric, so the refractive indices of the materials are real numbers. The phase difference must then come from the choice of the refractive index of the surrounding medium as discussed in the previous section.

As a test case, a core-shell nanoparticle with inner radius of $R = 120$ nm and shell thickness $d = 30$ nm was used. We choose these dimensions so the volumes of the core and shell are approximately equal. For the permittivity of the surrounding medium, we choose $\epsilon_{\text{med}} = 2$ ($n_{\text{med}} = 1.42$). Taking $\epsilon_{\text{core}} = 1$ and $\epsilon_{\text{shell}} = 3$, the contrasts (given by $\epsilon_i - \epsilon_{\text{med}}$) are equal and opposite. Because the volumes of the core and shell are approximately equal, the magnitude of the scattered field will be comparable. From Equation 3.12, we see that this allows for the scattered field of each part to most effectively destructively interfere.

Next, we simulate an incident plane-wave with a wavelength (in vacuum) of $\lambda_0 = 500$ nm, which is polarized into the page as shown in Figure 3.15. From the calculated far field magnitude of the full particle shown in Figure 3.16a, we see this results in side-scattering and decreased forward scattering (for details on the simulation, see Appendix B).

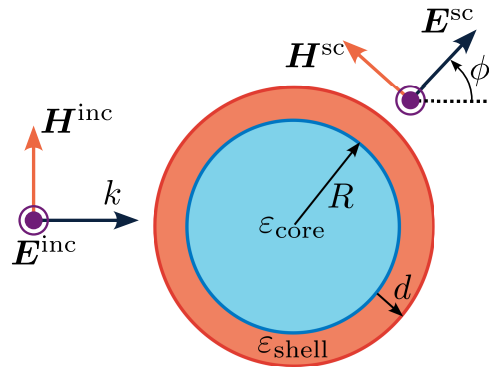


Figure 3.15: Plane-wave incident on a core-shell nanoparticle with core relative permittivity ϵ_{core} and shell relative permittivity ϵ_{shell} . The particle is in a homogeneous space with relative permittivity ϵ_{med} . The radius of the core is given by R and the thickness of the shell is given by d .

Since the local electric field is now known, the contributions of the core and shell can be evaluated separately using Equation 3.12. The resulting far field scattering pattern and phase difference of the scattered field between the constituents of the particle is shown in Figure 3.16. It can be seen that the scattering pattern of the core and shell parts resembles Mie scattering by low-index particles: most of the light is scattered in the forward direction and some of the light is scattered backwards. The phase difference explains the scattering pattern for the complete particle: the sideways-scattering originates from the destructive interference in the forward cone, where the phase difference is almost equal to π . In the sideward directions ($\phi = 100^\circ$ and $\phi = 260^\circ$), the phase difference is nearly zero, resulting in constructive interference.

Since the scattering pattern originates straight from the material properties and not from strong multipole resonances, it does not change significantly over the visible

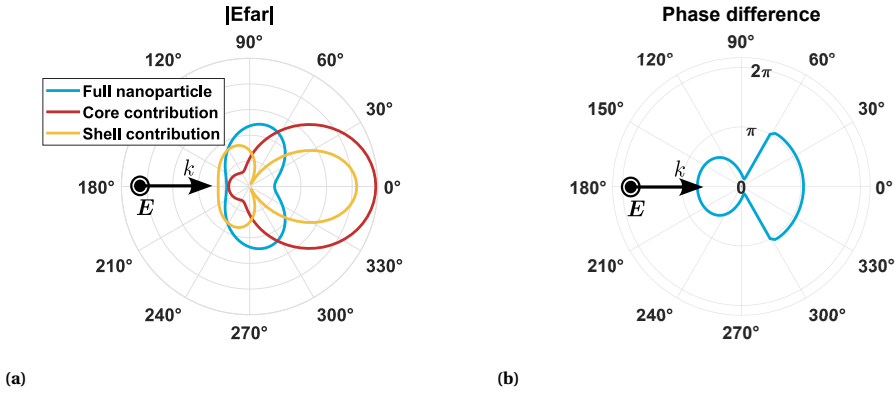


Figure 3.16: Polar plots of (a) the magnitude and (b) phase difference of the light with $\lambda_0 = 500$ nm scattered by a coreshell particle with $\epsilon_{\text{core}} = 1$, $\epsilon_{\text{shell}} = 3$, $R = 120$ nm, $d = 30$ nm inside a medium with $\epsilon_{\text{med}} = 2$.

spectrum when low dispersive materials are used. The scattering in the forward direction is suppressed over the entire spectrum, resulting in two lobes. On the other hand, the size of the particle compared to the wavelength is important for the scattering cross section. As a result, while the shape of the scattering pattern remains largely the same, the amount of light scattered by the particle decreases with increasing wavelength. To illustrate this, [Figure 3.17a](#) shows the scattering pattern and [Figure 3.17b](#) shows the scattering cross section and of the same particle for several wavelengths covering the range of the visible spectrum.

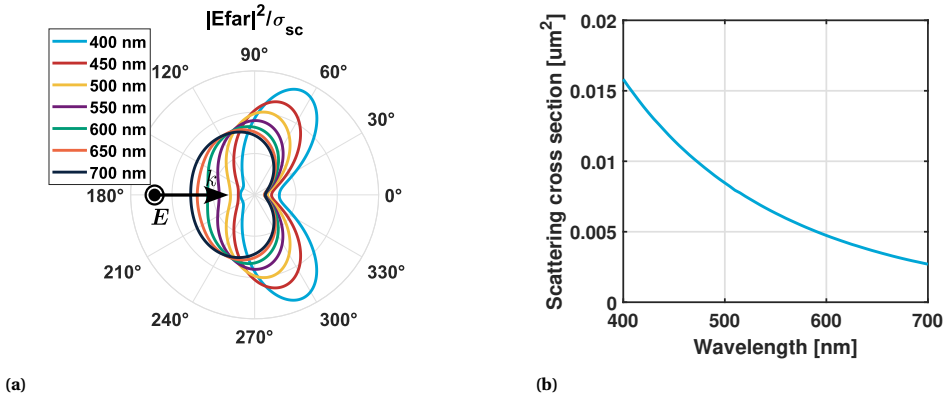


Figure 3.17: Plots of (a) the scattered far field intensity normalized by the scattering cross section and (b) scattering cross section over the visible spectrum of a core-shell nanoparticle in which a π phase difference is introduced between the scattered light of the core and the shell in the forward direction. The same particle is considered as in [Figure 3.16](#).

Introducing a material with complex permittivity makes it possible to achieve other phase differences. Now, we maintain the permittivity of the core ($\epsilon_{\text{core}} = 1$), and change

the permittivity of the shell to $\epsilon_{\text{shell}} = 2 + i$, such that $\epsilon_{\text{core}} - \epsilon_{\text{med}} = -1$, and $\epsilon_{\text{shell}} - \epsilon_{\text{med}} = i$. From Equation 3.12, we expect a phase difference of $3\pi/4$ in the forward direction. The results from the simulations, which are shown in Figure 3.18, confirm this.

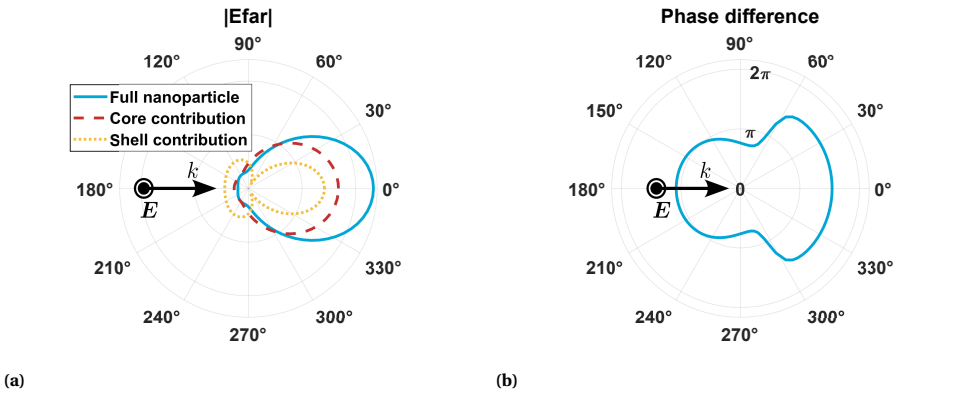


Figure 3.18: Polar plots of the (a) far field magnitude and (b) phase difference of the light with $\lambda_0 = 500$ nm scattered by a coreshell particle with $\epsilon_{\text{core}} = 1$, $\epsilon_{\text{shell}} = 2 + i$, $R = 120$ nm, $d = 30$ nm inside a medium with $\epsilon_{\text{med}} = 2$.

Coincidentally, we see that the scattered field in the backward direction is suppressed. The same decrease of scattering cross section with wavelength occurs as for the example with materials with only real permittivity for materials with complex permittivity as can be seen in Figure 3.19.

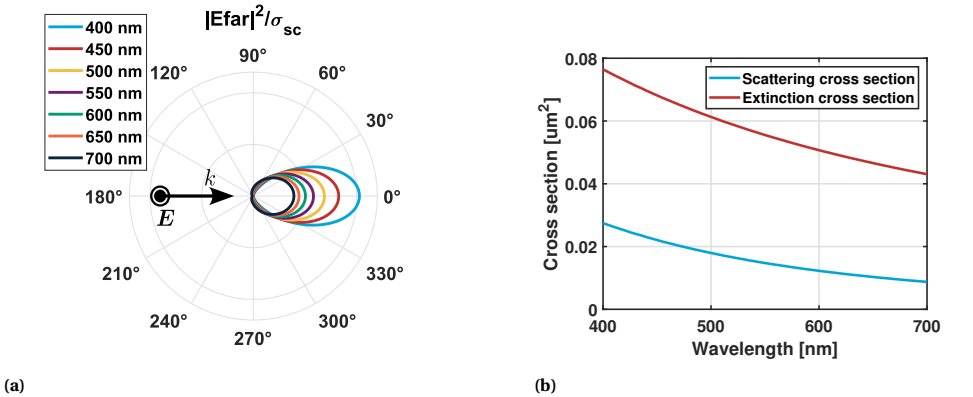


Figure 3.19: Polar plot of the (a) scattered far field intensity normalized by the scattering cross section and (b) cross sections over the visible spectrum of a core-shell nanoparticle in which a $\pi/2$ phase difference is introduced between the scattered light of the core and the shell in the forward direction. The same particle is considered as in Figure 3.18.

3.2.2. CORE-SEMISHELL NANOPARTICLES

It is important to note that the core-shell nanoparticles we considered in the previous section are completely symmetric. As a result, the related scatter patterns must also be completely symmetric with respect to the polarization direction of the incident beam. If we would like to achieve scattering into a single direction, we must break this symmetry. The easiest way to do this is to remove half of the shell, resulting in a core-semishell geometry as shown in [Figure 3.20](#).

3

In literature these are often called Janus particles: nanoparticles which have 2 surfaces with distinct physical properties (lending its name from the two faced Roman god Janus). In our case, the distinct physical properties would be a difference in refractive index on the opposite sides of the nanoparticle. These type of nanoparticles have already received a considerable amount of attention[53–58], because of their ease of fabrication and to study their geometry dependent resonances.

For the simplest case, in which the permittivity of both of the materials is real, either the phase difference must come from the electric field inside the particle, or the permittivity of the medium must be in between that of the two materials (see [Equation 3.1](#)). For the latter case, a π phase shift is realised.

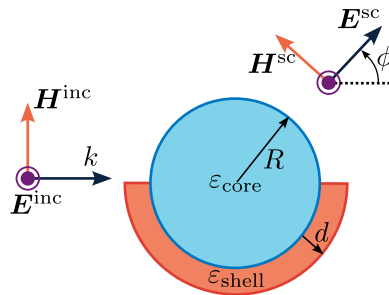


Figure 3.20: Plane-wave incident on a core-semishell nanoparticle (a type of Janus particle) with core relative permittivity ϵ_{core} and shell relative permittivity ϵ_{shell} . The particle is in a homogeneous space with relative permittivity ϵ_{med} . The radius of the core is given by R and the thickness of the shell is given by d .

We can investigate how the light is scattered when a plane-wave with a wavelength of $\lambda_0 = 500$ nm polarized into the page is incident from the side of the particle, with the semishell placed on the bottom as shown in [Figure 3.20](#). We keep the permittivity of the medium the same ($\epsilon_{\text{med}} = 2$). Then, we sweep over the permittivity of both the core and the semishell and plot the angle at which the magnitude of the scattered light is maximum.

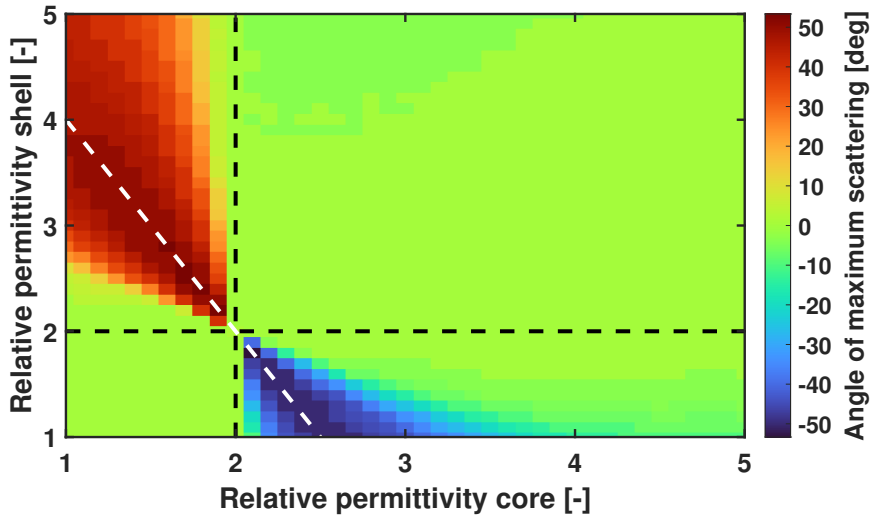


Figure 3.21: Angle ϕ of highest magnitude of scattered light with $\lambda_0 = 500$ nm vs core and shell relative permittivity. Core on the horizontal axis and shell on the vertical axis ranging from 1 to 5. The black dashed lines shows the permittivity of the medium ($\epsilon_{\text{med}} = 2$). Forward scattering is observed unless the permittivity of the medium is in between that of the core and shell. Along the white dashed line, the magnitude of the light scattered by the core and semishell is about equal.

From the results shown in [Figure 3.21](#), we can see that when the permittivity of both the core and the shell is either higher or lower than that of the medium, most light is scattered in the forward direction (0°). This is consistent with what we have seen before: the non-trivial scattering patterns are found when the permittivity of the core and shell is chosen such that the permittivity of the medium is in between that of the core and shell.

For more details, we can look at the actual scattering patterns that are simulated. In this case we take the permittivity of the core $\epsilon_{\text{core}} = 1.5$ and the permittivity of the shell $\epsilon_{\text{shell}} = 3.5$. As seen in [Figure 3.22](#), the scattering in the forward direction is almost completely suppressed and the light is scattered to the sides instead. Moreover, for the contributions of the core and shell to interfere properly, the magnitude of the scattered light by each part needs to be similar. This magnitude is proportional to the volume of a part and the contrast of its permittivity. This can also be seen in the graph, the largest angles are achieved when $(\epsilon_{\Omega_{1,2}} - \epsilon_{\text{med}})$ have opposite values (this corresponds with the top left and bottom right of the graphs in [Figure 3.21](#)).

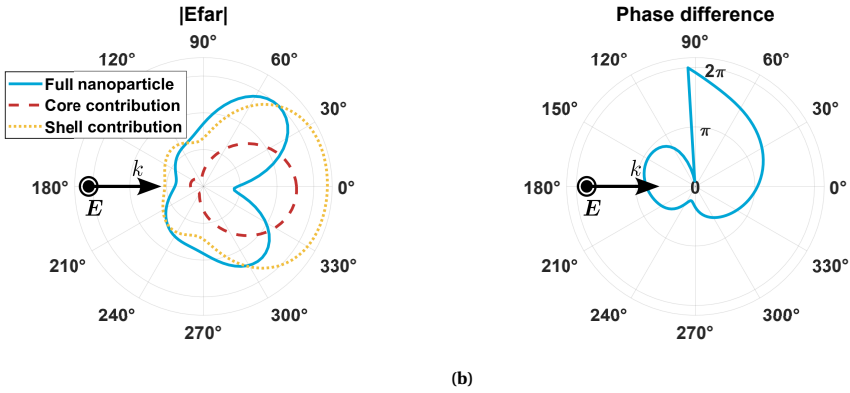


Figure 3.22: (a) Far field magnitude and (b) phase difference of light with $\lambda_0 = 500$ nm scattered by a core-shell particle with $\epsilon_{\text{core}} = 1.5$, $\epsilon_{\text{shell}} = 3.5$, $R = 120$ nm, $d = 30$ nm inside a medium with $\epsilon_{\text{med}} = 2$.

When using a material with absorption, instead of purely lossless materials, more possibilities arise since it is no longer necessary for the permittivity of the medium to be in between that of the core and the shell. The complex permittivity of a material is able to introduce interference effects between the each part of the nanoparticle. To show this, we again iterate over the permittivity of the core and the shell, but we add an imaginary part to the permittivity of the shell. Thus, the relative permittivity of the surrounding medium is kept at $\epsilon_{\text{med}} = 2$, but the imaginary part of the permittivity of the shell is changed to $\text{Im}\{\epsilon_{\text{shell}}\} = 1$.

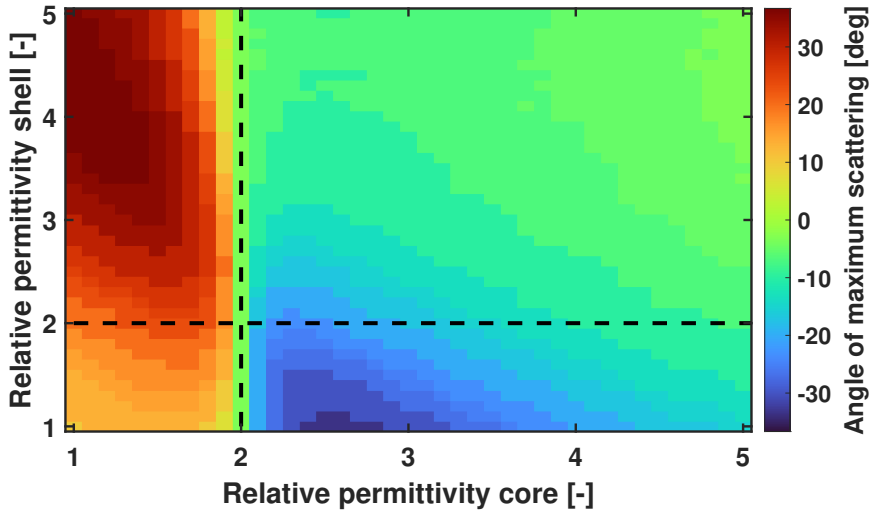


Figure 3.23: Angle ϕ of highest magnitude of scattered light with $\lambda_0 = 500$ nm vs core and shell relative permittivity. Core on the horizontal axis and shell on the vertical axis ranging from 1 to 5, the relative permittivity of the shell has a imaginary part of i .

From the results shown in Figure 3.23 we can see that - in contrast to the case with lossless components (Figure 3.21) - directional scattering is achieved for a much larger range of permittivities. Furthermore, when looking at the scattering pattern for a particle with $\epsilon_{\text{core}} = 2.5$ and $\epsilon_{\text{shell}} = 3 + i$ (Figure 3.24), we see that the light is scattered into a single direction. Of course, since the permittivity of the shell is complex, losses are associated with it because light is absorbed by the particle. This could be a disadvantage in certain applications.

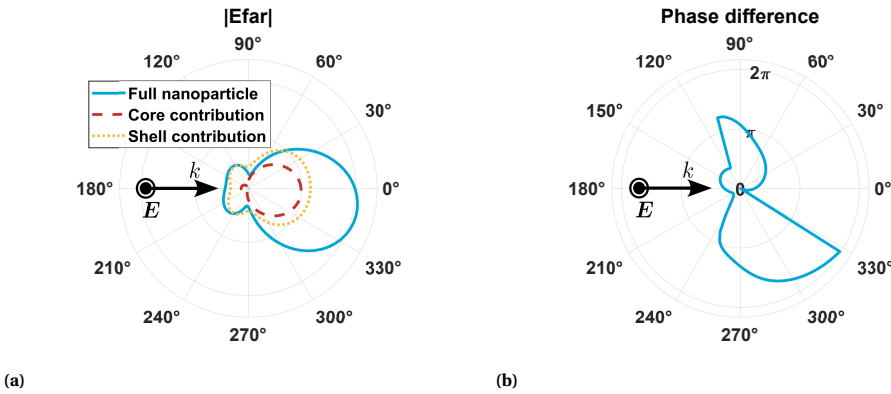


Figure 3.24: (a) Far field magnitude and (b) phase difference of light $\lambda_0 = 500$ nm scattered by a core-semishell particle with $\epsilon_{\text{core}} = 2.5$, $\epsilon_{\text{shell}} = 3 + i$, $R = 120$ nm, $d = 30$ nm inside a medium with $\epsilon_{\text{med}} = 2$.

The angle at which the light is scattered, can be controlled through the size of the composite nanoparticle. To show this, we start with the conditions where the scattering angle is greatest. For the lossless particle, this is where the contrast of the core and shell is balanced such that the magnitude of the scattered field of both are about equal. From here, we can change the size of the core and scale the semishell along with it, such that this balance is maintained. It follows that the height of the shell d is then a function of the core radius R :

$$d(R) = R(\sqrt[3]{2} - 1). \quad (3.13)$$

The calculated angle at which most light is scattered as a function of the size of the particle is shown in Figure 3.25.

From the graph, we can see that we can tune the direction the light is scattered into by changing the size of the nanoparticle. However, there are important changes with respect to the scattering pattern associated with that. For smaller core-semishell particles, the scattering pattern is broadened. For larger particles, the pattern becomes more directional. The same dependence can be seen in Figure 3.17. Furthermore, because of the semishell the asymmetry of the scattering with respect to the x -axis is increased.

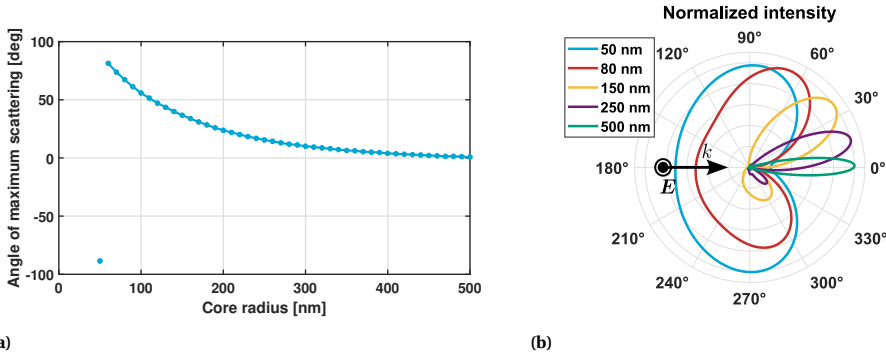


Figure 3.25: (a) Angle ϕ of highest magnitude of scattered light with $\lambda_0 = 500$ nm as a function of core radius for a core-semishell particle with $\epsilon_{\text{core}} = 1$, $\epsilon_{\text{shell}} = 4$ and $\epsilon_{\text{med}} = 2$, and (b) related scattering patterns normalized by the maximum intensity of all the scatter patterns.

This makes sense in the context of Mie scattering; small particles can only support a limited number of multipole resonances, resulting in a broad scattering pattern. For large particles, more multipole resonances contribute, resulting in more directionality. Specifically for a core radius of 50 nm, the scattering is almost symmetric. Moreover, the large particles barely scatter away from the forward direction.

Here we come to a point where the theory we use to understand the directional scattering breaks down. Up to a core radius of 150 nm, the scattering in the forwards direction is suppressed. After this point, the scattering is still directional, but light is scattered in the forward direction.

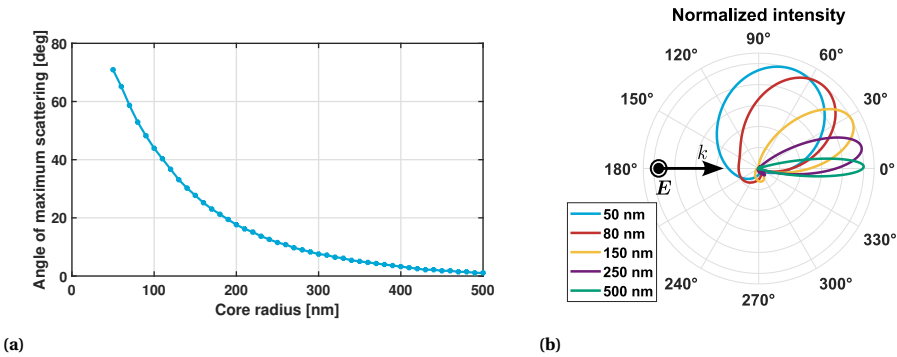


Figure 3.26: (a) Angle ϕ of highest magnitude of scattered light with $\lambda_0 = 500$ nm as a function of core radius for a core-semishell particle with $\epsilon_{\text{core}} = 1$, $\epsilon_{\text{shell}} = 4 + i$ and $\epsilon_{\text{med}} = 2$, and (b) related scattering patterns normalized by the maximum intensity of all the scatter patterns.

We can see that is also holds for cases where a complex permittivity is used. For this, we have taken permittivity combinations which can be found in Figure 3.23. The permittivity chosen were as follows: $\epsilon_{\text{core}} = 1$ and $\epsilon_{\text{shell}} = 4 + i$. The permittivity of the medium remained the same: $\epsilon_{\text{med}} = 2$. The results in Figure 3.26 show the same relation as before. However, due to the addition of absorption because of the complex

permittivity of the shell, the asymmetry is increased. This has the advantage that even for very small particles, directional scattering can be observed.

In reality, materials do not have a constant permittivity as function of wavelength, so for another test case we use the data of existing materials. We have chosen a core made of silica and a shell made of gold with the nanoparticle placed in air. The results are shown in Figure 3.27. The light is now scattered in the direction of the shell, because the permittivity of the medium is lower than that of the core.

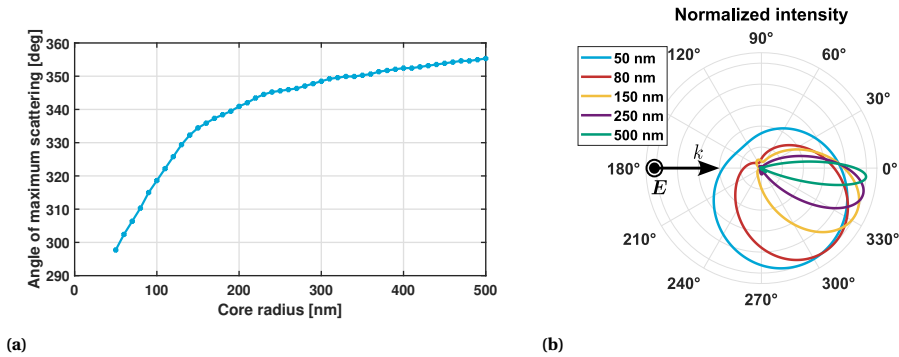


Figure 3.27: (a) Angle ϕ of highest magnitude of scattered light with $\lambda_0 = 500$ nm as a function of core radius for a core-semishell particle with a silica core and gold shell in air, and (b) related scattering patterns normalized by the maximum intensity of all the scatter patterns.

For such a nanoparticle, where the refractive index is not constant, we still observe that the directional scattering is maintained over the entire optical spectrum as is shown in Figure 3.28, where the scattering patterns for a silica / gold core-semishell particle are plotted for several wavelengths covering the visible spectrum.

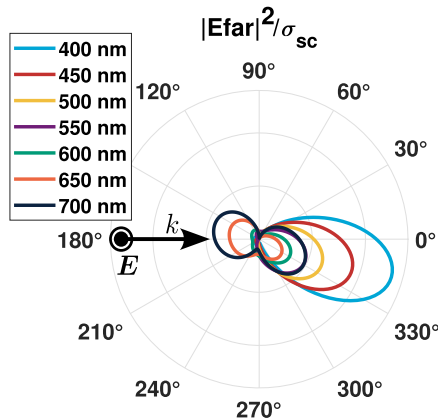


Figure 3.28: Plots of the scattered far field intensity normalized by the scattering cross section of a silica / gold core-semishell nanoparticle with a core radius of 150 nm and shell thickness of 39 nm for several wavelengths covering the visible spectrum.

3.2.3. OTHER GEOMETRIES

Since it is the volume that matters for the scatter pattern according to Equation 3.12, we can change the shape of the nanoparticle and still get similar results. As an example, we can simulate rectangular nanoparticles. In Figure 3.29, the scattering pattern by a spherical and equivalent rectangular composite SiO₂ / Au is shown.

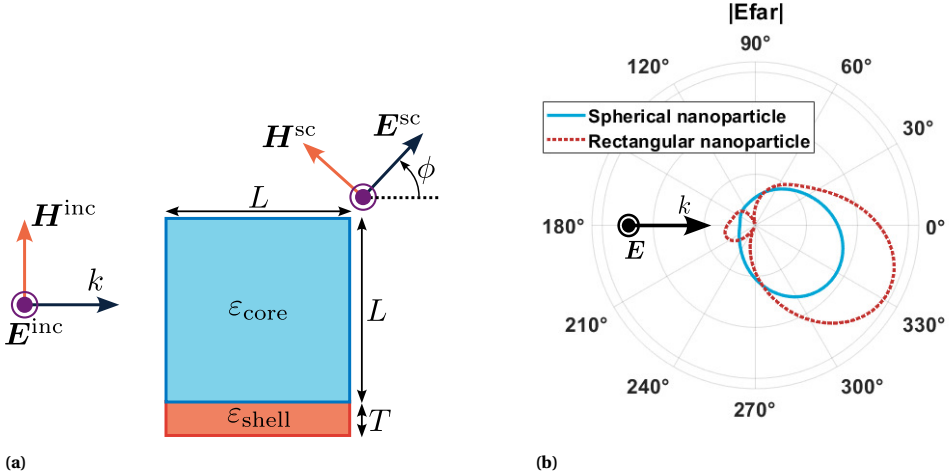


Figure 3.29: (a) Shape of the rectangular nanoparticle, which consist of a cube with sides of length L and an extra layer of material with thickness T . (b) Comparison of the electric far field of a spherical core-semishell SiO₂ / Au nanoparticle, with $R = 120$ nm, and $d = 30$ nm, and of a rectangular SiO₂ / Au nanoparticle, with $L = 240$ nm, and $T = 40$ nm. The wavelength of the incident field is $\lambda = 500$ nm.

From the figure it can be seen that the scattering pattern only changes slightly, the scattering direction is still maintained. As a result, the shape of the nanoparticles can be adopted to whatever fabrication method in most favourable for the application. Furthermore, fabrication tolerances will be large. As we have seen from Equation 3.12, the ratio between the amount of the two materials being used is important.

3.3. DIRECTIONAL SCATTERING AND GRATINGS

Because of the scattering characteristics of silica and gold nanoparticles, these could potentially be used for highly efficient transmission gratings. The idea is to construct a normal transmission grating and replace the grating elements by our directional scattering nanoparticles. By making sure the pitch of the grating is chosen so that the first diffraction order of the grating is at the same angle as the scattered field, most of the energy diffracted will end up in that diffraction order. This principle is illustrated in Figure 3.30.

Such a grating has been suggested before by Lütolf et al.[59], which indeed show increased efficiency in the first diffraction order. Unfortunately, no physical explanation was given towards the origin of the enhanced efficiency. Using our theory of scattering by composite nanoparticles, we are able to do that.

We start with a rectangular configuration. Because the grating is made of parallel

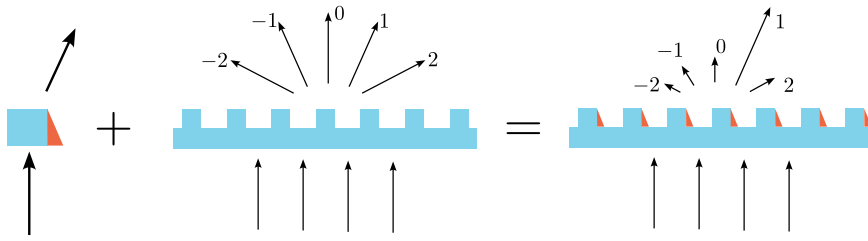


Figure 3.30: Schematic representation of the idea to combine single elements which scatter directionally, and putting them in a grating configuration. The resulting grating will have a high grating efficiency in the order corresponding to the scattering direction of the single element.

lines, we will simulate a two dimensional geometry. Let us first see what the scattering of such a nanoparticle (or nano-line) looks like when we add gold to the side following the methods developed in the previous section (Figure 3.31). The geometry of the nanoparticle is shown in Figure 3.31a. The reason for this geometry is due to the fabrication techniques that will be used, which will be discussed in Chapter 4.

In Figure 3.31b, we do not see the strong directionality as we saw in the previous section. The reason is the presence of the substrate, which significantly effect the response of the nanostructure to the incident light. We do see a preference towards the right side of the structure, again towards the same direction as the metal part of the scatterer, especially for the longer wavelengths. Because of the substrate there is also a strong forward scattering component. This forward scattering is also needed to be able to suppress the 0th transmission order.

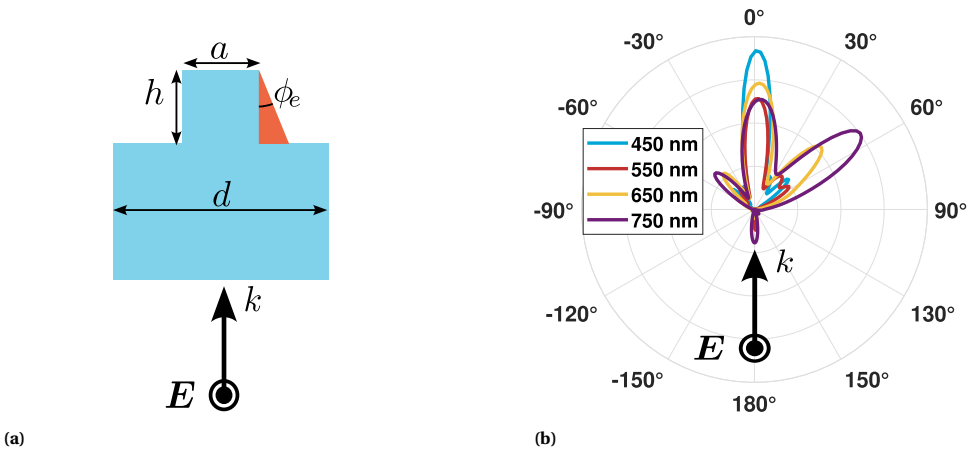


Figure 3.31: (a) Single grating element with pitch d , height h , and width a . The gold has been etched away at an angle of ϕ_e . A plane-wave with a polarization into the paper is incident from the bottom. (b) Simulated scattering (intensity divided by σ_{sc}^2) by a single grating element made of silica and gold with height $h = 520$ nm, width $a = 260$ nm, and $\phi_e = 5^\circ$ for various wavelengths.

Let us first consider the bare grating, i.e. no second material is added and the

scattering angles are solely determined by the geometry of the grating. The equation for determining the diffraction orders of a grating given by

$$d \sin \theta_m = m\lambda, \quad (3.14)$$

with d the grating pitch, θ_m the angle of the diffraction order m , and λ the wavelength of the incident light. Using this equation, we can determine the pitch of the grating, so the first order is diffracted at the same angle at which the nanoparticle scatters most of the light. In this case, the pitch would be 775 nm.

We can analytically determine the diffraction pattern and efficiency through the Fraunhofer approximation. The field at a far away point x_0, y_0, z_0 is then given by

$$U(x_0, y_0, z_0) = \frac{\exp(ikz_0) \exp\left[\frac{ik}{2z_0}(x_0^2 + y_0^2)\right]}{i\lambda z_0} \iint U(x, y, 0) \exp\left[\frac{-2\pi i}{\lambda z_0}(x_0x + y_0y)\right] dx dy \quad (3.15)$$

with U the field, and x and y the integration variables. The field inside the integral is determined by the grating structure.

To determine the response of a single period, we can simply integrate over the pitch d . Part of the grating will consist of a structure with refractive index n_{gr} , height h and width a , which will induce a phase delay due to the difference in refractive index of the surrounding medium n_{med} . We can now construct a transmission function $t(x)$:

$$t(x) = t_d(x) \left(e^{ikn_{gr}h} \text{rect}_{[0,a]} + e^{ikn_{med}h} \text{rect}_{[a,d]} \right). \quad (3.16)$$

This equation follows from the Born approximation in the case that the grating is thin. Here, $t_d(x)$ is the periodic function over the pitch of the grating.

To determine the performance of the grating, we can calculate the grating efficiency from the calculated intensity diffraction pattern using Equation 3.15. The grating efficiency G_m is defined by

$$G_m = \frac{P_m}{P_{inc}}, \quad (3.17)$$

where P_m is the power transmitted in the diffraction order m , and P_{inc} the power of the incident field.

First, we focus on limiting the 0th order transmission. We can do that by changing the height such that the light passing through the grating elements has a $\pi/2$ phase difference with respect to the light passing between the elements. The height is then determined by

$$h = \frac{\lambda}{2(n_{gr} - n_{med})}. \quad (3.18)$$

Taking the width to be half the pitch, and using Equation 3.18 to determine the height, we would expect zero transmission in the 0th order for the design wavelength of 550 nm. Calculating the diffraction efficiency for the 1st and 0th order for $h = 520$ nm, we get the graph shown in Figure 3.32.

Using COMSOL, we can simulate a grating using periodic boundary conditions, here also the reflection and geometrical effects of the grating are taken into account. For more

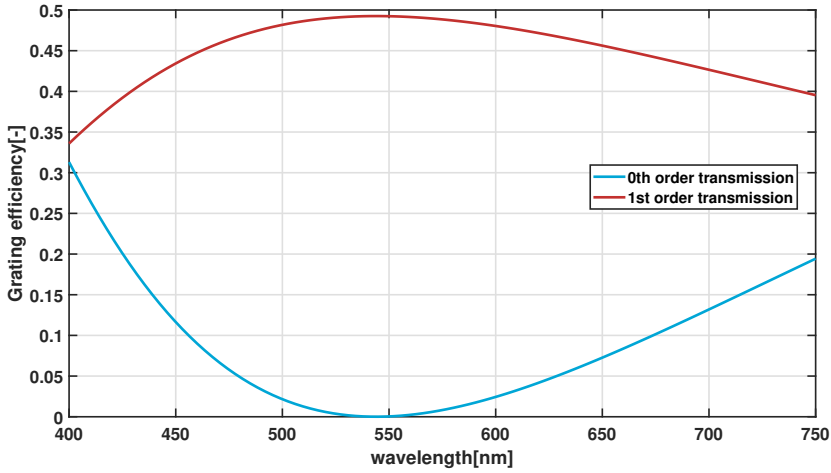


Figure 3.32: Graph of the grating efficiency of a rectangular grating made of glass with $d = 775$ nm, $a = 378$ nm, and $h = 520$ nm over the visible spectrum. The efficiency was calculated according to the Fraunhofer approximation. The incident field is at normal incidence and polarized along the grating lines.

information on the simulations, see [Appendix B](#). The results from the simulations in terms of grating efficiency are shown in [Figure 3.33](#).

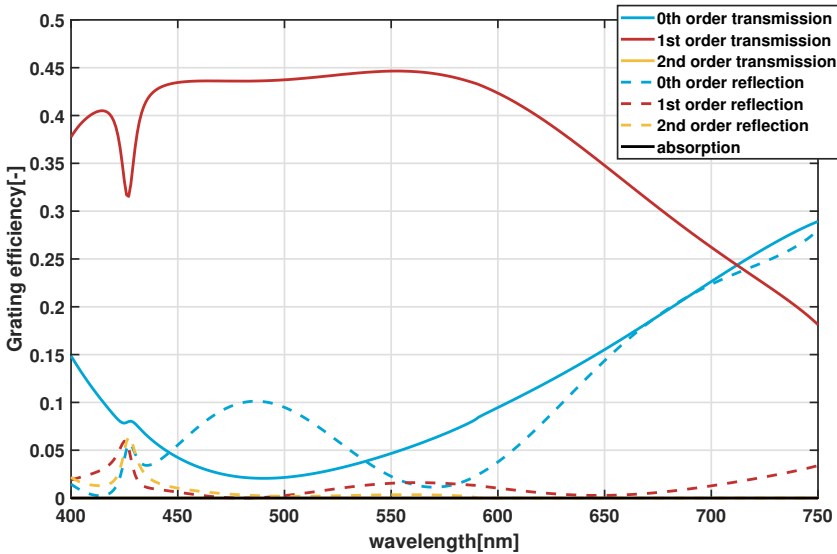


Figure 3.33: Graph of the grating efficiency of a rectangular grating made of glass with $d = 775$ nm, $a = 260$ nm, and $h = 520$ nm over the visible spectrum. The efficiency was calculated using COMSOL. The field is at normal incidence and polarized along the grating lines.

There are some differences with the efficiency obtained through the Fraunhofer approximation and the COMSOL simulations. This is because in the Fraunhofer approximation, only energy being transmitted is taken into account. Of course, we also expect losses in efficiency due to reflection. Moreover, the transmission function used to define the field at in plane given by Equation 3.16 is no longer valid when the pitch is comparable to the wavelength of the incident light. Finally, the 2D geometry of the grating is not taken into account in the Fraunhofer approximation.

An example of this discrepancy is the resonance effect that can be observed around 425 nm in Figure 3.33. This is due to light coupling into the grating itself, which is clear from the near field shown in Figure 3.34; the electric field is confined to the grating. The result is a dip in the 1st order grating efficiency.

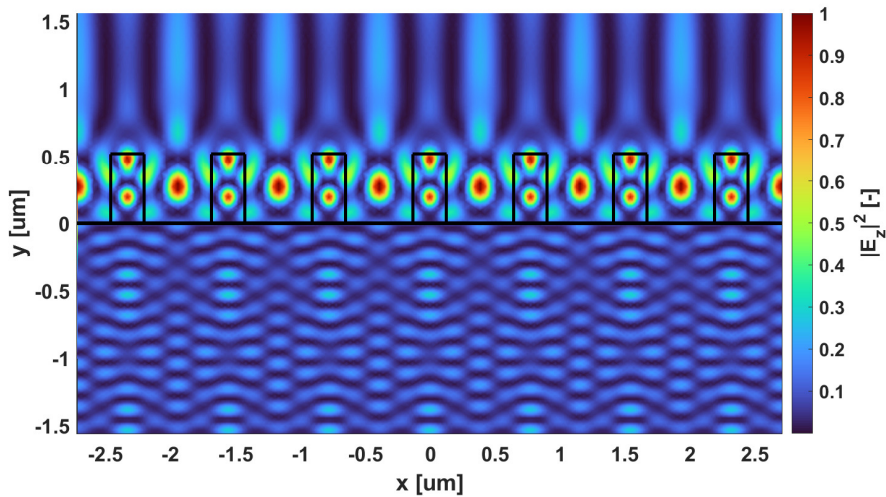


Figure 3.34: Near field as the normalized square of the magnitude of the electric field over 7 periods of the grating at $\lambda = 428$ nm. It can be seen that the field is concentrated inside the grating structure. The incident field is at normal incidence from the bottom and polarized along the grating lines.

3.3.1. METAL COMPOSITE ELEMENTS

When introducing the composite nanoparticles as the grating elements by adding gold, the scattering efficiency of the first order increases significantly, as can be seen from [Figure 3.35](#). This shows that the theory of directional scattering composite nanoparticles presented in [Section 3.2](#) can be applied to gratings as well. Because the symmetry of the grating is broken, the negative and positive diffraction orders also separate. The dip due to coupling can still be seen at around 445 nm, it is shifted and reduced due to the addition of the gold to the grating, changing the effective refractive index.

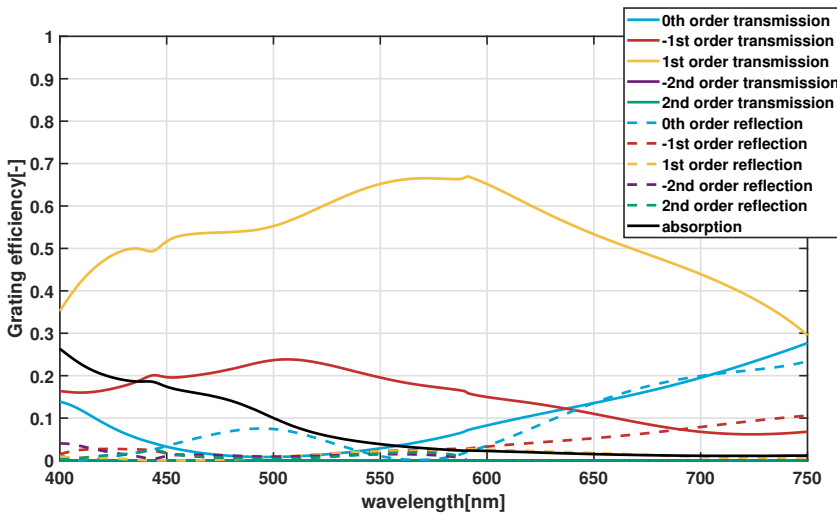


Figure 3.35: Graph of the grating efficiency of a rectangular grating made of glass and gold with $d = 775$ nm, $a = 260$ nm, and $h = 520$ nm over the visible spectrum. The efficiency was calculated using COMSOL. The incident field is at normal incidence and polarized along the grating lines.

The efficiency can be optimized further by breaking the symmetry in a different way; by changing the angle of incidence of the incident light. First, we will demonstrate its effect by changing the incident angle for the bare grating. The grating efficiency for an incident angle of 12° is shown in [Figure 3.36](#). Comparing this to normal incidence ([Figure 3.33](#)), we see that the efficiency has significantly increased. However, the downside is that the wavelength at which the light is coupled into the wavelength has shifted towards the center of the spectrum. Despite this, the efficiency at that point is only slightly lowered compared to the normal incidence.

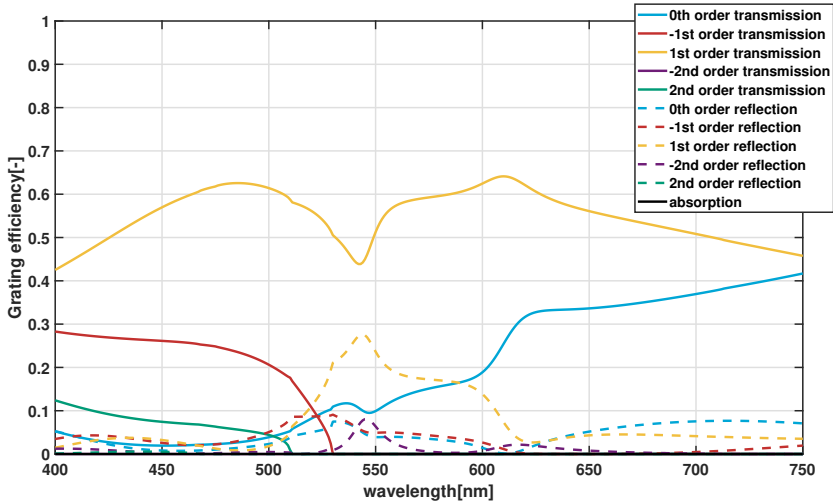


Figure 3.36: Graph of the grating efficiency of a rectangular grating made of glass with $d = 775$ nm, $a = 260$ nm, and $h = 520$ nm over the visible spectrum. The efficiency was calculated using COMSOL. The field is at a 12° incident angle and polarized along the grating lines.

We can do the same for the composite grating with gold, where the optimal² incident angle is at 15° . The results of which are shown in Figure 3.37. Now we are able to reach an efficiency of more than 60% for almost the entire visible spectrum. This is limited mostly by the 0th order transmission for the longer wavelengths and the absorption by the gold for the shorter wavelengths. Compared to what can be done with a normal grating, this is quite a large performance increase.

The reason we have been using gold so far, is because we have been using it for the composite nanoparticles. Of course, we could use a different metal with less absorption, especially for the shorter wavelength. Potential candidates for this are silver, aluminum and titanium. From simulations, we found that the material for which we were able to reach the best performance was silver. Figure 3.38 shows the results for a silver composite grating for an incident angle of 15° . Now, we have an efficiency of more than 65% over almost the entire visible spectrum. On the downside, the dip in the efficiency due to coupling into the grating is increased due to an increase in absorption.

²The optimum is defined as the highest efficiency over the entire shown spectrum

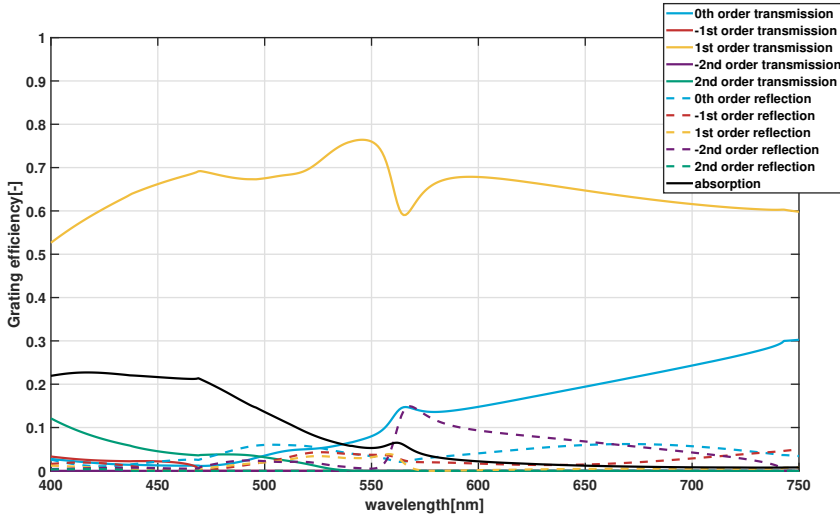


Figure 3.37: Graph of the grating efficiency of a rectangular grating made of glass and gold with $d = 775$ nm, $a = 260$ nm, and $h = 520$ nm over the visible spectrum. The efficiency was calculated using COMSOL. The field is at a 15° incident angle and polarized along the grating lines.

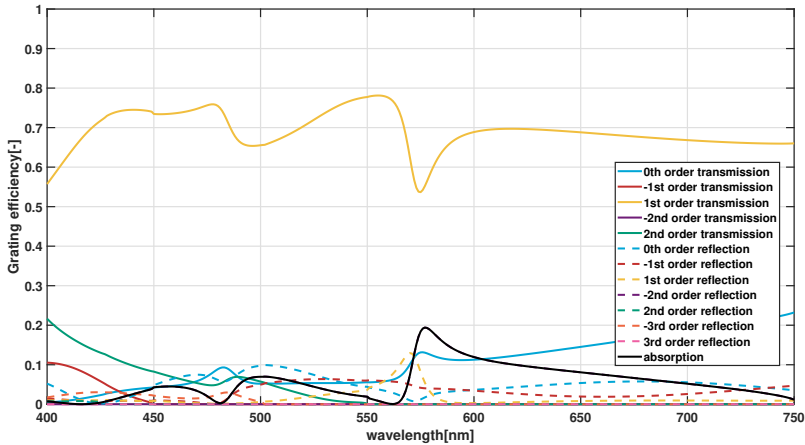


Figure 3.38: Graph of the grating efficiency of a rectangular grating made of glass and silver with $d = 775$ nm, $a = 260$ nm, and $h = 520$ nm over the visible spectrum. The efficiency was calculated using COMSOL. The field is at a 15° incident angle and polarized along the grating lines.

For such a simple addition to a standard grating structure, a large increase in the efficiency can be achieved. Furthermore, this addition can potentially be easily integrated in the production process. The addition of the metal can be realized with a simple sputtering and etching step, which can be used at a large scale.

3.3.2. EMBEDDED COMPOSITE GRATINGS

The next logical question to ask is whether increasing the efficiency of a grating as is shown in the previous section could be possible when using materials with no optical absorption. As we have shown in Section 3.2, this can be done by embedding the nanoparticles inside of a medium, while making sure that the refractive index of the medium is in between that of the two materials used for the composite nanoparticle. In that case, directional scattering can be achieved without the use of lossy materials. Something similar can be done for a grating, by embedding the grating elements inside a medium as shown in Figure 3.39.

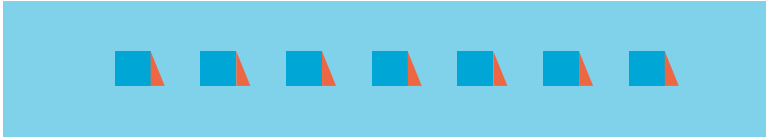


Figure 3.39: Schematic representation of a grating which consist of composite grating lines embedded into a medium.

The big advantage of embedding the grating inside of a medium, is that the substrate can be matched to the medium. As a result, the effect of the substrate is removed. Then, choosing the size of the grating elements carefully by taking into account the relation between size and scattering angle, the elements can be made to not have any forward scattering.

At first look, it seems like this opens up the way for transmission gratings with nearly unity efficiency for a single diffraction order. However, the chosen medium will limit the contrast that can be achieved (the largest contrast possible would be $n_{\text{med}} - 1$). Consequently, the scattering cross section is also limited. If the scattering cross section is too small, we would still have a significant 0th order contribution due to light that has simply not interacted with the grating.

Furthermore, when embedding the grating elements inside of a medium, we need to account for total internal reflection. By increasing the pitch of the grating, we can make sure that the first diffracted order is coupled out. This further decreases the effective scattering cross section. Also, the light can couple into the higher diffraction orders, which cannot couple out as the diffraction angles get too large.

Summarizing, due to the limitation of refractive indices that can be chosen because of the medium, there are several competing effects:

1. to have a large enough scattering cross section, the grating elements must be large and the contrast has to be as large as possible.
2. to reduce the 0th order transmission, the grating pitch has to be small.
3. to enhance a diffraction order, the grating element must be relatively small.

As an example we will show a diffraction grating made of air and aluminumoxide (Al_2O_3) inside PDMS. PDMS has a refractive index of about 1.4, and Al_2O_3 has a

refractive index of 1.8. As a result, the relative volume of each of the materials should be approximately the same.

We will start the design like before; first, creating a normal rectangular grating made of only air inside PDMS. The grating is designed so that the highest efficiency can be attained for a wavelength of 550 nm (inside air). The pitch is chosen such that we will achieve the same angular resolution as before. The results are shown in [Figure 3.40](#).

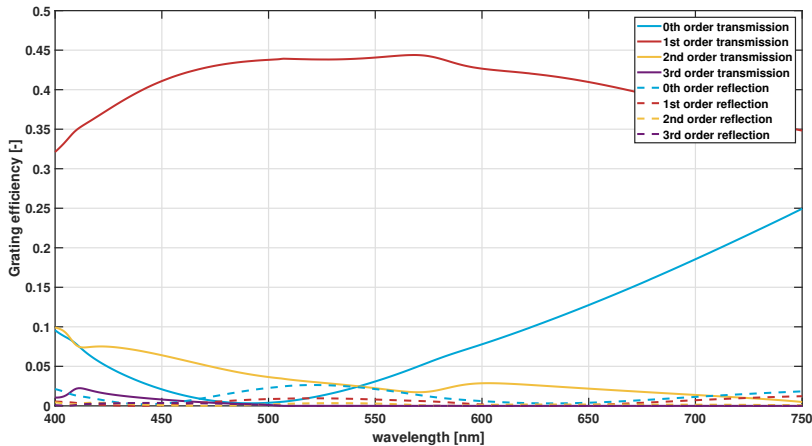


Figure 3.40: Graph of the grating efficiency of a rectangular grating made of air inside PDMS with $d = 1085$ nm, $a = 543$ nm, and $h = 650$ nm over the visible spectrum. The field is at normal incidence and polarized along the grating lines.

Next, the Al_2O_3 is added. The highest efficiency could be reached for a thickness of 50 nm, the results are shown in [Figure 3.41](#). Compared to the results where a metal was added, the achieved efficiency of the -1^{st} transmission order is quite disappointing. We can also see the cause of this: the 1^{st} transmission order is still relatively high. This is due to the large size of the elements, which results in limited asymmetry at the angles of the 1^{st} and -1^{st} diffraction orders. The elements must be quite large as the 0th order diffraction can otherwise not be suppressed sufficiently.

A possibility to counteract this is to make a bi-layer of smaller grating elements, which combined can still suppress the 0^{th} order. However, this would make the production process much more complicated. We have not investigated this possibility as it is out of scope of this thesis.

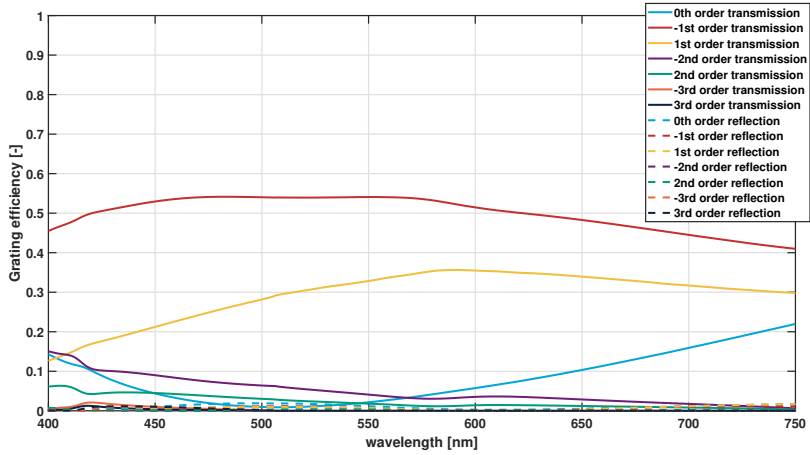


Figure 3.41: Graph of the grating efficiency of a rectangular grating made of air and Al₂O₃ inside PDMS with $d = 1085$ nm, $a = 680$ nm, and $h = 650$ nm over the visible spectrum. The field is at normal incidence and polarized along the grating lines.

3.4. SUMMARY AND OUTLOOK

In this chapter, we have shown the scattering behaviour of particles as a function of size, material and geometry. From this, we have seen that the scattering behaviour is not easily understood. As a result, in most studies trial and error methods are used to design scatterers. We proposed a new method, which makes it possible to easily design composite scatterers that scatter into a certain direction.

By eliminating the dependence on resonances, the directionality of the scattering becomes less reliant on the incident light's wavelength and instead depends on the material properties. This characteristic suggests that our proposed method holds the potential to achieve achromatic metasurfaces, offering enhanced performance over a broad range of wavelengths. Furthermore, the geometry of the nanostructures can be adapted to the fabrication capabilities and the tolerances of making this structure are relatively large.

Using the developed methods, we have shown designs for composite nanoparticle which scatter in a non-trivial direction. Furthermore, we have shown how this method can be used to design a highly efficient transmission grating usable for the entire visible spectrum.

We have also fabricated the composite nanoparticles and gratings, in order to measure them and experimentally verify the simulation results. The details on the fabrication of the nanoparticles and gratings will be discussed in [Chapter 4](#). The measurements can be found in [Chapter 5](#).

4

FABRICATION OF COMPOSITE NANOSTRUCTURES

“

Part of the art and skill of the engineer and of the experimental physicist is to create conditions in which certain events are sure to occur.

Eugene Wigner[9]”

IN [Chapter 3](#), we have seen how a nanoparticle can be designed such that it scatters light into a desired direction. Using this, we have also seen that we can create highly efficient diffraction gratings. To make measurements of the scattering and validate our theory, these particles and gratings would first need to be produced. This is no trivial task, since combining different materials at the nanoscale is usually challenging.

Methods to create composite nanoparticle have been explored by researchers, finding many applications in the field of biology (for drug delivery, imaging and more)[60] and chemistry (as catalysts)[61]. Usually, such particles are produced chemically, which has the benefit of being easily scalable. These are often in the form of core-shell particles, although other geometries are also available. The creation of anisotropic particles would generally require an extra step.

Other methods include the use of lithography that allows for precise control over the position and geometry of the fabricated particles. However, adding the second material to create a composite nanostructure introduces some additional challenges.

In this chapter we will explore different methods for the fabrication of composite nanoparticles. Initially, we will use deposited nanospheres as the start of the nanoparticle in [Section 4.1](#). From there, we will show several ways of obtaining composite nanoparticles. For each of the proposed methods, we will discuss the advantages and disadvantages.

For the fabrication of gratings that were discussed in [Section 3.3](#), e-beam lithography is used. The process discussed in [Section 4.2](#). The fabrication results presented in this chapter will form the basis of the samples used in the measurements that are presented in [Chapter 5](#).

4.1. COLLOID NANOPARTICLES

The easiest and cheapest option available for acquiring nanoparticles is in the form of colloids i.e. particles that are suspended in a liquid. These colloids are produced chemically, making the production process easily scalable. To stop the aggregation of the nanoparticles inside the liquid due to Van Der Waals forces, the surface of the nanoparticles is often modified.

Generally, molecules with a static charge are attached to the surface of the nanoparticles so that the particles repel each other in the liquid they are suspended in. A schematic representation is shown in [Figure 4.1](#). The size of the nanoparticles can be controlled by changing variables of the production process, or the nanoparticles of different sizes can be filtered afterwards by the use of centrifugation.

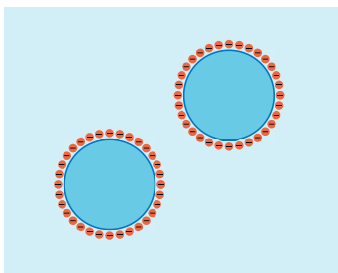


Figure 4.1: Spherical nanoparticles suspended in a liquid as part of a colloid. The particles repel each other through the surface charge they have which prevents them from agglomerating because of the Van Der Waals Forces.

The nanoparticles can be deposited on a surface by letting the liquid solution evaporate. However, getting a fairly homogeneous distribution of nanoparticle is difficult due to the surface tension of the solution that the nanoparticle are in. While the solution is evaporating, the solution will form droplets. As more of the solution evaporates, the surface tension of the liquid will pull the droplet together, resulting in particles present in the droplet to aggregate on the surface.

Functionalizing the surface of the substrate can help in this process. A paper by Malynych et. al.[62] shows this can be done by using poly(vinyl pyridine) (PVP). Both metallic and dielectric nanoparticles can be attracted to the PVP molecule, immobilizing them on the surface on which the PVP is deposited. By using adsorption to place the PVP on the wafer surface, an incredibly thin layer will be left behind, which will not affect the optical properties of the sample.

Then, instead of letting the solution evaporate, we can wait a certain amount of time for the nanoparticles to attach themselves to the surface. Afterwards, the surface can be rinsed with distilled water. Most nanoparticles are attached firmly enough to the

surface to remain there, while no significant amount of aggregation occurs due to the evaporating water pulling the nanoparticles together.

Aggregation can further be reduced by reducing the density of nanoparticle in the solution, simply because the average distance between the individual nanoparticles is increased. However, this does show the main disadvantage of using colloid nanoparticles: there is a trade-off between the amount of particles on the sample and the amount of aggregation. If the amount of nanoparticles on the surface is too small, combined with a small scattering cross section, there will not be a significant macroscopic effect. Increasing the amount of particles could lead to aggregation and the scattering characteristics may be affected.

For this reason, we will use the colloid nanoparticles to look at the microscopic scattering behaviour. In this section, we will present two fabrication methods which lead to composite nanoparticles with different geometries.

4.1.1. PRODUCTION OF CORE-SEMISHELL PARTICLES

For the first production method, we will produce core-semishell nanoparticles. These have been featured in many scientific papers already [55, 57, 63–67], because of their ease of manufacturing. In most papers, the scattering by the shells was studied without taking the core into account. These structures are generally called nanocups. However, as we have seen in [Chapter 3](#), the core can play an important role in the scattering behaviour.

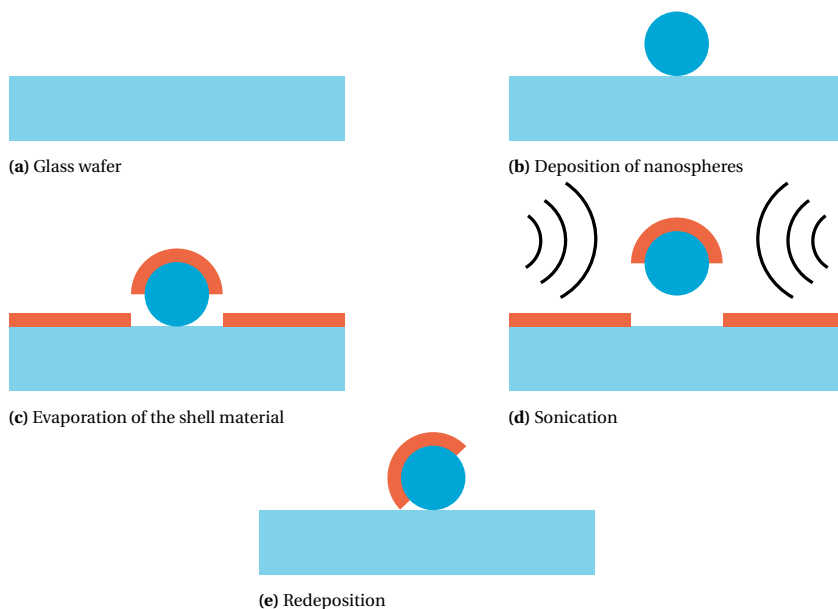


Figure 4.2: Schematic representation of the fabrication process of composite core-semishell nanoparticles. We start with a glass wafer (a), onto which silica nanospheres are deposited (b). Next, the shell material is evaporated on top (c). Then, the sample is sonicated and the core-semishell nanoparticles are released from the surface and re-suspended (d). Finally, the nanoparticles are redeposited (e).

The method of fabrication is fairly simple; a schematic representation is shown in [Figure 4.2](#). We start by depositing nanospheres onto a glass wafer. Next, we use evaporation to cover the top of the nanospheres by the shell material. Because of the evaporation, the surface of the glass wafer will also be covered by the shell material. This would also scatter the incident light during experiments, so we need to release the produced core-semishell nanoparticles from the wafer. This is done by sonicating the samples in water. During this process, the nanoparticles are released from the surface. With this we create a new colloidal solution of core-semishell nanoparticles, which can then be deposited on a new wafer.

The downside is that we do not have control over the orientation of the semishell. However, we observed that an orientation where the edge between the core and the semishell is on the glass wafer is somehow favoured (for silica/gold core-semishell nanoparticles). Still, the majority of the particles have an incorrect orientation, but enough particles have the right orientation so effective measurements can be performed without having to search for too long. Additionally, from the measurements we cannot be sure that the particles were indeed in the expected orientation.

For the production of silica/gold core-semishell nanoparticles, 300 nm colloid silica (SiO_2) 50 mg/mL nanoparticles solution was diluted to 70 $\mu\text{g}/\text{mL}$ by pipetting 20.0 μL of the colloid nanoparticle solution into 15.0 mL of distilled water. At this concentration, the distance between the nanoparticles which remain on the substrate is large enough to be in the single scattering regime.

Borosilicate glass wafers (UQG Optics 25 mm diameter Schott D263T 0.7 mm thick wafer) were cleaned with ethanol ($\geq 99.5\%$ Sigma-Aldrich). The ethanol on the wafer was then removed with a nitrogen gun. Afterwards, any remaining organic material was removed from the surface of the glass wafer by the means of plasma cleaning (Tepla 100, 300 W at 1.0 mBar).

After the cleaning steps, the wafers were put into a solution of 1-m% PVP (Sigma-Aldrich Poly(4-vinylpyridine) Mw 160000) in ethanol for 1 hour. This allows for the PVP to be adsorbed onto the surface of the glass wafer, creating a single-molecule thick layer improving the adhesion of the nanoparticles to the substrate.

Afterwards, the glass wafers were rinsed using ethanol in order to remove any PVP which has not already adsorbed onto the surface. The ethanol was again removed from the surface with a nitrogen gun.

At this point, the substrates are ready for the nanoparticles to be deposited. A drop of approximately 0.5 mL of the 70 $\mu\text{g}/\text{mL}$ 300 nm colloid SiO_2 solution is deposited onto a glass wafer. The nanoparticle solution remains on the substrate for about 30 min in order for enough nanoparticles to adhere to the surface. Then, the solution was rinsed of the wafer with distilled water. Any water that was left on the surface was then blown off using a nitrogen gun.

Upon inspection with an optical microscope, the nanoparticles can be seen on the surface of the glass wafer as shown in [Figure 4.3](#). The bright dots are the individual nanoparticles, some cases where two or more particles are aggregated together can also be observed. In [Figure 4.3b](#), a bright patch where a large amount of particle are aggregated together can be seen

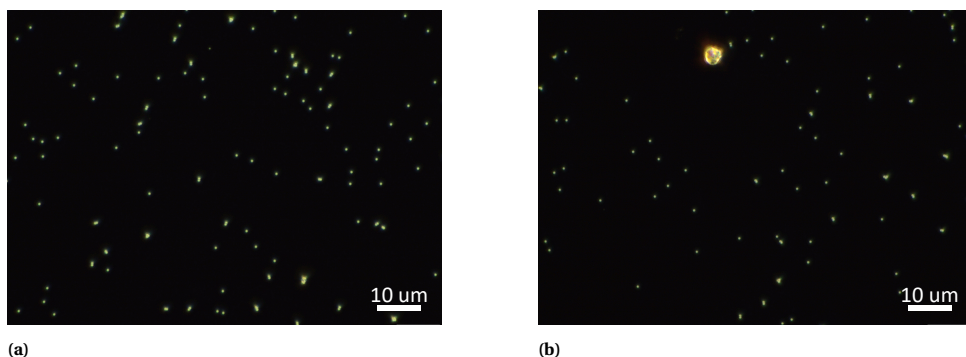


Figure 4.3: Micrographs of deposited 300 nm SiO₂ nanoparticles on a glass wafer. Some aggregated nanoparticles can be seen, in particular in the right figure.

Other material choices are, of course, also possible; in our experiments we have also used polystyrene cores (as in [Figure 4.5b](#)) and silver or titania shells. The production of silica/gold particles was the easiest and satisfy the conditions for directional scattering, so we focussed on these.

Using a scanning electron microscope (SEM, in our case the Hitachi S-4800), the nanoparticles can be imaged in more detail. The downside of using a SEM is that it is challenging to image non-conductive samples due to the electrons being used for imaging can accumulate on the sample, which often results in distortion of the produced images.

Images of the silica nanospheres on the glass wafer are shown in [Figure 4.4](#). Images were taken from the top ([Figure 4.4a](#)) and from the side ([Figure 4.4a](#)). In the images, the nanoparticles have bright edges due to charge accumulation at the edge. Also, horizontal stripes can be seen, which is an artifact that results from the scanning direction of the SEM.

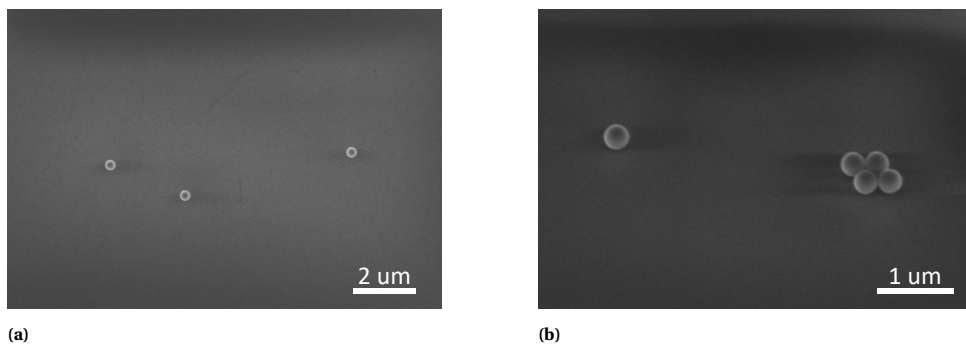


Figure 4.4: Electron micrographs of deposited 300 nm SiO₂ nanoparticles. Imaged (a) from the top and (b) from the side.

After the deposition of the nanoparticles, the core-semishell nanoparticles can be created by evaporation of the shell material onto the glass wafer. Since the evaporation

is very directional, only the top of the spherical nanoparticle is coated.

Evaporation makes it possible for the thickness of the shell to be easily controlled, since the speed at which the layer grows in is the order of 0.1 nm/s. The downside is that not only the nanoparticles are coated, but also the substrate, which would make it unusable for scattering measurements. The upside is that the result can be inspected easily using a SEM when the evaporated material is conducting as shown in [Figure 4.5](#).

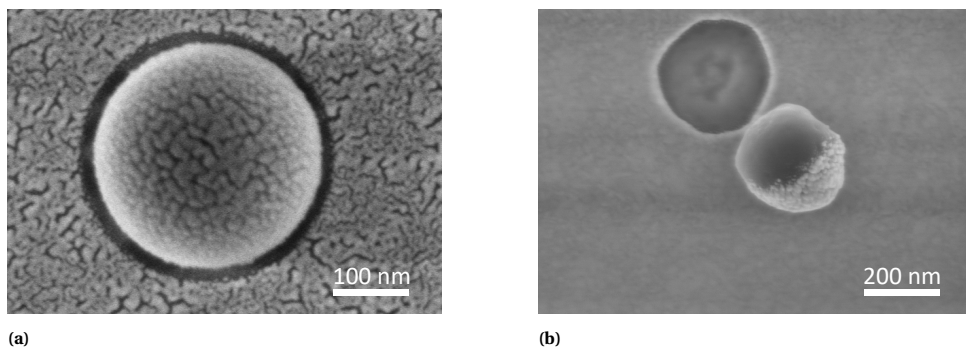


Figure 4.5: Electron micrographs of fabricated core-semishell particles. Top view of [\(a\)](#) a silica nanosphere coated by gold and [\(b\)](#) a knocked over polystyrene nanosphere coated by gold.

In these images, the gold can be recognized due to its structure and its brightness. Gold shows up brighter than silica because gold atoms are much heavier, resulting in a stronger signal by the scattered electrons. The shadow that the nanosphere cast on the substrate is clearly visible from the absence of the gold. In [Figure 4.5b](#), a core-semishell was knocked over by a mechanical jerk, showing the side profile of the nanoparticle.

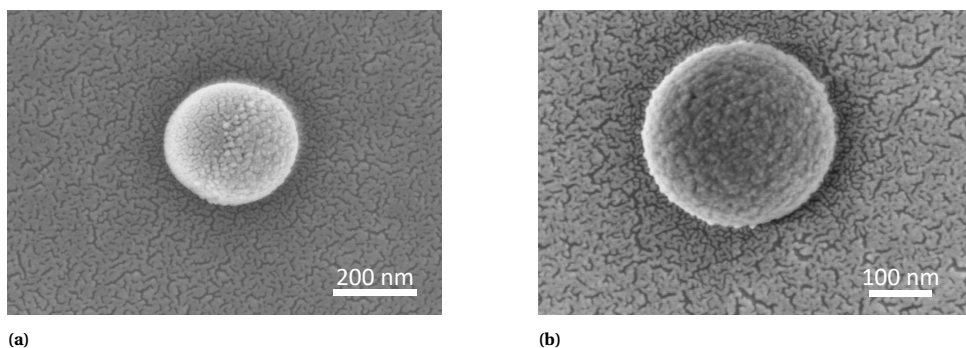


Figure 4.6: Electron micrographs of redeposited core-semishell particles. After redeposition, the sample was sputtercoated with gold to be able to get undistorted SEM images. [\(a\)](#) A redeposited silica/gold core-semishell particle with the shell pointing to the right and [\(b\)](#) a redeposited silica/gold core-semishell particle with mostly the shell visible

Now that the core-semishell nanoparticles are created, they need to be separated from the coated substrate. In order to do that, the wafers are sonicated in a few millilitres

of distilled water, so that we acquire a colloid solution of core-semishell nanoparticles. Similar to the SiO_2 colloid solution, these can be deposited on a glass wafer so that they can be measured.

Due to this method of getting the nanoparticles on the substrate, the orientation of the nanoparticles is completely random. Examples are shown in [Figure 4.6](#), where the redeposited core-semishell particles have been sputtercoated in a thin layer of gold to make SEM imaging possible. A conductive layer is not strictly necessary; however, it does significantly decrease the imaging resolution if it is absent.

Due to the sputtercoating with gold, the difference between the core side and shell side of the core-semishell particle is a bit harder to see but still visible. In [Figure 4.6a](#), the right side of the particle pointing slightly down has a thicker layer of gold, because that is the shell side. In [Figure 4.6b](#), the shell is pointing up. We can see that the layer of gold on the particle is thicker than on the substrate.

4.1.2. PRODUCTION OF ETCHED COMPOSITE NANOPARTICLES

Instead of creating a core-semishell nanoparticle, we could create a particle which does not have such a nicely defined geometry. As we have seen in [Chapter 3](#), the exact geometry of the particle does not significantly affect the scattering pattern. Thus, a similar particle can be created by starting with the bare core particles and creating a partial shell around it.

To achieve this, we start by sputtercoating an almost full shell around the particle. Next, ion-beam etching can be used to etch away most of the shell. If the right materials are selected, only the part of the shell in the *shadow* of the core will remain, while the core and substrate are not significantly affected. By changing the thickness of the sputtered shell and the etching angle, the amount of material of the shell left behind can be controlled.

The advantage of this method is that the orientation of the composite particle can be maintained through the directional etching. Furthermore, no material is left on the substrate besides the composite particles itself, as this is also etched away. A schematic representation of the production process is shown in [Figure 4.7](#).

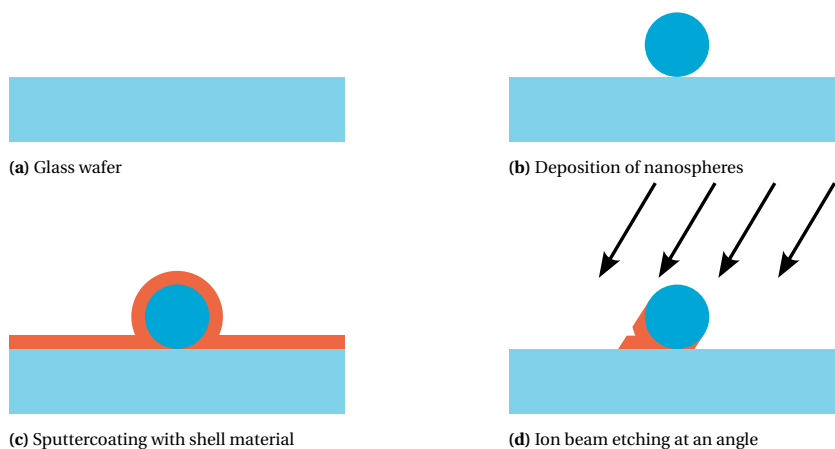


Figure 4.7: Schematic representation of the fabrication process of etched composite nanoparticles. We start with a glass wafer [\(a\)](#), onto which silica nanospheres are deposited [\(b\)](#). Next, the shell material is sputtercoated to cover the entire nanosphere [\(c\)](#). Finally, part of the shell is etched away through ion beam etching [\(d\)](#).

For these nanoparticles, the process was the same for the deposition of the nanospheres. After the deposition, the silica nanospheres were sputter coated with 40 nm of gold, so that enough gold will be left over after the etching step. The samples were then etched for a few minutes using Ar ion beam etching using the SCIA mill 150. Gold is etched much faster than silica, depending on the angle there is a factor of more than 4 difference in etching rate.

From sample inspection using a SEM, it was found that 8 min of etching was sufficient to remove all the gold except the part remaining in the shadow of the nanospheres. The results are shown in [Figure 4.8](#). Note that the quality of the images is significantly reduced compared to the images in [Figure 4.5](#) and [Figure 4.6](#) due to

charging effects during imaging.

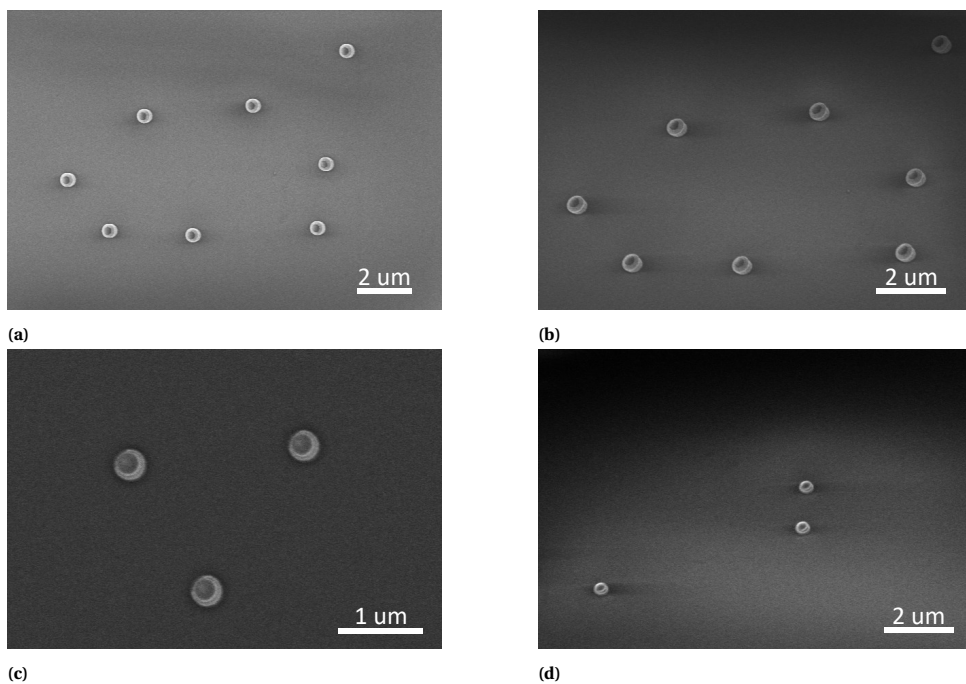


Figure 4.8: Electron micrographs of fabricated silica / gold composite nanoparticles on a glass substrate. (a) Top view and (b) side view of silica / gold composite nanosphere which have not been etched through yet. (c) Top view and side view (d) of fully etched silica / gold composite nanosphere

4.2. FABRICATION OF GRATINGS

The gratings were made using e-beam lithography. Instead of using borosilicate glass like before, fused silica wafers were used. The reason for this will be clear later in this section. First, a thin layer of metal was evaporated on the surface of the fused silica wafers. This is needed for the lithography step for two reasons.

First, a conductive surface is needed so the electrons can be carried away. If there was not such a layer, the electron would get stuck near the place there were fired at. As a result, this place would gain a charge and repel further electrons. This would have negative effects on the pattern produced. Second, the location of the surface is determined using a laser reflecting of the surface and for this to work the reflectivity of the surface must be high enough to get a good measurement.

For this conductive layer we have chosen 25 nm of titanium. This is because it can easily be removed in a later step of the fabrication process. A thickness of 25 nm provides a surface that is reflective enough for the height calibration sequence of the e-beam pattern generator, while not making the layer too thick.

After the titanium layer has been deposited on the surface, the resist ARN7520.17 NEW by Allresist is spincoated on top. The resist is sensitive for the electrons coming from the e-beam, which changes its chemical resistivity to solvents. We are using a negative resist, so that the exposed resist will remain on the wafer after development.

Depending on the desired height of the grating, different spin speeds were used which result in different resist film thicknesses. After this, the thickness was measured using ellipsometry or reflectometry. The results of which are shown in [Table 4.1](#).

Resist	Spinspeed (rpm)	Resist thickness by ellipsometry/reflectometry (nm)	Glass structure height by profilometer (nm)
ARN 7520.17 NEW	1000	875	750
	1300	780	700
	1500	740	675
	2000	625	580
	2250	590	570

Table 4.1: Resulting resist thin film thicknesses and glass structure height depending on used spin speeds

Next is the lithography step. A design is uploaded on the machine, which will then expose the resist according to this design. A 5 by 5 mm grating was designed using a beam step size of 25 nm and an electron beam spot size of 37 nm. Dose tests were performed to determine the dose so that the resulting structures have the same dimensions as specified by the design file. The dose found to produce the best resist structures with ARN7520.17 NEW was $300 \mu\text{C}/\text{cm}^2$.

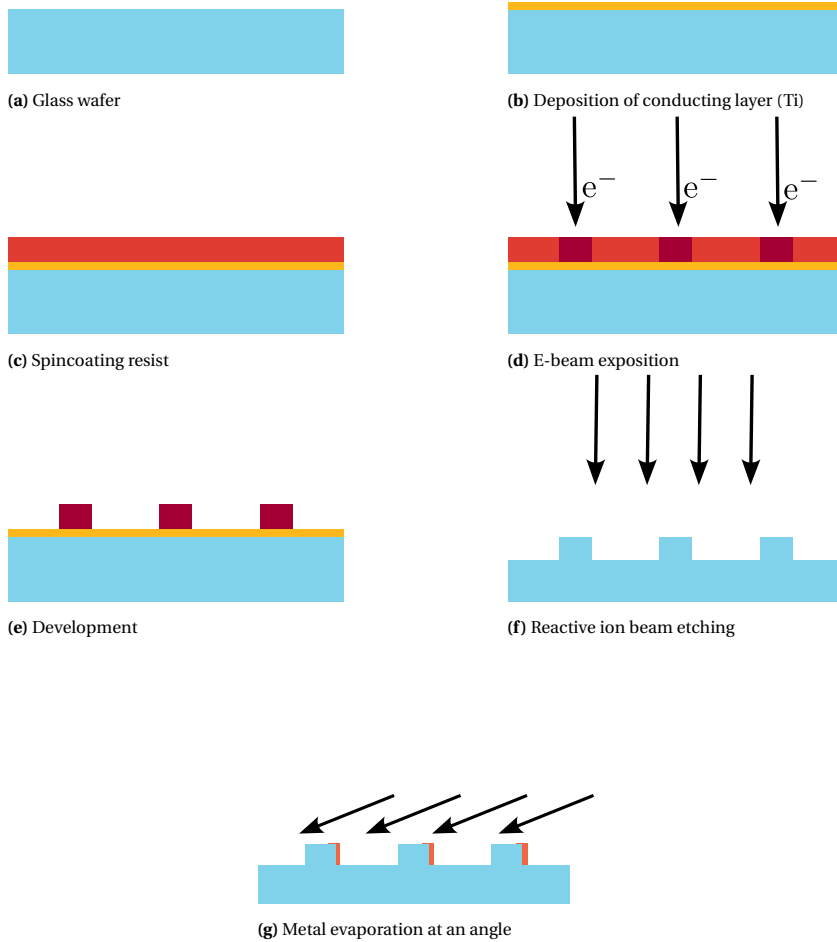


Figure 4.9: Schematic representation of the fabrication process of composite rectangular nanoparticles. We start with a glass wafer (a), onto which a conducting layer is deposited (b). The sample is then spincoated with resist (c) and exposed using e-beam (d). Next, the grating lines are developed (e) and etched into the glass substrate (f). Finally a second material is evaporated at an angle to cover the side of the grating lines (g).

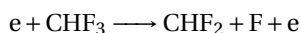
After this, the pattern needs to be developed; the part of the resist that has not been exposed by the e-beam needs to be removed. The patterns were developed using *Microposit Developer MF322*, a basic solution. First, the exposed wafers were placed vertically in a bath of MF322 for 60 seconds. Then in a bath of 1:9 MF322:H₂O solution for 15 seconds, a bath of H₂O for another 15 seconds and were finally left in another bath of H₂O for at least 15 seconds. While in solution, the samples were moved around manually to allow for the basic solution to reach all the unexposed resist.

After development, the resulting nanostructures made of resist were inspected using an optical microscope. An example is shown in [Figure 4.11a](#) and [Figure 4.11b](#). To confirm the height of the nanostructures with the measurements of the ellipsometer and reflectometer, the samples were measured using a profilometer.

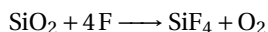
Next, the pattern needs to be transferred into the layer beneath it, which is done by reactive ion beam etching. Here, the glass is etched away chemically using a plasma with chemicals which can react with the glass. The left-over resist will mask the underlying material from being etched away. During the etching, the resist itself will also be etched away slowly. Therefore, the (maximum) height of the structures which are etched into glass are determined by the resist height.

The Sentech Etchlab 200 plasma etcher was used to do the etching of the glass. Several combinations of the gasses CF₄, CHF₃, Ar and O₂ were tried. Eventually we settled for etching with only CHF₃, as this produced the best selectivity. This allowed for the production of structures up to a height of about 750 nm using this resist and etch process. Reflection interferometry was used during the etching process to determine when all of the resist and the underlying titanium layer had been fully etched away. The height of the structures was measured using a profilometer, the results are also shown in [Table 4.1](#).

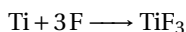
The gas undergoes several chemical reactions, so that the glass can be etched. First the F-radicals are created through the impacts of electrons in the plasma:



The fluoride then reacts with the glass following the reaction:



Furthermore, the titanium layer that was deposited for the e-beam step is etched away following the reaction



Reactive ion etching is not purely a chemical process. The physical impact of the ions hitting the sample also etches away material. While the effect on the glass is very limited, this is part of the mechanism by which the resist mask is etched away. The other part is chemical due to the oxygen that is released after the glass has reacted with the fluor radicals. The oxygen reacts with the resist and etches it away as well.

RIE settings	
Gasses	CHF ₃ 50 sccm
Microwave power	100 W
Bias voltage	-280 V
Pressure	11 μbar

Table 4.2: Settings used for the reactive ion etching of fused silica samples

Initially, borosilicate glass substrates were used (Schott D263 T Eco) . However, due to the additions of boron and other metals, etching is more difficult than it is for a pure form of glass: fused silica. Because of the additional metals, which do not react with the fluorine, oxygen or argon had to be added to the gas mixture. As a result, the resist would also etch away faster, making it difficult to obtain structures which were high enough.

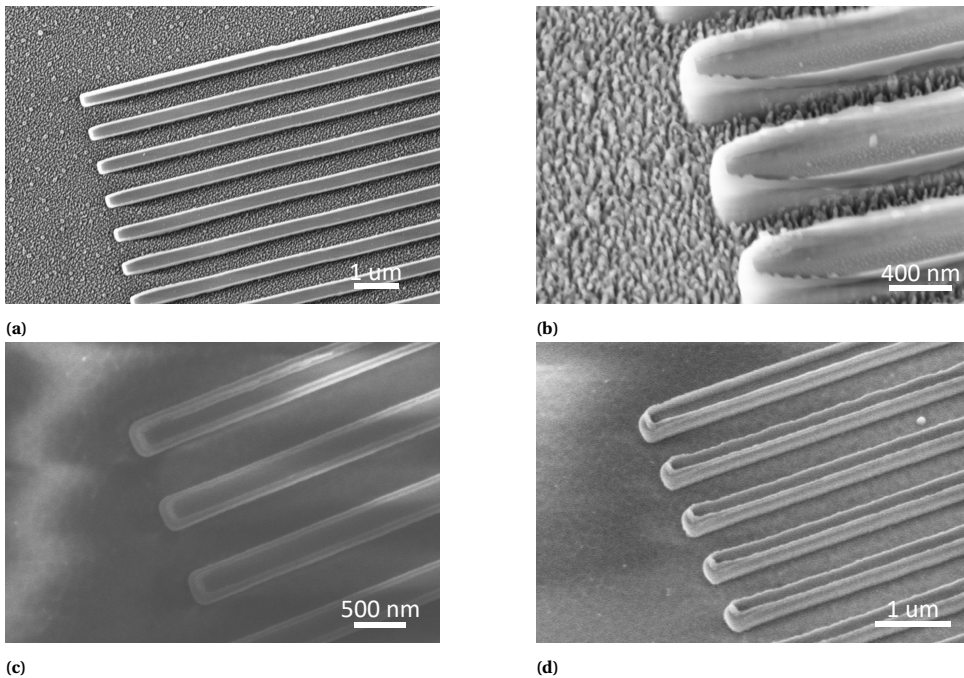


Figure 4.10: Electron micrographs from etched borosilicate substrates. (a) Top view and (b) side view which show the surface texture obtained after reactive ion etching. (c) Top view and (d) side view which shown the surface after subsequent argon etching. Note that due to the smoother surface, the SEM images are of lower quality due to charging. In (b) and (d), the sidewalls due to redeposition can be clearly observed.

When not enough argon or oxygen was added to the gas mixture, the leftover additives would shield the glass below it from being etched. This would result in a very rough surface texture. This could be fixed by a subsequent argon etching process, however it would make the fabrication process more complicated. The surface before and after the argon etching process can be seen in Figure 4.10. In Figure 4.10a and

Figure 4.10b, it can be seen that the surface has a structure which looks like small peaks. After the argon etching in Figure 4.10c and Figure 4.10d, the surface looks much more smooth.

Finally, we think that the additives which do not create volatile materials, would get redeposited onto the structures. This results in sidewalls being added to the structures we are trying to create out of glass. These sidewalls can also be seen in Figure 4.10b and Figure 4.10d. Although the creation of these sidewalls were not reported in the literature[68, 69], this was the main reason for us to switch to fused silica as a substrate. Using fused silica, we did not see any formation of sidewalls and we were able to create the structures in glass more easily.

After inspection, part of the grating elements were coated by a metal by evaporation at an angle. This way, only one side of the grating elements would be covered with metal and the space between the elements would not be covered. The combination of the layer thickness and the angle at which the sample is coated determines the volume of the deposited metal. This is what determines the final scattering behaviour as discussed in Section 3.2.

A schematic representation of the entire production process is shown in Figure 4.9. Note that the geometry of the grating elements is different from what we have considered in Chapter 3. The reason for that is that initially we had a different method of fabrication in mind, which did not end up working. However, as we have discussed the geometry does not have a significant effect on the scattering direction of the elements.

In contrast, the refractive index is very important. Therefore, the properties of the deposited layer have to be controlled very carefully, as the optical properties of it changes compared to the bulk material at the scale of the amount of material we want to deposit (thicknesses of a few tens of nanometers). Particularly for metals, where the absorption is significantly increased in the optical spectrum for thin films[70–74].

Different metals are affected differently, as their formation on the sample surface during the deposition is also different. Furthermore, more homogeneous films are generally created with slower deposition speeds. However, too slow deposition could result in more impurities being included from the environment. Accordingly, the speed at which the layers were grown was set to 0.05 nm/s. Samples with different materials and thicknesses (by changing the exposition time) were fabricated.

As another attempt to reduce the absorption by the metal, annealing of the samples was tried. This has been shown to reduce the absorption in certain conditions[75]. For samples with titanium specifically, titanium nitride can be created when annealing in a nitrogen environment[76] through the following chemical reaction:



Titaniumnitride has a much smaller imaginary part of its permittivity for optical frequencies[77], possibly resulting in less absorption while maintaining the conditions for directional scattering as proposed in Chapter 3.

Gratings were fabricated with a pitch of 775 nm, a width of 250 nm and a height of 520 nm. Results of the developed resist in the form of grating lines are shown in [Figure 4.11](#).

In the optical micrographs, a gradient can be seen towards the inside of the gratings. This is likely because that during the development of the resist, the developer can more easily get to the edges of the grating than to the center. Measurements using a profilometer of the resulting gratings have shown that this difference is only a few nanometers and therefore will not impact the performance of the grating.

In the electron micrographs, we can see that the lines have very straight sidewalls, which mean that they will provide a good mask for the etching of rectangular gratings into the glass substrate.

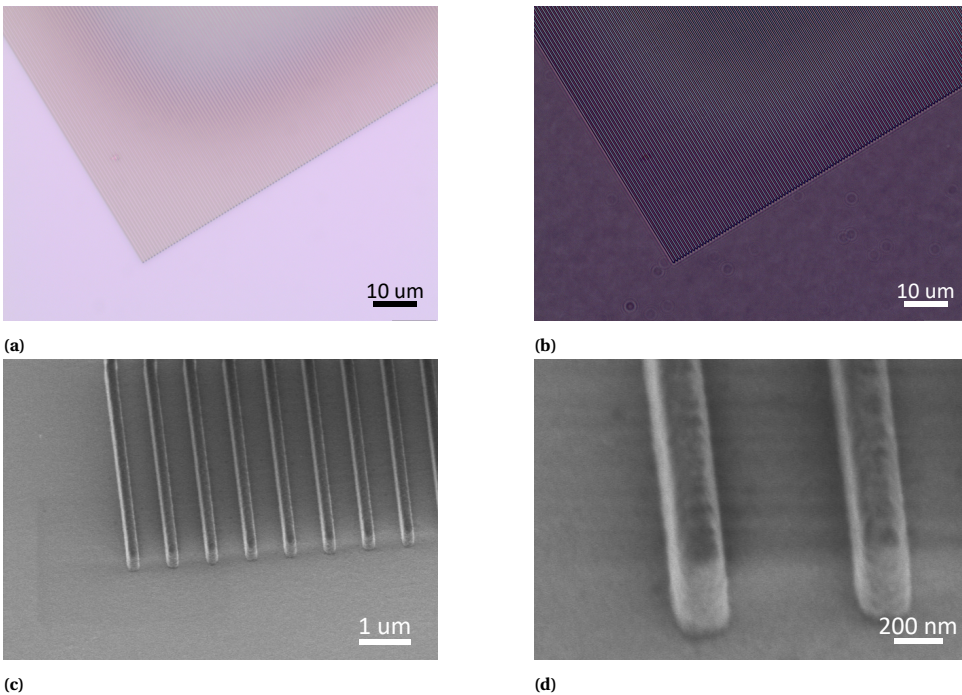


Figure 4.11: Optical micrograph (white light) of the fabricated resist structures in [\(a\)](#) reflection and [\(b\)](#) transmission of the grating lines made of resist. Note that the lines appear broader, because their width is below the diffraction limit. Electron micrographs of the fabricated resist structures of [\(c\)](#) the corner of the grating and [\(d\)](#) zoomed in onto two elements.

The resulting fused silica gratings, obtained after the reactive ion etching step are shown in [Figure 4.12](#). In [Figure 4.12a](#) and [Figure 4.12b](#), the gratings are shown as you would see them with the naked eye. The colored square on the glass wafer is the grating of 5 by 5 mm.

In [Figure 4.12c](#) and [Figure 4.12e](#), we can see that the resulting gratings elements are not completely rectangular, there is a slight slope to the sidewalls and the top of the grating elements are slightly thinner than the bottom. A method for solving this would be to use a hard mask like chrome instead of a soft mask. As this would result in a more elaborate fabrication process we have chosen not to do this. Furthermore, as we have seen in [Section 3.2.3](#), the exact shape does not matter much for the directional scattering. Because the height of the grating lines is not constant, it could be that the 0th order is not suppressed as much as expected from [Section 3.3](#).

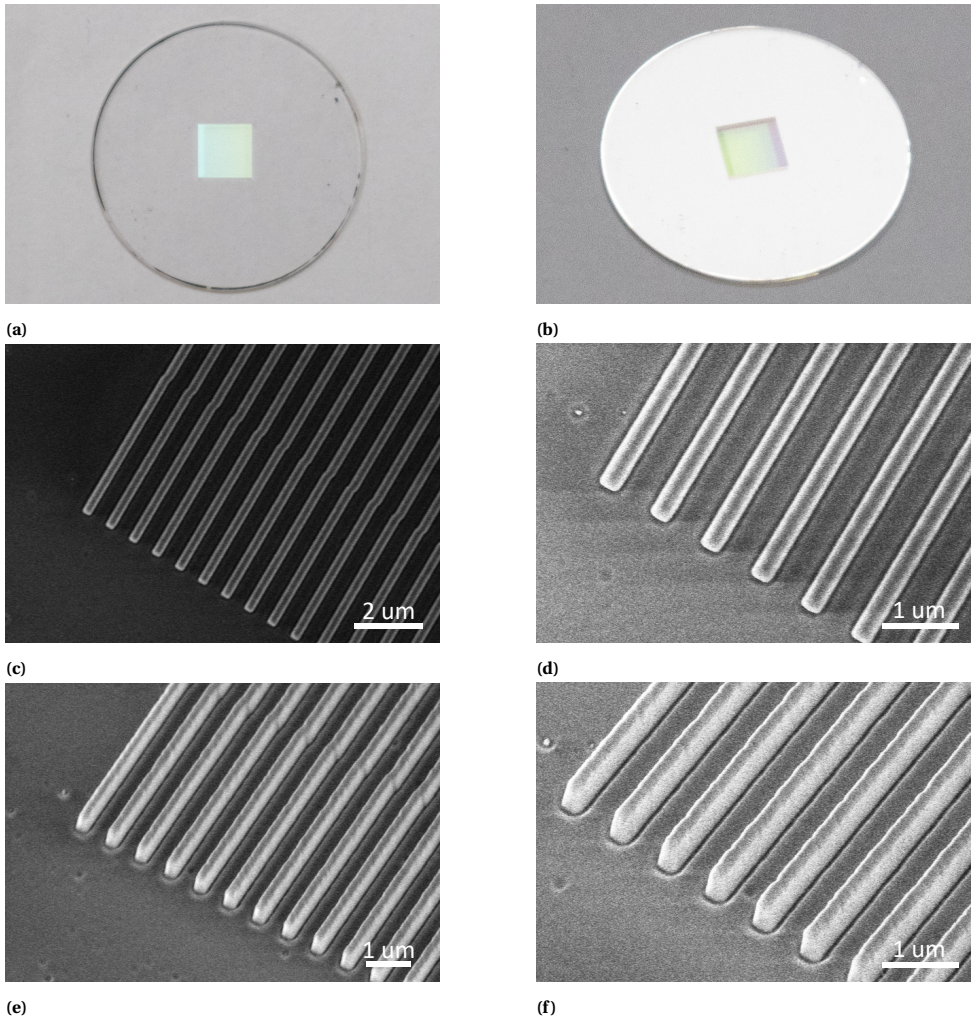


Figure 4.12: The fabricated glass gratings. (a),(b) Photos of the glass grating etched into the glass wafer and (c),(d) electron micrographs from the top and (e),(f) from the side at an angle of 30 degrees.

In [Figure 4.12c](#) and [Figure 4.12e](#), a discontinuity in the grating lines can be seen. This is due to the limited field of view of the e-beam pattern generator. When writing, the electron beam is moved using magnets which provides a very accurate control over the position. However, if the pattern to be printed is larger than the field of view, the stage has to move. This has a limited accuracy, resulting into an error in position of several nanometers. For measurements, we do not expect this to have a significant impact.

Afterwards, the spectral response of the gratings were measured to get a baseline (see [Chapter 5](#) for further details). Next, the samples were cleaned through sonication in acetone for 5 min and subsequent cleaning in an oxygen plasma for 2 min. Then, the metal was deposited onto the gratings. The metals gold, silver, platinum and titanium were investigated. Photos of the resulting composite gratings are shown in [Figure 4.13](#). SEM images of the grating elements are shown in [Figure 4.14](#), [Figure 4.15](#), and [Figure 4.16](#).

Results from annealing samples at 400°C for 4 hours in a nitrogen environment are shown in [Figure 4.17](#) for silver and [Figure 4.18](#) for titanium, in which case titaniumnitride was created.

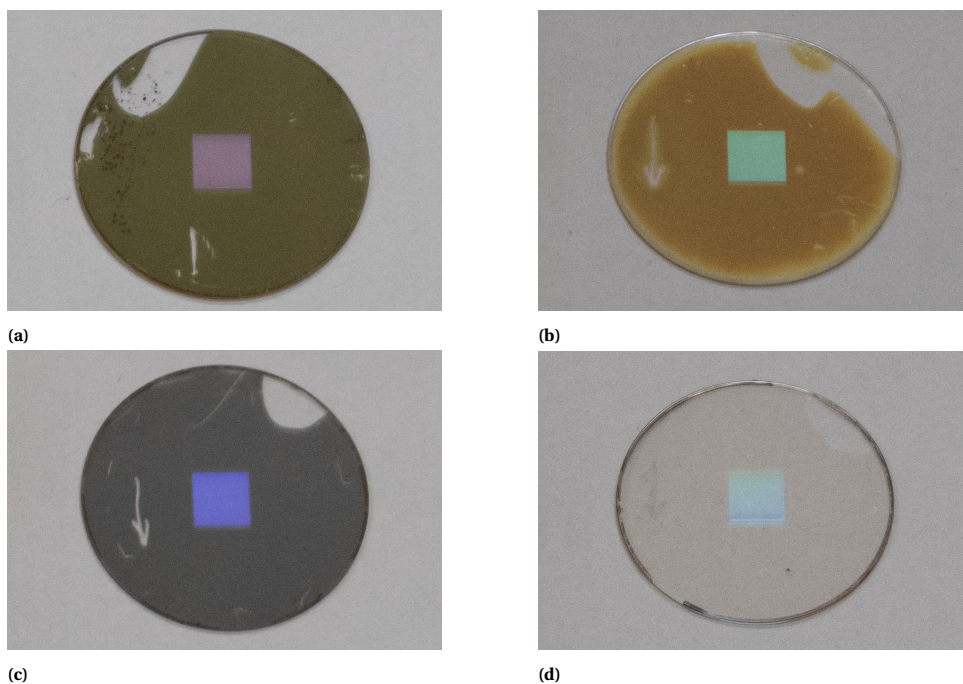


Figure 4.13: Photos of the fabricated composite gratings with (a) gold, (b) silver after annealing, (c) platinum and (d) titaniumnitride. Due to the annealing, the color of the silver on the substrate shown in (b) has turned brown.

For the gold composite gratings shown in [Figure 4.14](#), the glass gratings were more triangular shaped. The reason for this is not known, as the other fabricated gratings did have a rectangular shape. Due to the high contrast that gold provides in SEM imaging,

the difference between the side coated by the gold and the glass side can clearly be seen.

Also note the difference between the bottom of the gold and top in [Figure 4.14b](#), while the bottom edge is nice and straight due to the shadowing of the neighbouring grating line, the top line is very rough. This top line could be the cause of increased diffuse scattering and absorption.

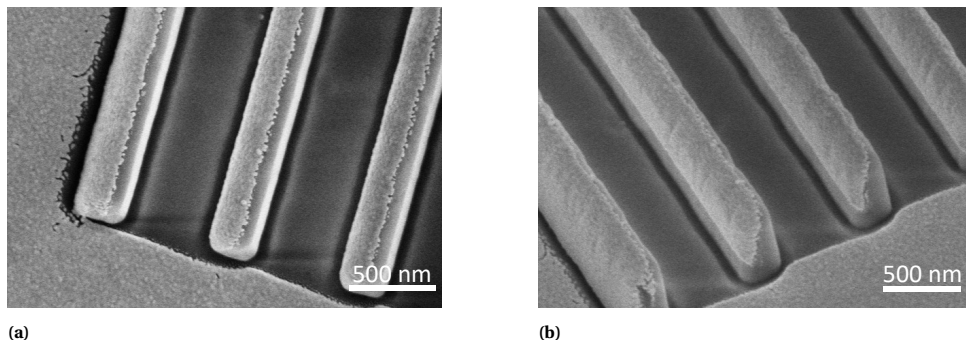


Figure 4.14: Electron micrographs of the fabricated gold composite gratings. The gratings were imaged (a) from the top and (b) from the side at an angle of 30 degrees.

In [Figure 4.15](#), the shadowing effect of the evaporation of platinum at a large angle can clearly be seen. The platinum does not consist of a uniform film, it is likely that this will increase absorption and diffuse scattering. By increasing the layer thickness, some improvement of the grating performance may be possible.

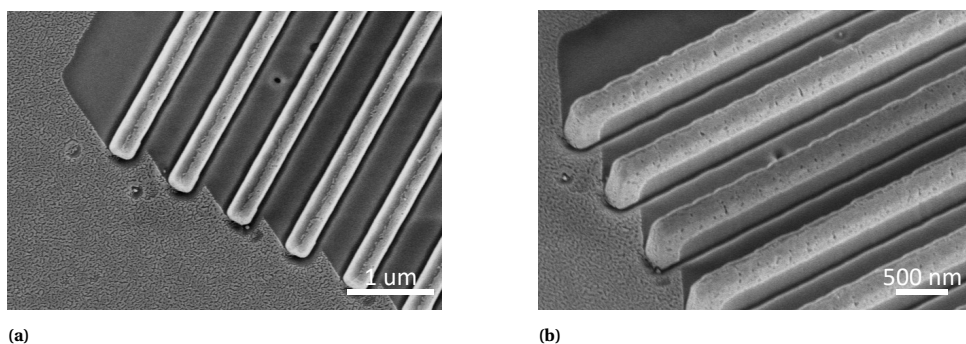


Figure 4.15: Electron micrographs of the fabricated platinum composite gratings. The gratings were imaged (a) from the top and (b) from the side at an angle of 30 degrees.

For the composite gratings with titanium in [Figure 4.16](#), imaging the grating is more difficult. This is due to the formation of a native oxide layer of titaniumdioxide on top of the deposited titanium, which is not conducting. Furthermore, titanium has a much lower atomic weight than gold, platinum and silver, resulting in less contrast.

Because of the limited image quality, only images from the top were made. While the shadow due to the evaporation can clearly be seen, the evaporated titanium on the grating lines is not visible on these images.

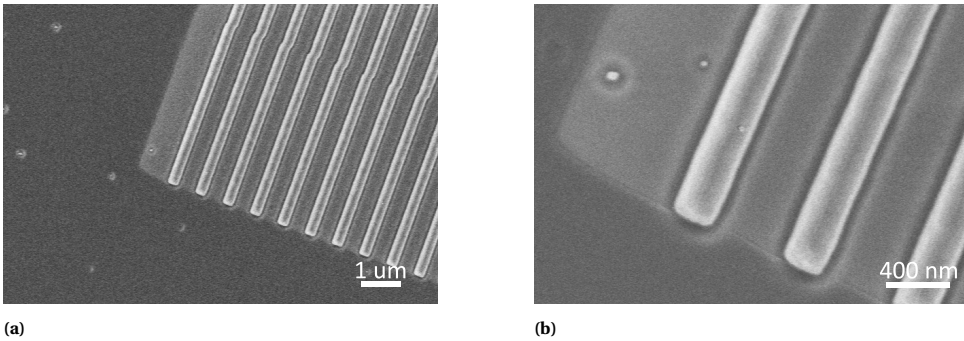


Figure 4.16: Electron micrographs of the fabricated titanium composite gratings, imaged from the top.

The SEM images for the composite grating with silver that are shown in [Figure 4.17](#) were made after annealing. The formation of small islands can be seen on the substrate and on the side of the grating lines. This is further discussed in [Section 5.5](#).

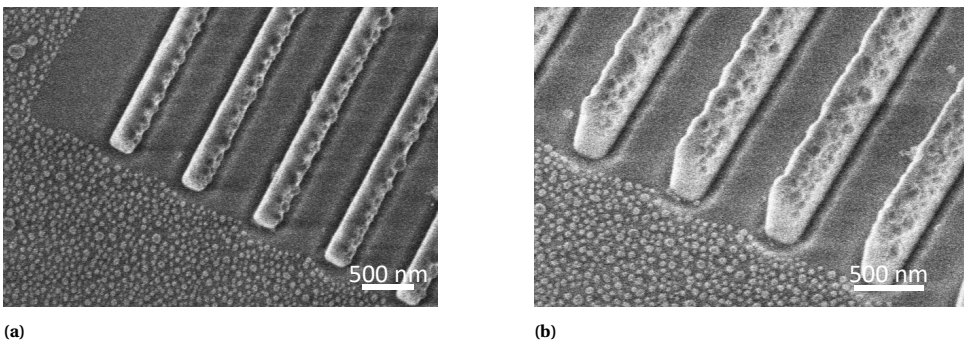


Figure 4.17: Electron micrographs of the fabricated silver composite gratings which have been annealed. The gratings were imaged (a) from the top and (b) from the side at an angle of 30 degrees.

Similarly to the composite gratings with titanium, the composite gratings with titanium nitride shown in [Figure 4.18](#) are only imaged from the top. This is because the sample has even lower conductivity than the titanium samples. Unfortunately, no discernible differences can be observed with respect to the titanium samples in [Figure 4.16](#), except for the further decrease in image quality.

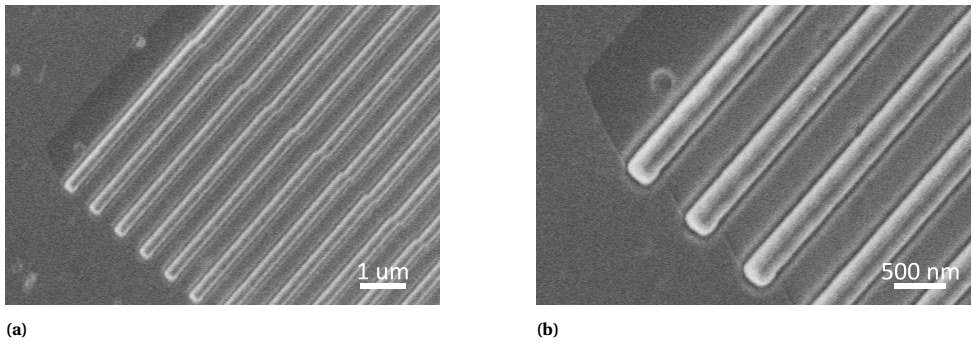


Figure 4.18: Electron micrographs of the fabricated titanium nitride composite gratings, imaged from the top.

4.3. SUMMARY AND OUTLOOK

In this chapter we have presented several methods for the fabrication of composite nanoparticles and gratings. For the fabrication of composite nanoparticles, the use of colloidal nanospheres is preferred, because of the ease of fabrication. With only one simple step in the form of evaporation, composite nanoparticles can easily be made. However, the downside is that the substrate is also covered, requiring more steps to remove the nanoparticles from the substrate and deposit them on another. As a result, the orientation of the particles is randomized, making subsequent experiments difficult.

By sputter coating the nanospheres and ion beam etching at an angle, the composite nanoparticles can be made with just one step extra. The advantage is that the orientation is well defined, allowing for easy optical experiments to determine the scattering characteristics of the produced nanoparticles. Therefore, these are the nanoparticles that will be used in [Chapter 5](#).

For the fabrication of gratings, e-beam lithography is required. A substrate made of fused silica was used, as borosilicate glass contains additions which hinder the etching process to create the nanostructures. Once a glass grating was created, the creation of a composite grating is easily done by evaporation of a metal at an angle, so that no metal is deposited between the grating lines.

It is important to be aware of the change in optical properties of ultra-thin films, as they are very dependent on the film formation process. In particular, ultra-thin films of metals generally have more absorption than in their bulk form.

As we have seen in [Chapter 3](#), it is not required to use metals to get directional scattering. Rather, since the permittivity needs to be complex, semiconductor materials can also be used. Such a material can be created by annealing titanium in a nitrogen environment to obtain titaniumnitrate.

All of the described methods in this chapter are easily scalable (or are able to be adapted to be scalable in the case of gratings), and therefore could potentially be used in the production of new technologies which use broadband directional scattering in the visible spectrum.

In [Chapter 5](#), the measurements of the composite nanoparticles and grating which were fabricated in the methods described in this chapter will be discussed.

5

MEASUREMENTS OF SCATTERING COMPOSITE NANOSTRUCTURES

“

Experiment is the sole source of truth. It alone can teach us something new; it alone can give us certainty.

Henri Poincaré[9]”

IT is important to validate our theory by measuring the nanostructures which have been designed in [Chapter 3](#) and fabricated in [Chapter 4](#). We will experimentally determine the scattering by single composite nanoparticles and we will analyse the performance of the produced gratings.¹

Measuring individual particles that are this small is not easy, because only a fraction of the incident light is scattered by them. In this chapter, the Fourier microscope setup for measuring these particles is presented. The optical setup is discussed and calculations are made to determine the approximate amount of light that is scattered by the particles in [Section 5.1](#). Then, the measurement results of the fabricated particles are shown and discussed in [Section 5.2](#) and [Section 5.3](#).

For the composite gratings, their performance is determined using a goniometer. The experimental setup is discussed in [Section 5.4](#). The diffraction efficiency is calculated and compared to that of a bare glass grating in [Section 5.5](#).

¹[Section 5.3](#) of this chapter is the extended version of the results in our paper *Broadband directional scattering through a phase difference acquired in composite nanoparticles*[45], while [Section 5.5](#) is the extended version of the results in our paper *Method for designing highly efficient composite transmission gratings*[46]

5.1. MEASUREMENT SETUP FOR SINGLE NANOPARTICLES

The nanoparticles are measured in transmission to determine their scatter pattern. The optical setup is shown in Figure 5.1, where the nanoparticles are illuminated with a HeNe laser at a wavelength of 633 nm. Because the nanoparticles do not scatter so much light, a relatively high power laser of 10 mW is used.

First, the laser beam passes through a spatial filter to clean up the beam profile and obtain a nice Gaussian distribution. Then, the laser beam is redirected by two mirrors towards the sample. An iris is placed in front of a focusing lens so that most of the light that is scattered by the mirrors is blocked.

The laser is then focused on the sample using a best form lens. This lens is not completely filled, as a result the effective NA is limited to about 0.10. The sample is placed vertically on a sample holder attached to a motorized XYZ stage. Then, a 100x 0.85 NA microscope objective is used to collect the scattered light. The nanoparticles are on the side of the substrate closest to the microscope objective.

After this, a tube lens is used to create an image in the image plane. At this image plane, another iris is placed which has an aperture which is slightly bigger than the focus spot size in the image plane. This is done so that as much of the light that is scattered elsewhere than the object plane is eliminated. As a result, the field of view is limited to the size of the aperture.

Because the incident light that did not interact with the particle is much more intense than the scattered light, it needs to be blocked. Otherwise, the camera at the Fourier plane would become saturated, making an accurate measurement impossible. Thus, the Fourier plane is projected by a lens onto a glass plate with a central obstruction.

A second lens is used to go back to the image plane. A beamsplitter is placed after the lens such that we can measure in both the image plane and the Fourier plane at the same time. A camera is placed at the transmission side of the beamsplitter which effectively turns this part of the setup into a darkfield microscope.

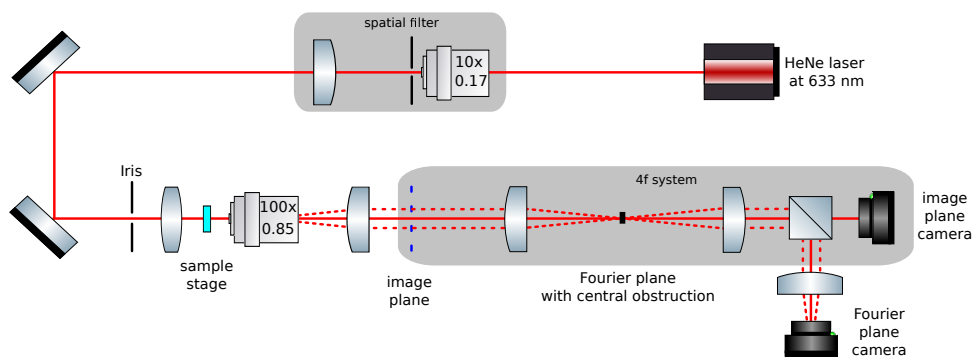


Figure 5.1: Schematic representation of the optical setup used to measure the scatter pattern of nanoparticles. Rays coming from the back focal plane are dashed.

The light reflected by the beamsplitter passes through a lens to project the Fourier plane on the other camera. The measurements made by this camera is what we are

mainly interested in. The images produced by the camera in the image plane is used to determine the position and focus of the nanoparticles.

To illustrate the difficulty of measuring individual nanoparticles, we can make a rough approximation of the amount of light that is scattered by a single silica nanoparticle with a diameter of 300 nm. Using Mie theory (which is discussed in [Section 2.3](#)), we can determine the scattering cross section of the particle as if it was suspended in air.

We obtain a scattering cross section of $\sigma_{sc} = 2.8 \cdot 10^{-15} \text{ m}^2$. To determine the power of the scattered light, we can compare it by the size of the focussed spot on the sample of the laser. For a spot with a diameter of $8 \mu\text{m}$, which is achieved in practice, this is equal to an area of $A = 5.0 \cdot 10^{-11} \text{ m}^2$. The power of the scattered light by the nanoparticle is then equal to $P_{sc} = \frac{\sigma_{sc}}{A} P_0$, with P_0 the power of the laser that is used. We use a laser of 10 mW, so this comes down to a value of $P_{sc} = 560 \text{ nW}$. From this calculation it is clear that any other background signal will be problematic during the experiments, as the scattered light by optical components is of similar magnitude.

Because the scattering by the nanoparticles is polarization and orientation dependent, four measurements are performed for each nanoparticle:

- Symmetry axis of the particle along the x-axis, polarization along the x-axis.
- Symmetry axis of the particle along the x-axis, polarization along the y-axis.
- Symmetry axis of the particle along the y-axis, polarization along the x-axis.
- Symmetry axis of the particle along the y-axis, polarization along the y-axis.

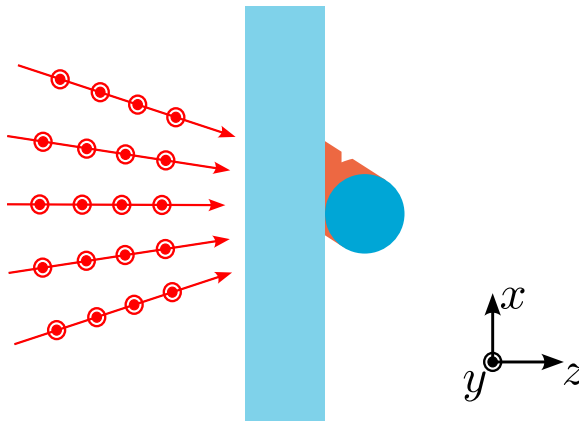


Figure 5.2: Schematic representation zoomed in on the sample. Laser light from the left polarized along the y-axis is focussed onto a single particle on the sample substrate. In this drawing, the symmetry axis of the particle is along the x-axis.

By taking the measurements at different polarizations, we can determine the dependence on polarization of the scatter pattern (see [Figure 5.2](#)). By taking measurements with different orientations of the particle by rotating the stage, we

can be sure that the directional scattering is due to the particle if the scatter pattern rotates with the particle.

5.2. POSTPROCESSING OF MEASUREMENTS

An issue with such a setup using a coherent source is that reflections in this system can cause interference artifacts in the Fourier plane. Since the intensity of the scattered light by the nanoparticles is very limited, it is comparable to light scattered of the optical components of the measurement system.

A different source with lower coherence could not be used, because such sources cannot be focussed down to a small enough spot. As a result, even more background signal would be present, making it harder to get accurate measurements.

To counteract this, a measurement was made on a part of the sample where no nanoparticles were present. Both this measurement and the nanoparticle measurement were Fourier filtered using a low pass filter to remove interference effects. Next, the background was subtracted from the measurement to obtain a measurement of the light scattered by the nanoparticle.

Because of the coherence of the source, this process introduces some artifacts, as the subtraction process does not take interference into account. [Figure 5.3](#) shows the process for a particle with its symmetry axis along the y -axis with x -polarized light incident on the sample.

Initially, the sample was moved to a place where the laser spot would not illuminate any particles. A measurement was taken, obtaining a back focal plane image as shown in [Figure 5.3c](#). To the left of the obstruction, a reflection can be seen. This is likely light that is reflected off the first surface of the tube lens, and then reflected by the last surface of the microscope objective. The reflection is off-centre due to imperfect alignment.

Next, the sample is moved so that the focal spot is centered on a single nanoparticle. The back focal plane image acquired is shown in [Figure 5.3a](#). It can be seen that the image is slightly brighter, indicating that more light is scattered than before. The same reflection to the left of the central obstruction can be seen as well. Above the central obstruction, slightly to the left clear interference can be seen. It is unknown what the cause of this is.

To remove the unwanted effects, both the image of the particle and the background image are Fourier filtered using a low pass filter. The results are shown in [Figure 5.3b](#) and [Figure 5.3d](#). From here, the difference between the images is already much clearer, where the directional scattering by the nanoparticle can be recognized.

To produce the final image, where only the scattering by the nanoparticle is included, the difference of the filtered images is taken. The result is shown in [Figure 5.3e](#). Note that the reflection which is present in both the particle and background measurements results in an artifact in the final image. However, the directional scattering which we want to prove can still clearly be seen.

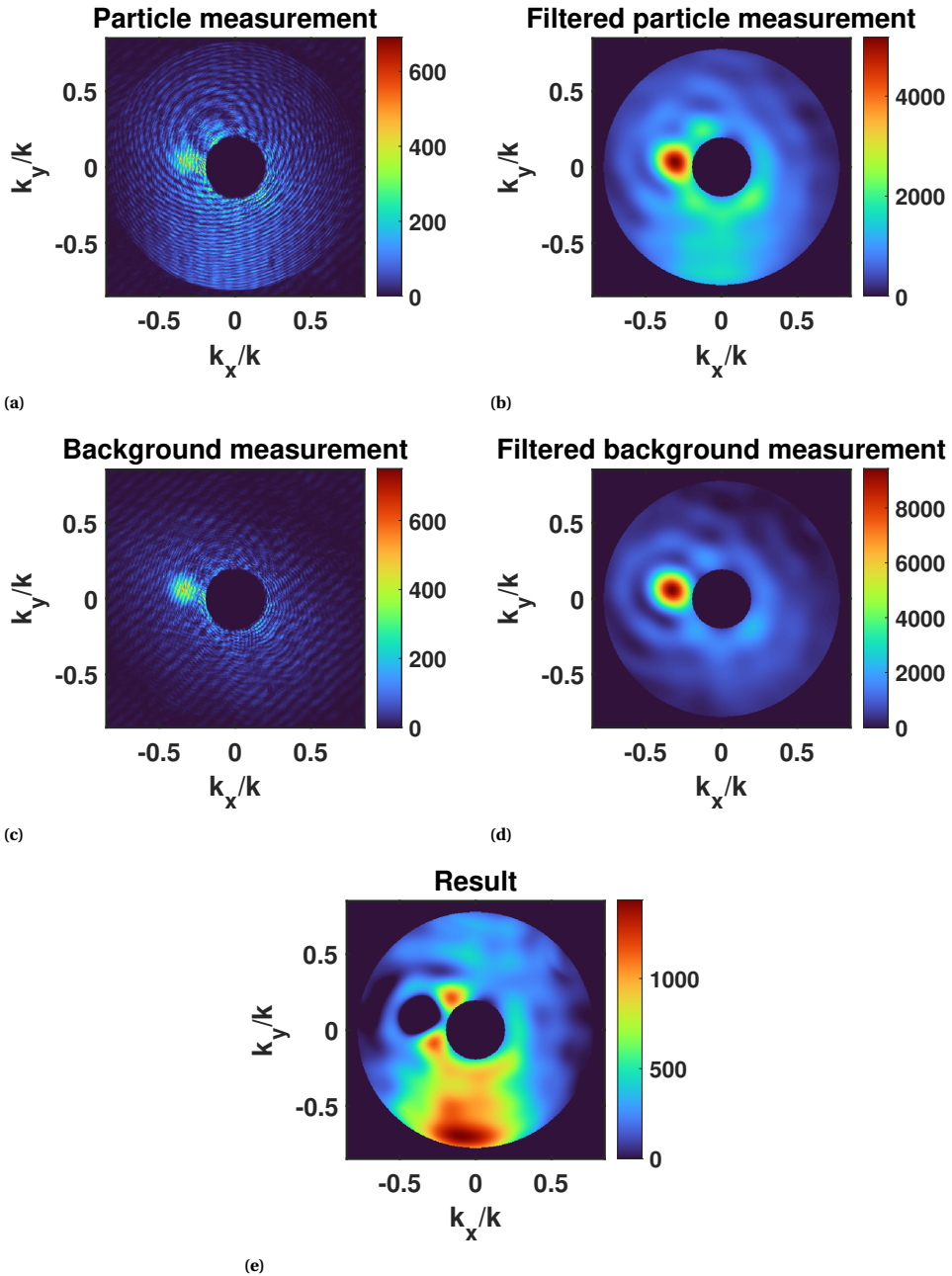


Figure 5.3: Post-processing steps which were taken for the measurements, the colorbar show arbitrary intensity values. (a) Direct nanoparticle measurement. (b) Fourier filtered nanoparticle measurement. (c) Raw background measurement. (d) Fourier filtered background measurement. (e) Result after subtracting (d) from (b), negative values were set to 0.

5.3. MEASUREMENTS OF COMPOSITE NANOPARTICLES

For the measurements of the scattering by composite nanoparticles, the samples obtained through fabrication method 2 using the colloidal particles were used (see [Section 4.1.2](#)). The results are shown in [Figure 5.4](#) and [Figure 5.5](#).

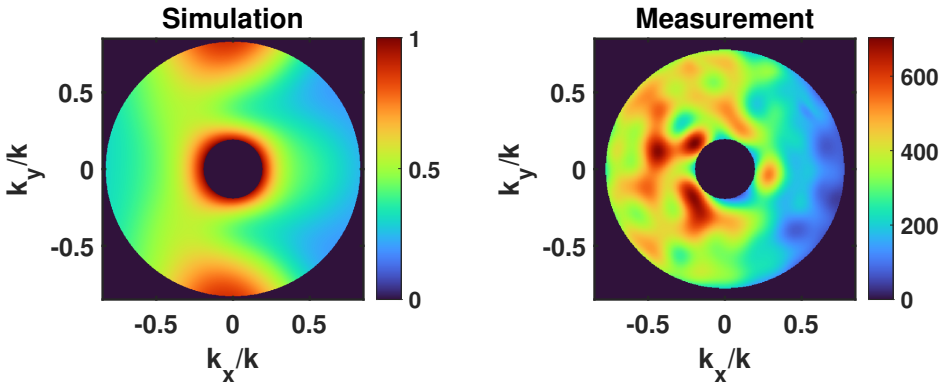
For the case where the polarization axis of the incident light is along the symmetry axis of the particle ([Figure 5.4b](#) and [Figure 5.5d](#)), we see that the scattering is slightly asymmetric with respect to the polarization direction as is also expected from simulations ([Figure 5.4a](#) and [Figure 5.5c](#)). The more detailed directionality towards the edge of the NA is not recovered. This is likely due to the limited signal to background ratio.

In [Figure 5.4d](#) and [Figure 5.5b](#) the case where the polarization axis of the incident light is perpendicular to the symmetry axis of the particle is shown. While the measurements do show directional scattering, it does not fully agree with the FEM simulations shown in [Figure 5.4c](#) and [Figure 5.5a](#) (for details on the simulation see [Appendix B](#)). There are a few reasons why this could be the case. First, the high intensity is located more to the edge of the NA. Because the raw measurement data is Fourier filtered to remove high spatial frequencies, the intensity at the boundary of the NA is reduced. Second, the optical constants used for the materials may deviate from the ones used in the simulations.

Furthermore, the procedure for the removal of background signal could have introduced some artifacts as we have shown in the previous Section. Because the background signal is not constant and also depends on the position of the substrate, there are places where too much or too little of the background signal has been removed.

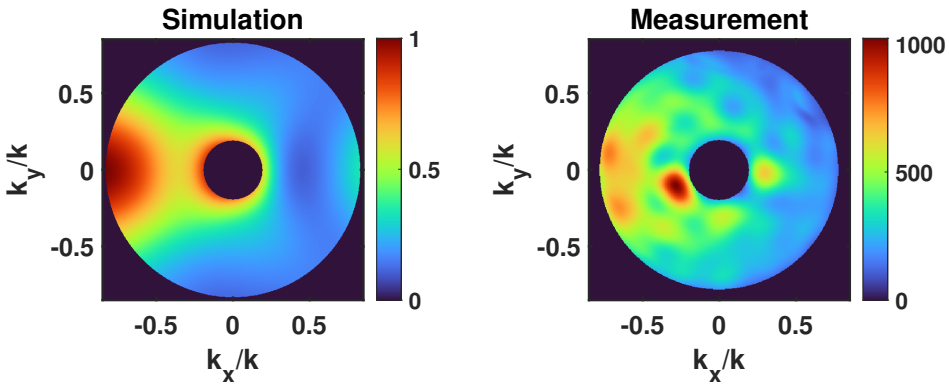
Finally, the FEM simulations assume a plane wave incident normal with respect to the substrate, instead of a focused spot. Therefore, we expect the scattered light to be more spread out, as each incident plane wave with an angle shifted from the normal adds a similar shift to the scattering pattern.

All things considered, we can conclude that the method of designing particles with a desired scattering behaviour in [Section 3.2](#) is qualitatively confirmed by these measurements. Directional scattering can indeed be achieved through the combination of two different materials into a single nanoparticle.



(a) Simulation symmetry axis of the particle along the x-axis, polarization of the incident light along the x-axis.

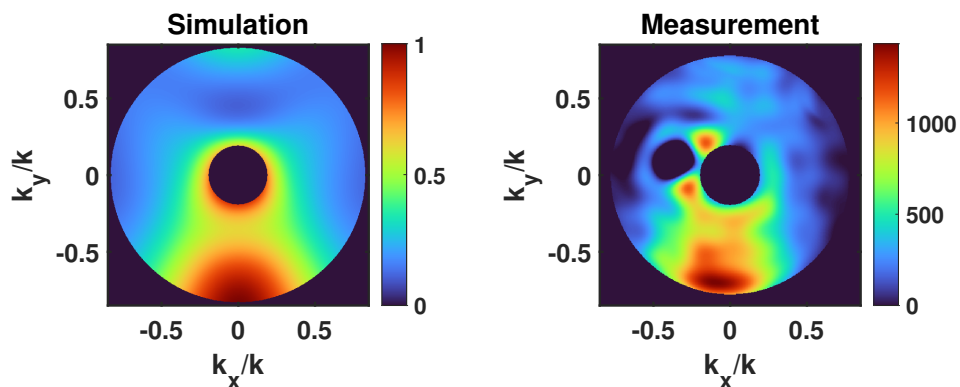
(b) Measurement symmetry axis of the particle along the x-axis, polarization of the incident light along the x-axis.



(c) Simulation symmetry axis of the particle along the x-axis, polarization of the incident light along the y-axis.

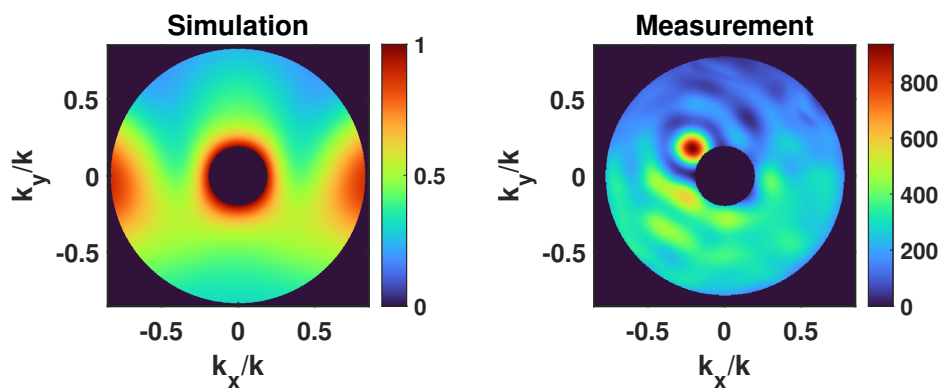
(d) Measurement symmetry axis of the particle along the x-axis, polarization of the incident light along the y-axis.

Figure 5.4: Simulations and corresponding measurements of SiO₂@Au core-semishell nanoparticles with the symmetry-axis parallel to the x-axis for different polarization of the incident light.



(a) Simulation symmetry axis of the particle along the y-axis, polarization of the incident light along the x-axis.

(b) Measurement symmetry axis of the particle along the y-axis, polarization of the incident light along the x-axis.



(c) Simulation symmetry axis of the particle along the y-axis, polarization of the incident light along the y-axis.

(d) Measurement symmetry axis of the particle along the y-axis, polarization of the incident light along the y-axis.

Figure 5.5: Simulations and corresponding measurements of SiO₂ @ Au core-semishell nanoparticles with the symmetry-axis parallel to the y-axis for different polarization of the incident light.

5.4. GRATING MEASUREMENT SETUP

To measure the diffraction efficiency of the produced gratings a goniometer was constructed. A schematic of the setup is shown in Figure 5.6. The goniometer allows for the measurement of the intensity of light which originates from the centre of the circle at different angles, while the lens rotating about the centre remains perpendicular to the incident light.

Light from a stabilized broadband Tungsten-Halogen source (Thorlabs SLS201/M 360 nm-2600 nm) was coupled to an optical fiber. This fiber was coupled to a collimator to illuminate the grating sample. After the fiber collimator a linear polarization filter and diaphragm was placed. This way, the direction of polarization and spot size on the grating could be controlled. The light is then collected using another fiber collimator. This collimator was mounted on a rotational stage, such that it could rotate around the sample and capture all the transmitted diffraction orders.

The sample was mounted on several stages: a linear stage to move along the z -direction, to make sure the sample is in the center of the circle of the collection collimator; a rotational stage such that the sample could be rotated around the y -axis, to change the angle of incidence of the light; and a rotational stage that could rotate the sample around the z -axis to make sure the diffraction order are aligned with the collection collimator. The grating was mounted with the grating lines parallel to the y -axis. Light from the collimator was sent to a spectrometer using a fiber, allowing us to calculate the diffraction efficiency.

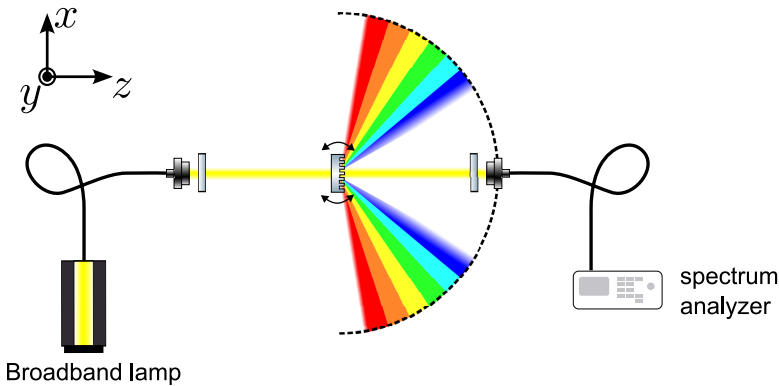


Figure 5.6: Schematic representation of the experimental setup used to analyse the performance of fabricated diffraction gratings.

5.5. GRATING MEASUREMENT RESULTS

To calculate the grating efficiency, first a spectral intensity reference measurement was taken of the light source by leaving the sample holder empty. The ratio between the intensity of the diffraction order and the intensity of the reference measurement then results in the grating efficiency. This means that Fresnel reflections of the first surface of the sample and absorption of the glass are also taken into account in the calculations of the grating efficiency.

5.5.1. POLARIZATION ALONG THE GRATING LINES

For the first set of measurements, the polarization of the incident light is along the grating lines. This means that for the measurements where the light is at an angle other than normal to the surface, the light is *s*-polarized (or TE). The gratings are made of fused silica with a pitch of 775 nm, a height of 520 nm and a linewidth of 260 nm.

To calibrate the setup and to check the performance of our fabricated gratings, measurement were done on samples after the reactive ion etching step (Section 4.2). Based on the results, improvements on the setup were made so that accurate and reliable measurements could be taken. These measurements also provide a benchmark for the composite gratings to improve upon.

In Figure 5.7, the measurements of the diffraction efficiency of the bare gratings are compared to the results of FEM simulations (see Appendix B for details). Note that these are not the same as Figure 3.33, since we changed from borosilicate glass to fused silica which has a lower refractive index. These measurements were taken with the light incident normal to the grating.

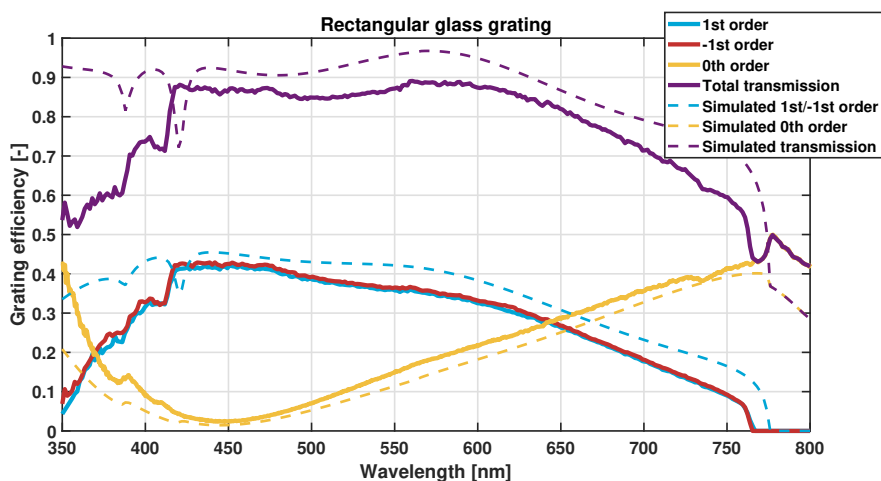


Figure 5.7: Measured grating efficiency of transmitted orders and total transmission of a fabricated rectangular grating made of fused silica with a pitch of 775 nm, a height of 520 nm and a width of 260 nm at normal incidence compared to simulations.

From the graph we see that the shape generally agrees. Also, as we would expect

from symmetry considerations, the 1st and -1st order nicely overlap. However, the 1st, -1st order and total transmission is lower than in the simulations. This can be explained by alignment errors in the setup, where not all the diffracted light is coupled into the optical fiber. Also, the fabricated grating is not exactly periodic and has some surface roughness resulting in losses due to diffuse scattering.

Furthermore, the measured 0th order is higher than in simulations. This is likely because the grating is not exactly rectangular. As discussed in [Chapter 4](#), the grating elements have a slight slope where the top of the elements is thinner than the bottom. As a result, the transmitted 0th order is not suppressed as efficiently as possible.

Finally, we can observe a drop in transmitted light below a wavelength of 420 nm. This cannot be explained by absorption by the glass, because we have used JGS-2 fused silica glass as the substrate which does not significantly absorb light above about 300 nm (which was also confirmed by measurements). Therefore, this is likely due to diffuse scattering due to the surface roughness of the gratings, which affects shorter wavelengths much more than longer wavelengths. The dip seen in the total transmission at around 760 nm, is due to shadowing of the sample holder where the diffracted light cannot reach the camera.

Adding a metal to the side of the elements, which turns it into a composite grating dramatically changes the diffraction efficiency. We will show the diffraction efficiency of several different metals that were used. The measurements of the composite gratings with gold added are shown in [Figure 5.8](#), for platinum in [Figure 5.9](#), for titanium in [Figure 5.10](#) and for silver in [Figure 5.11](#).

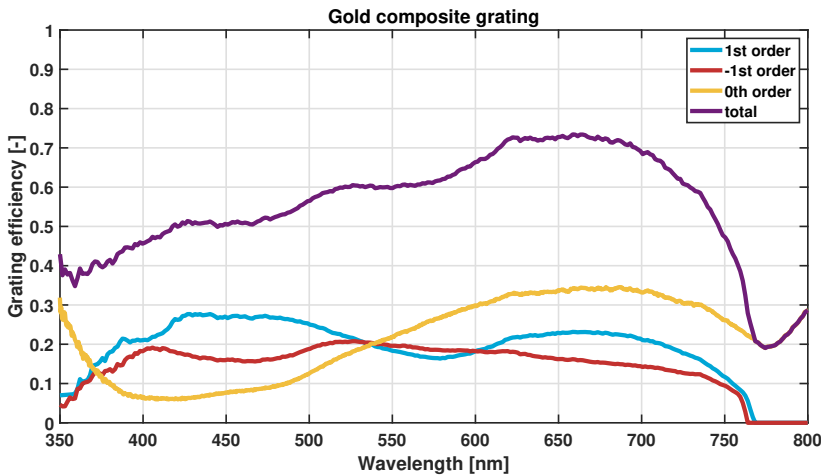


Figure 5.8: Measured grating efficiency of transmitted orders and total transmission of a fabricated composite grating with a pitch of 775 nm, a height of 520 nm and a width of 260 nm at normal incidence. A layer of 40 nm of gold was evaporated at an angle of 56 degrees on the side of the 1st diffraction order.

For the composite grating made with gold, we can see that the 1st and -1st order do indeed split, where more light is diffracted towards the side of the metal (the 1st diffraction order) as predicted by simulations in [Section 3.3](#). However, the overall

efficiency of the grating has significantly decreased, due to absorption and diffuse scattering. As discussed in Section 4.2, this is due to the geometry at the nanoscale of the deposited gold film.

Furthermore, between a wavelength of 530 nm and 605 nm, the efficiency of the -1^{st} order is actually higher than that of the 1^{st} order. It is unclear what the cause of this is, it could be that the permittivity for this bandwidth is such that the light is scattered slightly more to the glass side of the grating elements.

For composite gratings made out of platinum, titanium and silver, we see similar diffraction efficiencies. Over the entire visible spectrum, the diffraction efficiency of the 1^{st} and -1^{st} order split, where the 1^{st} order efficiency is higher than that of the -1^{st} order. Generally, the efficiency of the 1^{st} order is more than two times higher than that of the -1^{st} order.

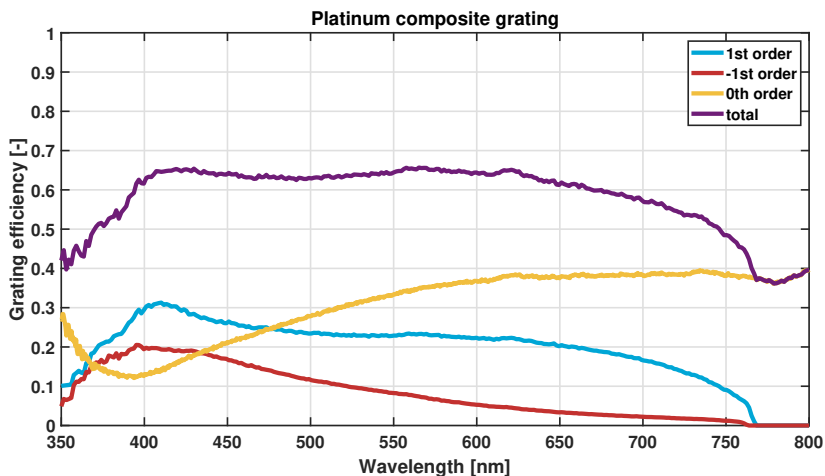


Figure 5.9: Measured grating efficiency of transmitted orders and total transmission of a fabricated composite grating with a pitch of 775 nm, a height of 520 nm and a width of 260 nm at normal incidence. A layer of 15 nm of platinum was evaporated at an angle of 60 degrees on the side of the 1^{st} diffraction order.

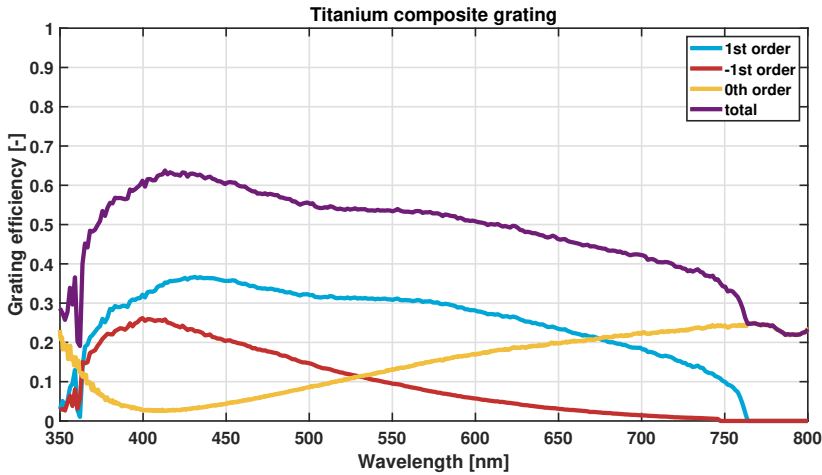


Figure 5.10: Measured grating efficiency of transmitted orders and total transmission of a fabricated composite grating with a pitch of 775 nm, a height of 520 nm and a width of 260 nm at normal incidence. A layer of 15 nm of titanium was evaporated at an angle of 60 degrees on the side of the 1st diffraction order.

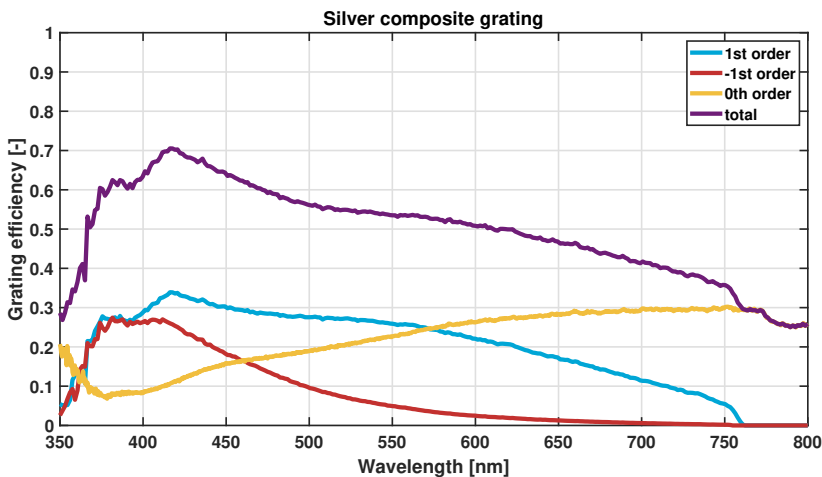


Figure 5.11: Measured grating efficiency of transmitted orders and total transmission of a fabricated composite grating with a pitch of 775 nm, a height of 520 nm and a width of 260 nm at normal incidence. A layer of 15 nm of silver was evaporated at an angle of 55 degrees on the side of the 1st diffraction order.

Furthermore, a shift can be seen in the minimum of the 0th diffraction order and the minimum value changes. Due to the addition of the metal, the light that is transmitted in between the grating lines cannot fully destructively interfere with the light that is scattered into the 0th order by the grating lines. The minimum shifts due to the addition of the metals; the optical path length reduces, because the real part of the refractive index of the used metals is smaller than that of air.

Differences in the shape of the efficiency curves can be explained by the differences in the wavelength dependency of the permittivity of the used metals. Of course, the overall efficiency of the gratings is still decreased due to absorption and diffuse scattering.

To try and solve the problem of absorption and diffuse scattering, samples were annealed inside a nitrogen environment at 400°C. As we have previously discussed in Section 4.2, this has been shown to work in the literature[75–77]. For most of the metals used, we found no improvement of the grating efficiency or the overall transmission of the samples, with the exception of the sample with silver and titanium.

This is because for silver, small islands are created due to the annealing process which can clearly be seen in Figure 4.17. Due to the formation of these islands, absorption and diffuse scattering is actually increased rather than decreased as shown in Figure 5.12. It is interesting to note that this method is also used for the creation of plasmonic nanoparticles[71].

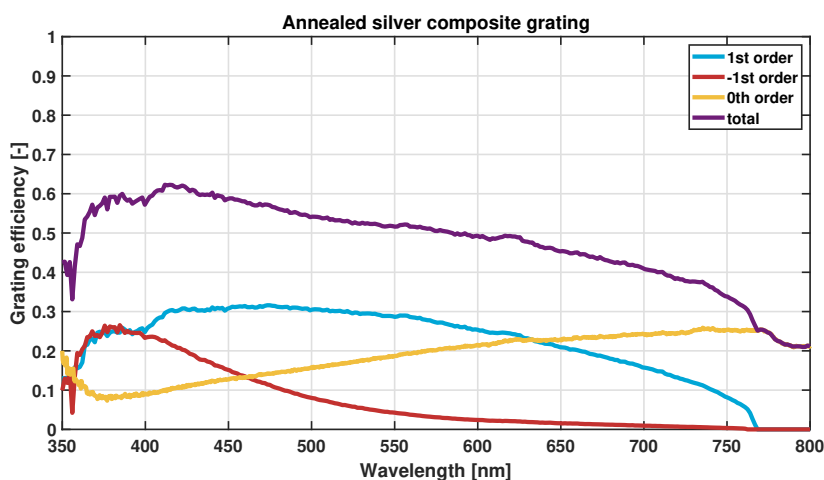


Figure 5.12: Measured grating efficiency of transmitted orders and total transmission of a fabricated composite grating with a pitch of 775 nm, a height of 520 nm and a width of 260 nm at normal incidence. A layer of 15 nm of silver was evaporated at an angle of 55 degrees on the side of the 1st diffraction order. Afterwards, the grating was annealed at 400°C for 4 hours.

For the titanium samples, annealing did not only change the geometry of the film, but changed the material into titaniumnitride through the chemical reaction of the nitrogen gas in which the annealing took place[76]. The measured grating efficiencies are shown in Figure 5.13.

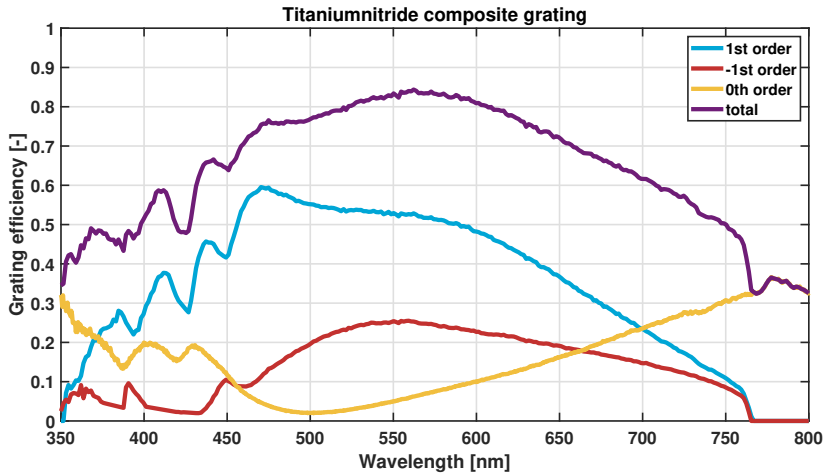


Figure 5.13: Measured grating efficiency of transmitted orders and total transmission of a fabricated composite grating with a pitch of 775 nm, a height of 520 nm and a width of 260 nm at normal incidence. A layer of 15 nm of titanium was evaporated at an angle of 60 degrees on the side of the 1st diffraction order. Afterwards, the grating was annealed at 400°C for 4 hours to create titaniumnitride.

As a result of the annealing, the absorption and diffuse scattering is significantly reduced while the directional scattering by the grating elements is maintained as is evident from the high 1st order grating efficiency. The efficiency of the 1st order reaches values higher than 50% from about 460 nm to 590 nm. Such a high efficiency cannot be achieved by gratings which are symmetric with respect to the polarization (and are made of isotropic materials), as the 1st and -1st order must have the same efficiency in that case.

Note that the minimum of the 0th order has shifted towards 500 nm. This shows that the optical pathlength has increased with respect to the titanium sample, but also with respect to the bare glass grating. Therefore, a material must now be present with a refractive index larger than that of air. This is further proof that TiN was created in the annealing process, which for optical frequencies, has a refractive index where the real part is around 1.2.

Up to a wavelength of about 500 nm, some oscillations can be seen in the diffraction efficiency of all transmission orders. We are currently unsure where these oscillations come from, and this is out of the scope of this thesis.

The performance of the bare glass grating and the composite grating with titaniumnitride are compared in Figure 5.14. We can see that up to a wavelength of 425 nm, the performance of both grating is about equal, with some dips in the efficiency of the composite grating. However, from 450 nm onwards the composite grating significantly outperforms the bare grating.

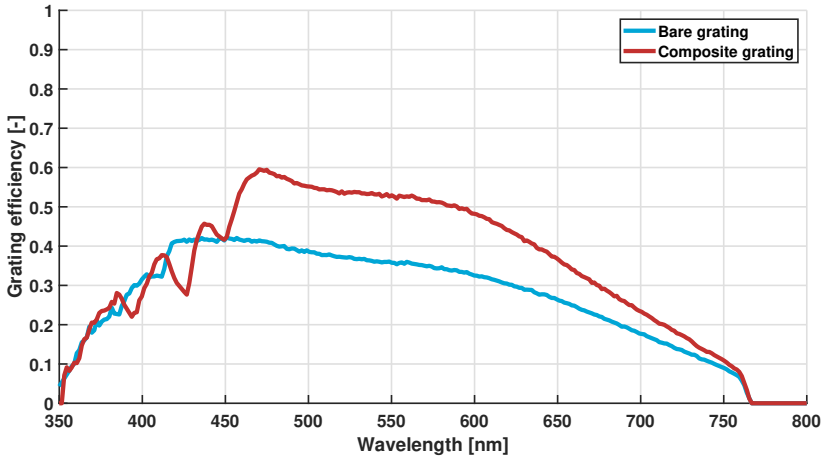


Figure 5.14: Comparison of the 1st diffraction order efficiency of the bare glass grating and composite grating with titanium nitride. Both gratings are illuminated at normal incidence.

5

While the results of the composite gratings with a metal showed that the theory of using grating elements which directionally scatter for the entire visible spectrum works, this result shows that the problem of diffuse scattering and absorption can be overcome. This means that composite gratings have a potential of outperforming commercial gratings, while maintaining competitive in their fabrication process.

LIGHT INCIDENT AT AN ANGLE

Next, the same measurements were made where the grating was rotated to the optimal angle; the angle at which most energy would go into a single diffraction order for the full visible spectrum. These angles were found experimentally by measuring the gratings at angles ranging from 5 to 15 degrees from the normal. This was done for the bare glass grating, the composite grating with platinum and the composite grating with titaniumnitride. Note that we do not take into account the 2nd transmission orders here, as a result the total transmission is likely higher than shown.

The optimal angle for the bare grating and the grating with platinum is 14 degrees, while for the grating with titaniumnitride the optimal angle is 12 degrees. The results are shown in [Figure 5.15](#), [Figure 5.16](#) and [Figure 5.17](#).

5

Comparing the first order diffraction efficiency of the normal grating and the composite grating at an angle, we see that the composite grating also has an increased efficiency, as shown in [Figure 5.18](#).

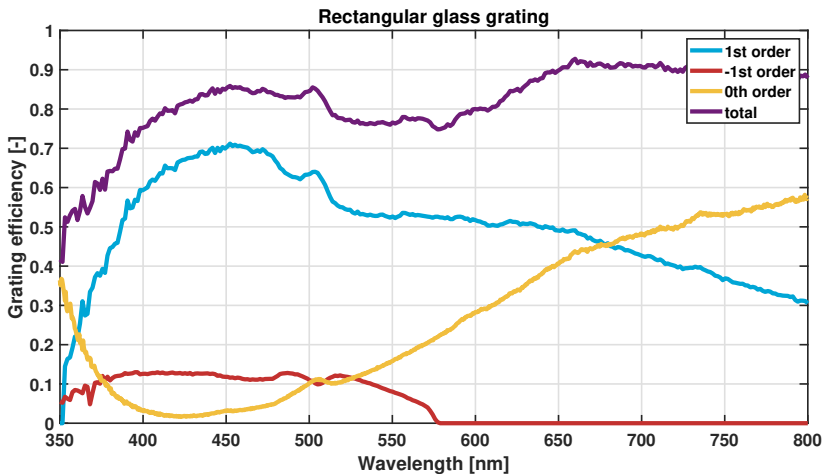


Figure 5.15: Measured grating efficiency of transmitted orders up to the 1st / -1st order and total transmission of a fabricated glass grating with a pitch of 775 nm, a height of 520 nm and a width of 260 nm at an incidence angle of 14 degrees.

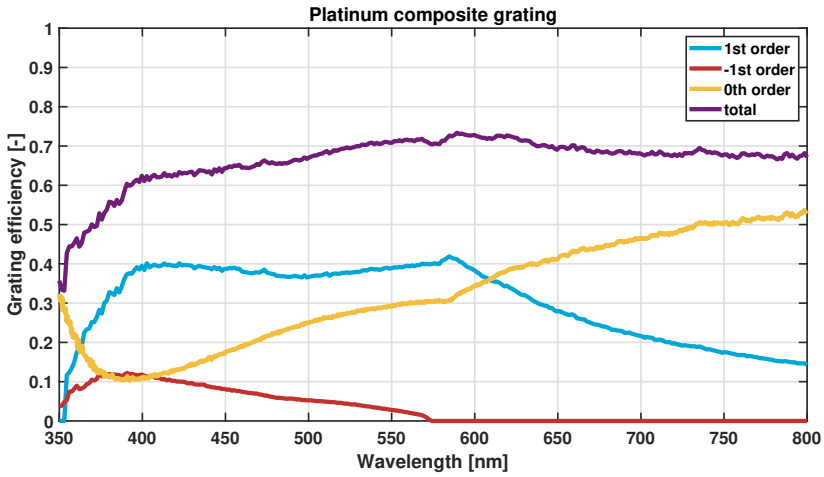


Figure 5.16: Measured grating efficiency of transmitted orders up to the 1st/-1st order and total transmission of a fabricated composite grating with a pitch of 775 nm, a height of 520 nm and a width of 260 nm at an incidence angle of 14 degrees. A layer of 15 nm of platinum was evaporated at an angle of 60 degrees on the side of the 1st diffraction order.

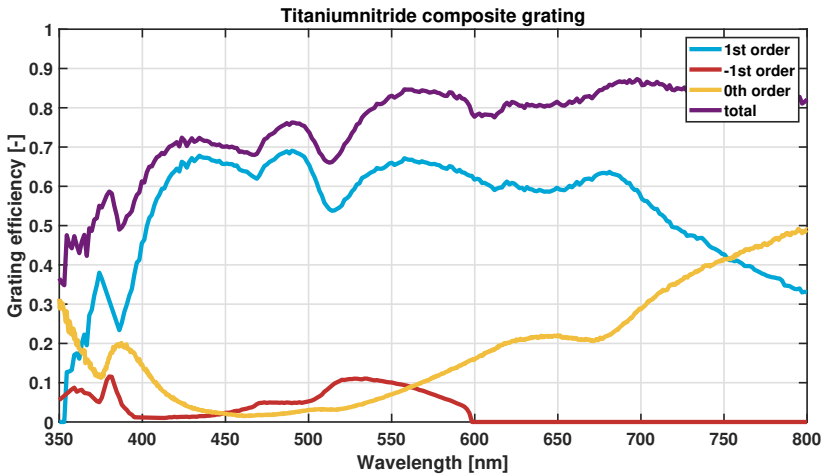


Figure 5.17: Measured grating efficiency of transmitted orders up to the 1st/-1st order and total transmission of a fabricated composite grating with a pitch of 775 nm, a height of 520 nm and a width of 260 nm at an incidence angle of 12 degrees. A layer of 15 nm of titanium was evaporated at an angle of 60 degrees on the side of the 1st diffraction order. Afterwards, the grating was annealed at 400°C for 4 hours to create titaniumnitride.

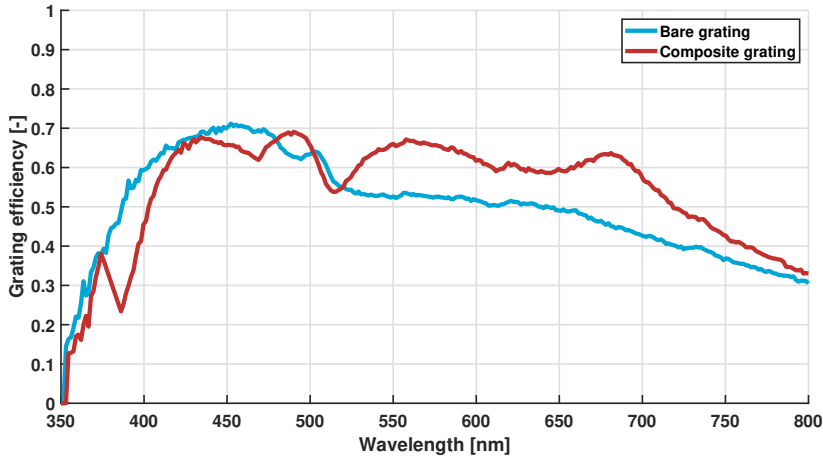


Figure 5.18: Comparison of the 1st diffraction order efficiency of the bare glass grating and composite grating with titaniumnitride. Both gratings are illuminated at an incident angle of 14 degrees from normal.

We can see that for wavelengths below 425 nm, the composite grating performs worse than the bare glass grating. This is likely due to the absorption and diffuse scattering as we have discussed before. In the bandwidth from 425 nm up to 520 nm, the efficiency of both gratings are about the same. Beyond that, the composite grating outperforms the bare grating, at some points the efficiency is increased by over 15%.

It is likely that improvements in the fabrication of these gratings, both the efficiency of the bare grating and composite titaniumnitride grating can be improved. For the composite grating, we see that a lot of light is lost due to absorption and diffuse scattering, especially in the blue part of the spectrum. Further improvements can be achieved here as well, for example by substituting the titaniumnitride for a different semiconductor material.

Finally, the composite gratings were designed to function at normal incidence. Thus, it makes sense that the improvement at a different angle is limited. The optimal amount of titaniumnitride that is present and the optimal angle at which the titanium it is made from is deposited is likely different for illumination at an angle.

5.5.2. POLARIZATION PERPENDICULAR TO THE GRATING LINES

So far we have only discussed the case where light is polarized along the grating (*s*-polarized or TE). If the polarization is *p*-polarized, where the electric field is perpendicular to the grating lines, we would still expect some asymmetric scattering. It is likely that the asymmetry is much less, similar to what we have seen for the individual nanoparticles in Section 5.3 (Figure 5.4a, Figure 5.4b, Figure 5.5c and Figure 5.5d).

As before, we start by measuring the grating without any other material added. The results are shown in Figure 5.19.

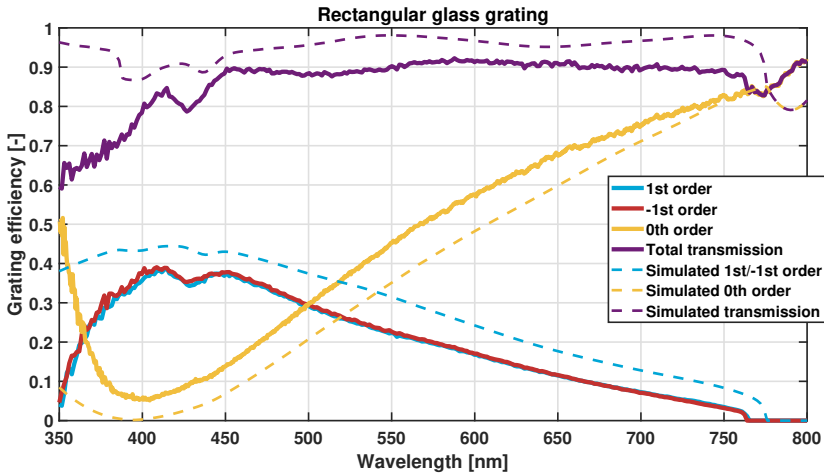


Figure 5.19: Measured grating efficiency of transmitted orders and total transmission of a fabricated rectangular grating made of fused silica with a pitch of 775 nm, a height of 520 nm and a width of 260 nm at normal incidence compared to simulations for *p*-polarized incident light.

As expected, the efficiency of the 1st and -1st diffraction orders are exactly equal. Comparing this to the results for the *s*-polarization in Figure 5.7, we see that the diffraction efficiency is lower overall, because the grating was not optimized for *p*-polarization.

The simulations of the grating show again show a similar shape. The lower 1st and -1st diffraction efficiency in the measurements and increased 0th order efficiency are likely caused by the same phenomena as for the measurements with *s*-polarized light (alignment, grating geometry and surface roughness).

A dip in the 1st and -1st order and the total transmission can be seen around 425 nm, which is caused by an increase of 1st and -1st reflection orders.

Next, we will consider a composite grating made with TiN, which showed a great increase of efficiency for the 1st diffraction order in the case of *s*-polarization. The measurements for *p*-polarization are shown in Figure 5.20.

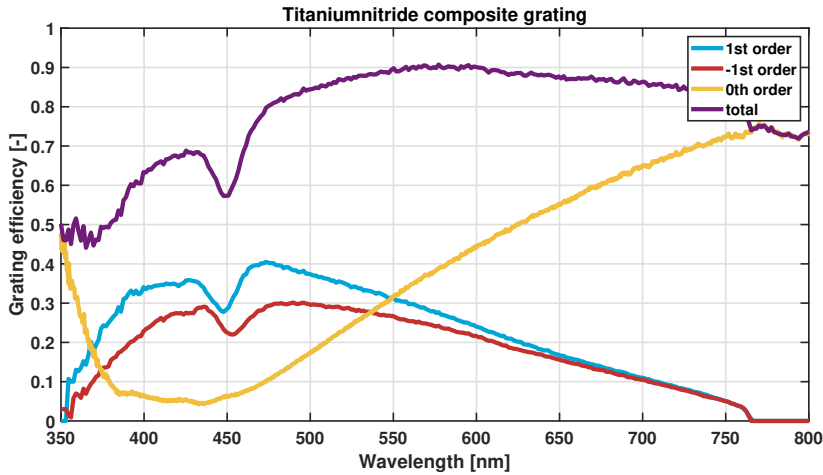


Figure 5.20: Measured grating efficiency of transmitted orders and total transmission of a fabricated composite grating with a pitch of 775 nm, a height of 520 nm and a width of 260 nm at normal incidence. A layer of 15 nm of titanium was evaporated at an angle of 60 degrees on the side of the 1st diffraction order for *p*-polarized incident light. Afterwards, the grating was annealed at 400°C for 4 hours to create titaniumnitride.

5

As hypothesized, the splitting of the 1st and -1st is not as significant as for the case where the polarization of the incident light is along the grating lines. However, the efficiency of the 1st order is reduced with respect to the efficiency measured for the bare grating. We can see that the total amount of light that is transmitted is significantly reduced for the lower wavelengths up to 500 nm. Which is again likely due to the roughness of the fabricated grating elements resulting in diffuse scattering.

A dip in the total transmission and the 1st and -1st order can also be seen around a wavelength of 450 nm. This is likely the same dip as we have seen in [Figure 5.19](#), which has shifted to longer wavelengths due to the addition of material.

5.6. SUMMARY AND OUTLOOK

From the measurements of the single nanoparticles, we can conclude that the theory for directional scattering through the combination of two materials into a single nanoparticle is validated. The measurements clearly show the directional scattering that was predicted by simulations and the obtained images in the back focal plane are qualitatively similar to the simulated images.

Directional scattering is strongest when the polarization of the incident light is along the symmetry axis of the particle. In the case that the polarization is perpendicular to the symmetry axis of the particle, limited directional scattering is observed.

Doing measurements of single scattering nanoparticles is difficult because of the low amount of signal due to the small size of the particles and the very small amount of light scattered by them compared to the background signal from the scattering by optical components in the system. Using Fourier filtering to clean up the interference effects, a clear image of the scattering can still be produced.

Measurements of the fabricated composite gratings (both the metal and semiconductor samples) show that the developed theory works in the broadband for the entire visible spectrum. Furthermore, the diffraction gratings themselves demonstrate a potential application for broadband directionally scattering nanostructures.

The composite grating with titaniumnitride show a clear improvement over the standard glass gratings, both at normal incidence and at an angle where the diffraction efficiency for the 1st diffraction order is optimized. As expected, the improvement is found for *s*-polarized light. For *p*-polarized light, splitting of the 1st and -1st diffraction orders is still observed. However, in both cases diffuse scattering and absorption limit the overall efficiency.

For relatively simple fabrication steps, a significant improvement in the diffraction efficiency can be achieved. By optimizing the fabrication process, possibly using a different semiconductor material and optimization of the grating geometry, we think that the efficiency can be improved even further. Possibly becoming a good alternative for transmission gratings for *s*-polarized light.

More experiments could be done to determine where the loss of total transmission is coming from. A more detailed analysis of the gratings can be made by measuring the reflected diffraction orders and by measuring the absorption using an integrating sphere. Combining this with our developed theory for scattering composite nanostructures, an effective method for the optimization of the diffraction efficiency can be established.

6

VOLUMETRIC SCATTERING BY NANOPARTICLES

“

If your theory is found to be against the Second Law of Thermodynamics I can give you no hope; there is nothing for it but to collapse in the deepest humiliation.

Arthur Stanley Eddington[9]”

MOST of this thesis is focused on the scattering by isolated nanoparticles. In this chapter we will look at the collective scattering by nanoparticles. So instead of the single scattering regime, we will consider the multiple scattering regime.

First, we will look at the limitation of multiple scattering on maintaining directionality by taking into account the second law of thermodynamics in [Section 6.1](#). Then, simulations are performed using a Monte-Carlo approach, the model is described in [Section 6.2](#) and the results are presented in [Section 6.3](#). Finally, a conclusion and outlook is given for multiple scattering by designed nanoparticles.

6.1. SCATTERING AND ENTROPY

The second law of thermodynamics is generally understood as that entropy always increases. We will show that in optics, we can translate this into the equivalent statement that étendue always increases. In this section, we will follow the explanation from the book *Introduction to non-imaging optics* by Chaves[78].

We start by introducing the concept of radiance. We consider an area dA that emits or scatters light with a certain flux $d\Phi$ as shown in Figure 6.1. The light is emitted (or scattered) at an angle θ from the normal vector \mathbf{n} of dA and is confined in a solid angle $d\Omega$. The radiance L is then defined by

$$L = \frac{d\Phi}{\cos\theta dA d\Omega}. \quad (6.1)$$

A more commonly known quantity closely related to the radiance is called the intensity, given by

$$I = \frac{d\Phi}{d\Omega}. \quad (6.2)$$

If the surface dA is inside a medium with refractive index n , we can write the radiant flux as

$$d\Phi = \frac{L}{n^2} n^2 \cos\theta dA d\Omega = L^* dU \quad (6.3)$$

Here, $L^* = L/n^2$ is defined as the basic radiance. The étendue is defined by

$$dU = n^2 \cos\theta dA d\Omega. \quad (6.4)$$

The étendue is a quantity that depends on the spatial and angular extend of the light and is independent of the energy of the light.

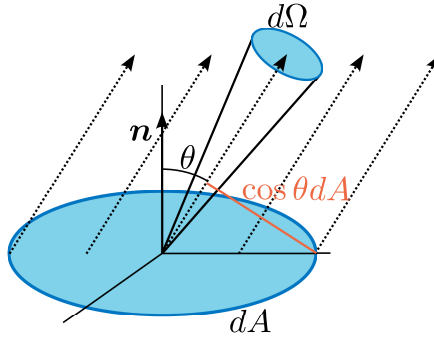


Figure 6.1: Graphical representation of the concept of radiance. Light is incident or emitted by the surface dA at an angle θ from the normal vector of the surface \mathbf{n} in a solid angle Ω .

Now, let us assume that the surface dA is the surface of a blackbody emitter. The total flux emitted into a hemisphere is given by the Stefan-Boltzmann law:

$$d\Phi_{\text{hem}} = n^2 \sigma_{\text{SB}} T^4 dA, \quad (6.5)$$

with σ_{SB} the Stephan-Boltzmann constant ($5.670 \cdot 10^8 \text{ W}\cdot\text{m}^{-2}\cdot\text{K}^{-4}$) and T the temperature of the black body emitter (in Kelvin). If we calculate the light emission of an arbitrary emitter over a hemisphere, we get

$$d\Phi_{\text{hem}} = L^* n^2 dA \int_0^{2\pi} \int_0^{\pi/2} \cos\theta \sin\theta d\theta d\phi = \pi n^2 L^* dA \quad (6.6)$$

Using the two equations above, we can relate the basic radiance to the temperature:

$$L^* = \frac{\sigma_{\text{SB}} T^4}{\pi} \quad (6.7)$$

Let us consider the situation where two black body surfaces separated by a distance r are radiating towards each other as shown in [Figure 6.2](#). We can then calculate the étendue of the light that surface dA_1 emits towards surface dA_2 :

$$dU_{12} = n^2 dA_1 \cos\theta_1 d\Omega_{12} = n^2 dA_1 \cos\theta_1 \frac{dA_2 \cos\theta_2}{r^2}. \quad (6.8)$$

Similarly, we can calculate the étendue of the light emitted by surface dA_2 towards surface dA_1 :

$$dU_{21} = n^2 dA_2 \cos\theta_2 d\Omega_{21} = n^2 dA_2 \cos\theta_2 \frac{dA_1 \cos\theta_1}{r^2}. \quad (6.9)$$

From this, we can see that

$$dU_{12} = dU_{21}. \quad (6.10)$$

If we now assume that the system is in equilibrium (the surfaces emit the same amount of light), then the flux from surface 1 to 2 is equal to the flux from 2 to 1: $d\Phi_{12} = d\Phi_{21}$. Combining this with [Equation 6.1](#) and [Equation 6.10](#), we get:

$$L_1^* = L_2^*. \quad (6.11)$$

From [Equation 6.7](#), we see that this means that the temperature of the two surfaces are equal. This is of course what we would expect from thermodynamics.

Going back to the statement at the start of the chapter, the question is whether we can use some piece of optics that could decrease the étendue. In this case, the light emitted by dA_1 is captured by the first surface of the optic dO_1 . After crossing the optic, the light is emitted at the last surface dO_2 and is then directed towards the surface dA_2 . Following the same arguments as before, we know that in equilibrium we have

$$L_1^* = L_{O1}^*, \quad L_{O2}^* = L_2^*. \quad (6.12)$$

For light travelling from dA_1 to dA_2 it is possible for the basic radiance to decrease due to the optic (because of absorption), such that we have $L_{O1}^* > L_{O2}^*$. Then $T_1 > T_2$, which would not violate the principles of thermodynamics. However, the basic radiance cannot increase due to the optic.

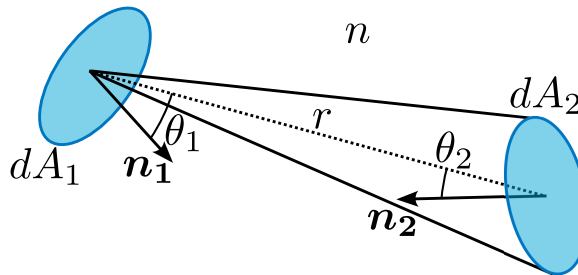


Figure 6.2: Graphical representation of two surfaces dA_i radiating towards each other and absorbing the radiation. The surfaces are a distance r from each other and are in a medium with refractive index n . The normal vectors \mathbf{n}_i and related angles θ_i are also drawn.

Furthermore, for constant flux, from Equation 6.1 we see that the only way of decreasing the étendue by going through the optic is by increasing the basic radiance, which we just showed is not possible. So, for constant flux, étendue can only be conserved or increased¹. If we would want to decrease the étendue, the only way would be by reducing the flux. In other words, by introducing absorption in the optical system[79]. However, this is unwanted in many applications.

Let us now consider the consequences this has on everything that has been discussed in this thesis. Would it be possible for us to design a nanoparticle that (even ever so slightly) redirects light towards a particular direction, independent of the direction of the incident light? If this would be possible, we would be able to make a volume of many of these nanoparticles that redirects this light into that direction for a macroscopic effect. This would reduce the étendue, and therefore is not possible.

More specifically, down to the single nanoparticle level, we could consider a spherical wave incident on a nanoparticle. This means that the étendue of the incident light is at its maximum. Therefore, any increase in directivity is not possible, the only possible result is that an outgoing spherical wave is produced.

Let us lower our expectations, instead of lowering the étendue, we can try to change the direction of the light by going through a volume with nanoparticles. As we have seen in Chapter 3, when light scatters from a nanoparticle, the étendue increases significantly. At the same time, we need enough nanoparticles such that most of the light that we put into the volume, will interact with the nanoparticles.

This creates a problem; if we have enough nanoparticles to make sure that the light sufficiently interacts with the nanoparticles, we will have nearly reached maximum étendue of the light after interacting with the nanoparticles. At that point, light is scattered uniformly in each direction and we could have used any arbitrary nanoparticle. If, on the other hand, we use a small amount of nanoparticles, most of the light will simply go on with hardly any scattering. The challenge then, is to find the right balance.

¹Alternative derivations to get to the conservation are also presented by Chaves[78], including a derivation from Hamiltonian optics. In this case, the conservation of étendue shows up in the form of Liouville's theorem.

6.2. MONTE-CARLO SIMULATIONS

To determine what would happen to light incident on a volume with nanoparticles, we have developed a python code to run Monte-Carlo simulations². The idea is to launch *photons* one by one into the volume. The scatter patterns from the COMSOL simulations are then used as a probability distribution and by generating a random number, the scatter direction is determined. By launching many photons, the scattering of light through the volume can be approximated.

We start by defining a *volume* and a source in 2D³, which has a defined position of where the light enters the volume and a defined angular distribution (Figure 6.3). In the volume, a certain density of scatterers exist. Depending on the density of the scatterers, a mean free path length \mathcal{L} can be calculated. Using the mean free path length, a probabilistic distance can be calculated after which a photon will encounter a scatterer.

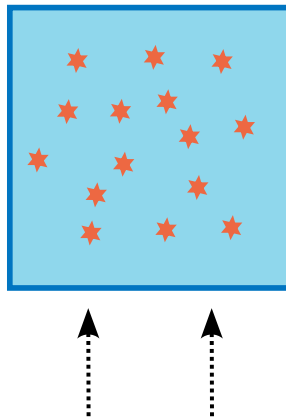


Figure 6.3: Schematic representation of the setup for the Monte Carlo simulations. Light enters the box from the bottom and is scattered by the scatterers. When the light exits the box, the position and angle at which it does is recorded.

The free path length is calculated using

$$\mathcal{L} = \frac{1}{\rho\sigma_{\text{ext}}}, \quad (6.13)$$

with σ_{ext} the extinction cross section (in m), and ρ density of scatters (in m^{-2}). By using a random number $\zeta \in [0, 1]$, we can calculate the random distance a photon can travel until it is scattered through

$$\Delta S = -\mathcal{L} \ln(\zeta). \quad (6.14)$$

After this distance is travelled, the photon will either be scattered and will obtain a new direction into which it will travel, or it will be absorbed. To determine what happens,

²A large part of this work was done by P. Van der Spek and E. Yildirim as part of their bachelor and master thesis[80, 81].

³The scattering in 3D was also investigated and we found that the results were qualitatively the same. Since they are easier understood in 2D, these are presented here.

the ratio between the scattering cross section and extinction cross section is used. This ratio is called the albedo:

$$A = \frac{\sigma_{\text{sc}}}{\sigma_{\text{ext}}}. \quad (6.15)$$

If the photon is scattered, its new direction can be determined through the normalized intensity scatter pattern, which can be determined for a certain scatterer using the methods from [Chapter 2](#).

Depending on the number of particles and their scattering cross section, the photons will scatter a certain number of times until they are either absorbed, or leave the volume. When they leave the volume, their position and direction is recorded. The entire process of the Monte-Carlo simulation is outlined in the diagram of [Figure 6.4](#).

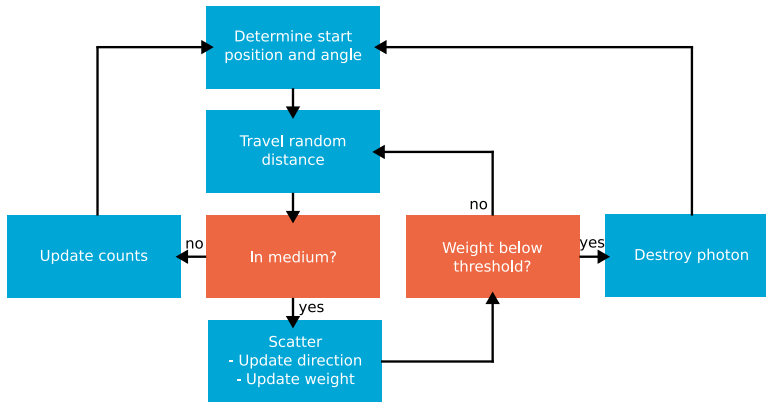


Figure 6.4: Schematic representation of the algorithm used for the Monte Carlo simulations.

6.3. MONTE-CARLO RESULTS

The goal of this PhD project as mentioned in [Chapter 1](#), is to create a volume with a desired scattering behaviour. To see if we can attain this goal, we will analyse the intensity distribution and angular distribution of the light transmitted through a volume with nanoparticles.

The results of all sides is plotted in a single graph, so that they are easy to compare. In [Figure 6.5](#), the results are plotted alongside the box, to help with the interpretation of the results. For the top and bottom distributions, the graphs run from the left of the box to the right of the box. For the left and right distributions, the graph runs from the bottom of the box to the top of the box.

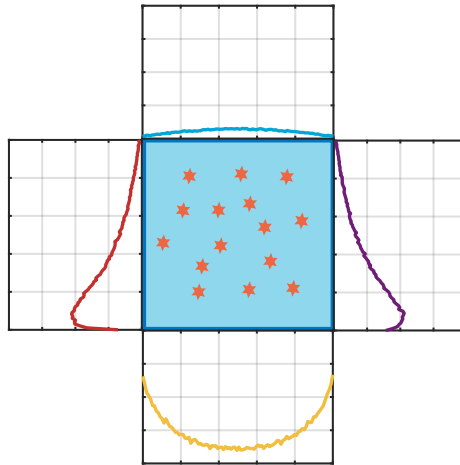


Figure 6.5: Example of the intensity distribution plots placed to the side of the box with scatterers to help with the interpretation of the results in the following subsections.

6.3.1. UNIFORM SCATTERERS

To get a sense of how the light is scattered by nanoparticles, we will first consider particles which only have an electric dipole contribution. As a result, in the plane perpendicular to the polarization of the incident light, the scattering is fully isotropic. Next, we send a parallel beam of light into the box with the particles and plot the resulting intensity distribution at the edges. This is a good reference to compare the other simulations to, as there is no absorption and no preferred direction.

To demonstrate the effect of the density of particles, the simulation is done for three different cases where the density of scatterers is increased. The scattering cross section is not changed. In the figure below we mention the mean path lengths, as this makes interpretation of the results the easiest. We plot both the intensity distribution at the four edges of the box and the angular distribution.

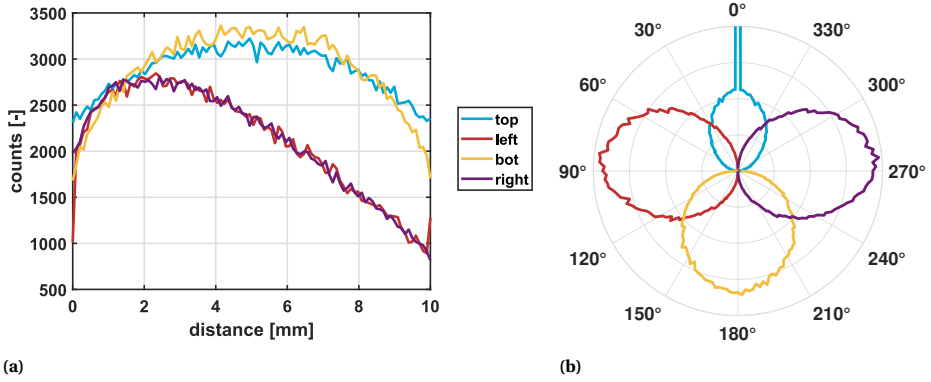


Figure 6.6: Intensity over (a) position and angle (normalized) (b) for 10x10 mm box with particles which scatter the light uniformly, for different sides of the box. The mean free path of photons travelling through the box is 5 mm.

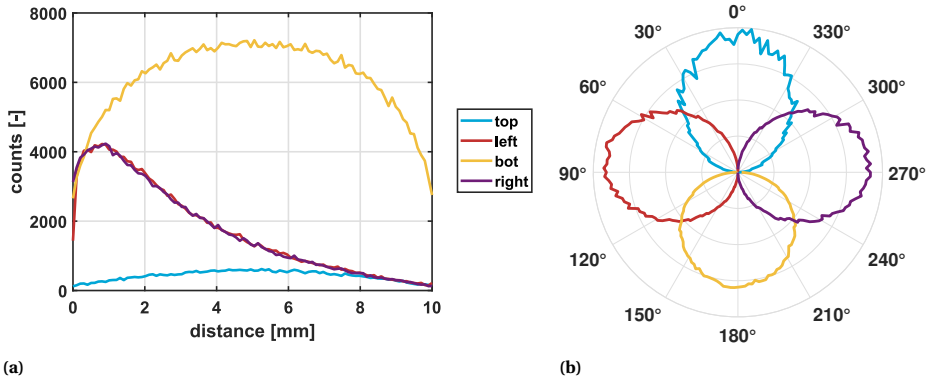


Figure 6.7: Intensity over position (a) and angle (normalized) (b) for 10x10 mm box with particles which scatter the light uniformly, for different sides of the box. The mean free path of photons travelling through the box is 1 mm.

Figure 6.6 shows the results for the longest mean free path length of the three cases shown. The path length is about 5 mm, which means that each photon scatters twice on average. The result is that the amount of light scattered to the top of the volume is about equal to the amount of light scattered to the bottom. From the angular distribution of the light passing through the volume, we see that a large part of the light that has reached the top side has not scattered at all.

Looking at the intensity distribution of the sides of the volume, we see that the intensity first increases as we move up and then decreases. The initial increase follows the same pattern as the curves for the top and bottom intensity and is due to the edges of the volume. The decrease follows the Beer-Lambert law, as we move up further in the volume, more and more of the light has scattered, resulting in an exponential decrease

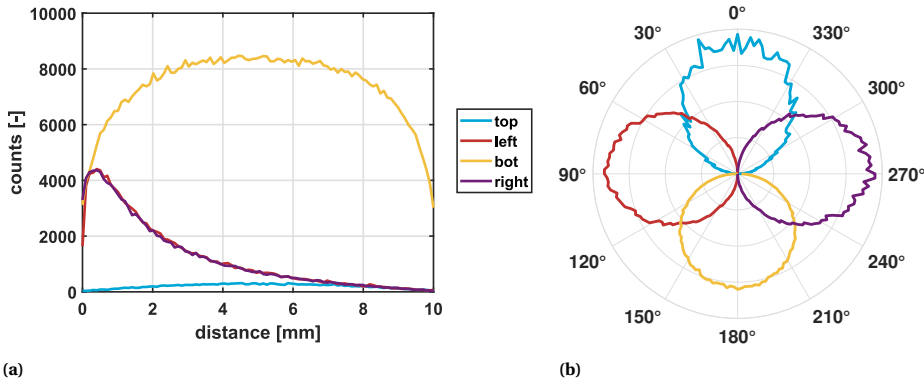


Figure 6.8: Intensity over position (a) and angle (normalized) (b) for 10x10 mm box with particles which scatter the light uniformly, for different sides of the box. The mean free path of photons travelling through the box is 0.5 mm.

of the intensity. This exponential relation is more clear in [Figure 6.7](#) and [Figure 6.8](#).

The effect of increasing the density of scatterers and thus decreasing the mean free path length can be seen in [Figure 6.7](#) and [Figure 6.8](#). Less and less light reaches the top of the volume due to the exponential decay. The angular distribution of the light at the top of the volume is now consistent with the scatter pattern of a single particle, however the amount of light reaching the top is very small.

The conclusions we can draw from this simple case are then as follows:

- the scatter pattern of a single nanoparticle must have very little backscattering so that not a lot of light is lost to the bottom of the volume in the first scatter event.
- the density of scatterers must be high enough so that the angular distribution of the light leaving the volume is fully determined by the nanoparticles. In other words, the non-scattered light does not significantly contribute to the intensity at the edges of the volume.

6.3.2. DIRECTIONAL SCATTERERS

Next, we will consider a volume with particles that preferably scatter into a certain direction, with limited backscattering. Specifically, we will use a particle similar to those we have introduced in [Chapter 3](#). In this case, it is a core-semishell particle with $\epsilon_{\text{core}} = 1$, $\epsilon_{\text{shell}} = 4$ inside a medium with $\epsilon_{\text{med}} = 2$. The core radius is 150 nm and shell thickness is 40 nm, the scatter pattern for $\lambda_0 = 500$ nm is shown in [Figure 6.9](#). The scatter pattern was calculated using COMSOL (for details, see [Appendix B](#)).

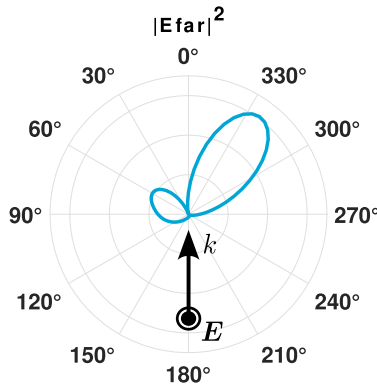


Figure 6.9: Polar plot of the scatter intensity by a core-semishell nanoparticle with a core radius of 150 nm, shell thickness of 40 nm, $\epsilon_{\text{core}} = 1$, $\epsilon_{\text{shell}} = 4$ inside a medium with $\epsilon_{\text{med}} = 2$ for an incident plane wave at a wavelength of 500 nm.

We take a density of these particles such that the mean free path lengths are the same as for the case of the uniform scatterer. The intensity distribution is shown in [Figure 6.10](#). From this graph, we observe that more light has scattered towards the left side of the volume than the right side. Moreover, the intensity distribution on the top of the volume shows more light on the right. Also, less light is scattered back to the bottom of the box due to the scattering pattern.

From the peak at 0° in the angular distribution, we see that it is dominated by the part of the light which has not been scattered. Besides the peak, we can recognise the scattering pattern for a single particle in the distribution. For the side, we do see that the angular distribution is significantly different from the case of the uniform scatterer due to the directional scattering.

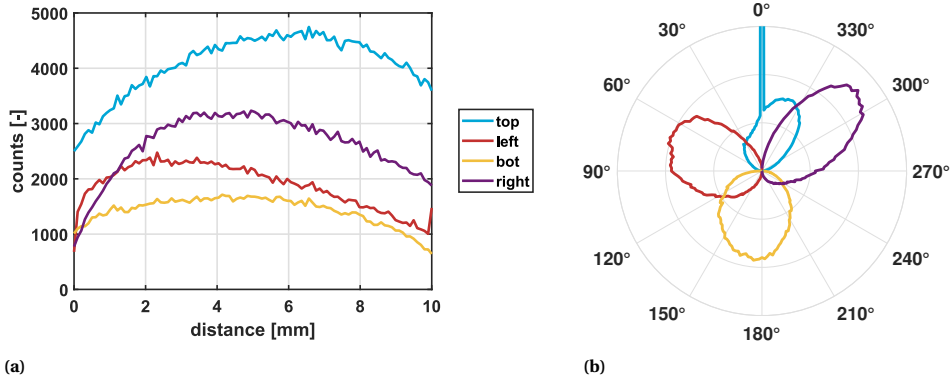


Figure 6.10: Intensity over position (a) and angle (normalized) (b) for 10x10 mm box with lossless directional scatterers, for different sides of the box. The mean free path of photons travelling through the box is 5 mm.

Decreasing the mean free path length again, Figure 6.11 shows that the amount of backscattered light significantly increases, consistent with the case of the uniform scatterer. Because there are now more scatter events on average, the étendue increases and directionality is lost. We do see that the angular distribution of the light transmitted through the top is fully determined by the scattered light now.

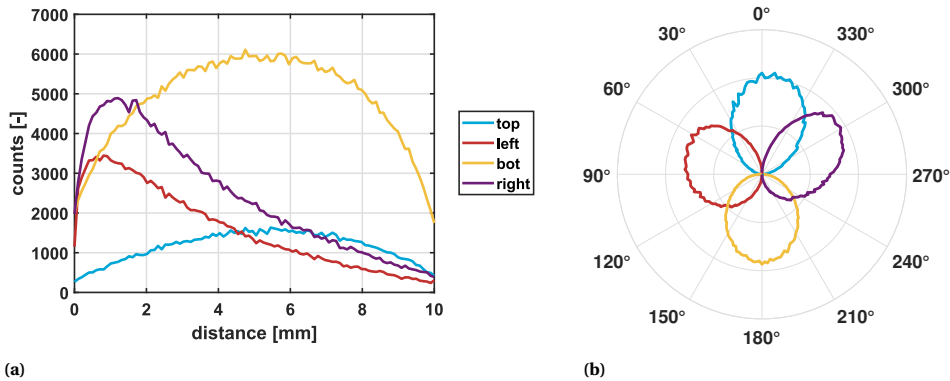


Figure 6.11: Intensity over position (a) and angle (normalized) (b) for 10x10 mm box with lossless directional scatterers, for different sides of the box. The mean free path of photons travelling through the box is 1 mm.

The results of a further decrease of the mean free path length are shown in Figure 6.12. We see that the amount of backscattered light has further increased and the amount of light reaching the top has further decreased. More important however, is that the angular distribution of the light has become slightly more symmetric, which goes against our objective.

This is consistent with our conclusions from Section 6.1. Each time the light is scattered, the étendue is increased. As there is no way of decreasing the étendue, because the scatterers do not absorb any of the light, it will increase until it has reached a

maximum where the light does not have a preferred direction anymore. In other words, independent of the scattering pattern of the nanoparticle, after enough scattering events, the angular distribution will become the same as that of a completely uniform scatterer.

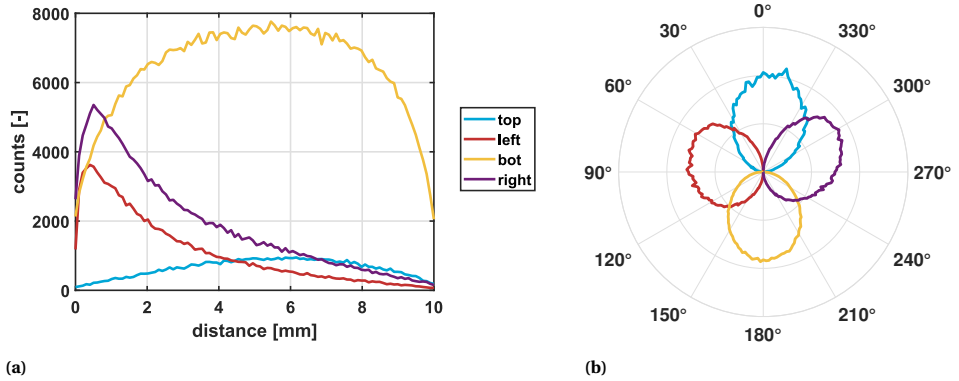


Figure 6.12: Intensity over position (a) and angle (normalized) (b) for 10x10 mm box with lossless directional scatterers, for different sides of the box. The mean free path of photons travelling through the box is 0.5 mm.

6.3.3. DIRECTIONAL SCATTERERS WITH ABSORPTION

As we have learned, the only way to decrease étendue, is to remove energy from the system. In this case, we can obtain it through absorption of the light by the scatterers. Therefore, we will use SiO₂ / Au core-semishell particles in air (at a wavelength of 500 nm). These particles have been discussed extensively in this thesis, their scatter pattern can be found in [Figure 3.27b](#) and [Figure 3.28](#).

Let us start with the low density of scatterers again. From [Figure 6.13](#), we see the strong directionality again. Of course, there is a large part of the light which has passed through the box without any scattering as for the other cases. So, we need to increase the amount of scatterers again.

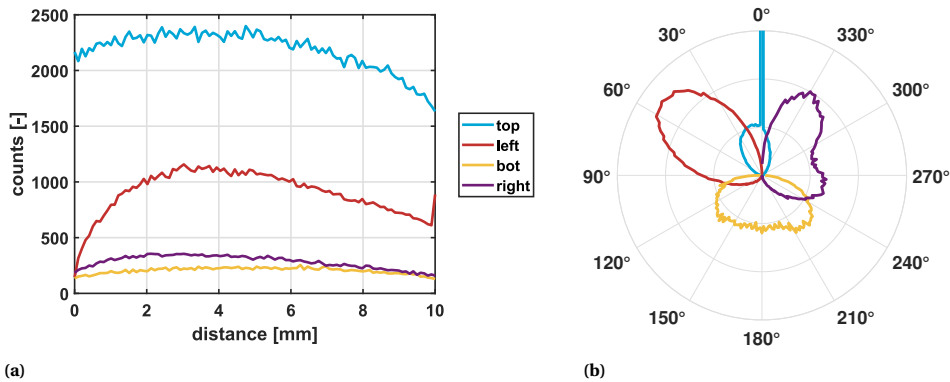


Figure 6.13: Intensity over position (a) and angle (normalized) (b) for 10x10 mm box with lossy directional scatterers, for different sides of the box. The mean free path of photons travelling through the box is 5 mm. 64% of the photons is absorbed.

The results for a mean free path length of 1 mm are shown in [Figure 6.14](#). In contrast to the lossless cases we discussed earlier, we see from the angular distribution of the light on the top that a large part of the light has not been scattered. Here, it is important to note the low amount of light that has actually reached the top edge. This is due to the large amount of absorption: 92% of the light has been absorbed inside the box.

The absorption by the scatterers effectively limits the amount of scatter events. This preserves the directionality we see in the angular distribution of the intensity. For the top specifically, only the photons which have not scattered or have only scattered once give a large enough contribution. This is the reason why the contribution of the light which has not scattered is still significant.

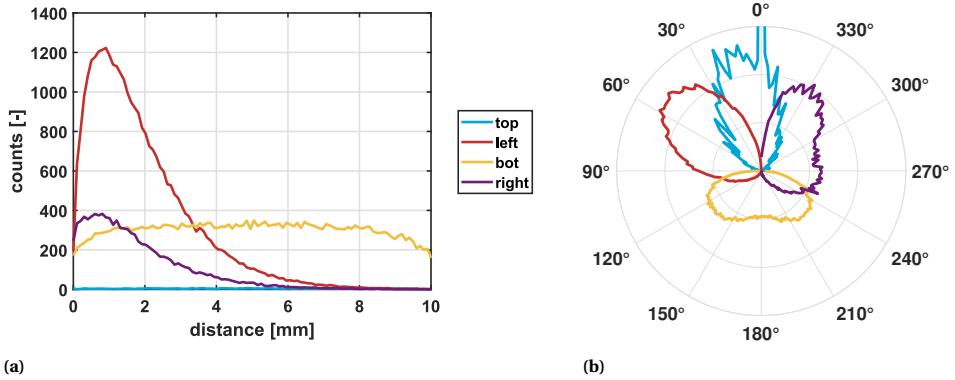


Figure 6.14: Intensity over position (a) and angle (normalized) (b) for 10x10 mm box with lossy directional scatterers, for different sides of the box. The mean free path of photons travelling through the box is 1 mm. 92% of the photons is absorbed.

6.4. SUMMARY AND OUTLOOK

In this chapter, we have seen that étendue plays an important role in scattering. In general, each scatter event increases étendue. As the only way to decrease étendue is by removing energy, in the multiple scattering regime directionality is quickly lost in the case of lossless scatterers. Directionality can be maintained when absorbing scatterers are used. However, much of the incident light is lost and the remaining light has either not scattered at all, or only a few times.

Where does this leave us with the goal of this thesis: the design of a volume with nanoparticles that has a desired scatter behaviour? In principle this can be done, however, only for the case where the amount of scatter events is very limited. This raises the question: why not use a surface with scatterers, the effectiveness of which has been shown a lot in literature? Here, we know the light will only scatter very little, and the portion of the light that scatters can be controlled through the scatter cross section of the particles and their separation. Furthermore, planar fabrication is much easier as this is done for many other applications. One could even think of multiplayer systems where possibly each layer has different nanoparticles to send the light in other directions.

For applications in where the light needs to be completely scrambled, many scattering events are needed. As we have seen, at that point directionality cannot be maintained and effectively any scatterer can be used.

7

CONCLUSION

7.1. CONCLUSIONS

IN this thesis, we have developed a theory for the broadband scattering of light using nanostructures in the optical spectrum. By combining two different materials into a single nanostructure, directional scattering can be achieved. Due to the different permittivity that the two materials have, the scattered field by each of them have a phase difference. This phase difference is dependent on the direction that the light is scattered in. As a result, light in certain direction interfere constructively, while interfering destructively in other directions.

The great advantage of this method is that the directionality is largely independent on the wavelength of the incident light, unlike traditional methods to achieve directional scattering which are based on resonances. These resonances are only present for a small bandwidth, therefore the scatter pattern can change drastically over the optical spectrum.

Based on this theory, we have also demonstrated an application of these directional scatterers in a grating. By creating grating elements which are composed of two different materials, the diffraction efficiency of a specific order can be greatly increased. However, we found that creating accurate simulations of such gratings is difficult, as the material properties depend highly on the shape and size at the nanolevel.

The single composite nanoparticles were fabricated using simple methods. This allows for the possibility of mass production and would make it cost-effective. The nanoparticles were created by starting with readily made nanospheres. Using sputtering and etching, a second material could be added to produce the composite nanoparticles.

For gratings, e-beam lithography was used to produce the gratings. Next, metal was evaporated on the side of the grating lines, by evaporating the metal at a high angle from the normal. To create a semiconductor material to further improve the performance of the composite gratings, samples were annealed.

Measurements of the nanoparticles have shown the same directional scattering as predicted by the developed theory and simulations. The gratings were also measured,

where we also found the expected improvement of the 1st diffraction order. However, the efficiency seems to be limited by losses due to absorption and diffuse scattering.

Finally, a theoretical analysis was made on the original idea of the PhD project: to create a volume with nanoparticles that can scatter an incident beam of light into a specific direction. It was found that this is not possible without significant loss of light. The reason behind this is due to the increase of étendue with every scatter event. If étendue increases too much, the light coming out of the volume will simply have a Lambertian distribution, the same for any generic diffusive volume.

Overall, we think this thesis contributes to the scientific understanding of directional scattering by single and multiple nanoparticles. Furthermore, this could lead to new applications in the field of lighting and spectroscopy. In the field of lighting this could lead to more energy efficient lighting. For spectroscopy, improvements in the quality of spectroscopic measurements can be attained through the development of more efficient gratings, improving our understanding of physical processes.

7.2. OUTLOOK AND RECOMMENDATIONS

The continuation of this work can be found in the main part of this work: the directional scattering by composite nanoparticles. Now that the broadband directional scattering has been proven, it is interesting to look at the macroscopic applications. In this section we will list a few possible directions for future research.

First and foremost, a problem with these particles that need to be solved is the strong wavelength dependence of the scattering cross section. In practice, this means that blue light is scattered much more than red light, which is of course detrimental for any broadband application. A potential method for solving this is by using broadband Mie resonances. By designing a composite nanoparticle which support Mie resonances so that the scattering cross section is almost constant over the entire visible spectrum, this would be solved. The difficulty is that this would likely interfere with the phase of the scattered field by the two materials of the composite nanoparticle. Therefore, more research is needed to see if it is possible to achieve this.

For other research directions, it is interesting to look further into applications in which embedded composite nanoparticles can be used. When particles are embedded in a medium, directional scattering can be achieved without the use of lossy materials, as is shown in [Figure 3.25](#). For example, a volume with embedded particles could be placed on top of an LED, to improve the outcoupling of light that would otherwise be internally refracted. Examples can already be found in literature[82–85], however little emphasis is put on the directionality of the outcoupled light.

Another application would be the production of a broadband diffuser with little reflection. Instead of creating a volumetric diffuser, one could make a diffuser composed of multiple layers of scatterers on a surface. This way, the amount of scatter events and the orientation of the particles can easily be controlled, mitigating the main disadvantages of having designed scatterers inside a volume. We have already seen in this thesis that the design of a scatterer with little backscattering and high directionality is possible. Subsequent layers could have scatterers which have a scatter pattern that accounts for the first one, such that hardly any light is backscattered.

Finally, it would be interesting to use a phase change material such as vanadiumoxide,

which changes from a dielectric material to a metallic with increasing temperature. The refractive index then changes accordingly, especially in the infrared part of the spectrum, where the imaginary part of the permittivity increases significantly with temperature[86]. This would mean that it could be possible to actively change the scattering direction of composite nanoparticle made with this material. Changing the temperature could change the angle at which the light is scattered.

A

MATHEMATICAL IDENTITIES AND DERIVATIONS

A.1. VECTOR IDENTITIES AND TENSORS

Below, a selection of vector identities used throughout this thesis is given[27]

$$\nabla \times \nabla \times \mathbf{A} = \nabla(\nabla \cdot \mathbf{A}) - \nabla^2 \mathbf{A} \quad (\text{A.1})$$

$$\nabla \times (\psi \mathbf{A}) = \psi(\nabla \times \mathbf{A}) + (\nabla \psi) \times \mathbf{A} \quad (\text{A.2})$$

$$\nabla \times \nabla \psi = 0 \quad (\text{A.3})$$

$$\nabla \cdot (\nabla \times \mathbf{A}) = 0 \quad (\text{A.4})$$

$$\nabla \cdot (\mathbf{A} \times \mathbf{B}) = \mathbf{B} \cdot (\nabla \times \mathbf{A}) - \mathbf{A} \cdot (\nabla \times \mathbf{B}) \quad (\text{A.5})$$

$$\mathbf{A} \cdot (\mathbf{B} \times \mathbf{C}) = \mathbf{B} \cdot (\mathbf{C} \times \mathbf{A}) = \mathbf{C} \cdot (\mathbf{A} \times \mathbf{B}) \quad (\text{A.6})$$

where \mathbf{A} , \mathbf{B} and \mathbf{C} are vector fields and ψ a scalar function.

Tensors are indicated by a line over the variable. The divergence of a tensor \overline{T} is defined as:

$$\nabla \cdot \overline{T} = \frac{\partial \overline{T}_{ik}}{\partial x_i} \mathbf{e}_k \quad (\text{A.7})$$

with \mathbf{e}_k a basis vector.

A.2. DERIVATION OF THE 3D GREENS FUNCTION FOR A DIPOLE

This derivation is based on the lecture notes of Advanced Photonics by H.P. Urbach[87]. Let us consider an electric dipole somewhere in a medium. The associated charge and current density is then given by

$$\rho(\mathbf{r}) = -\mathbf{p} \cdot \nabla \delta(\mathbf{r}), \quad (\text{A.8})$$

$$\mathbf{J}(\mathbf{r}) = -i\omega \mathbf{p} \delta(\mathbf{r}). \quad (\text{A.9})$$

The electromagnetic field emitted by this dipole follows the Maxwell equations, we have

$$\nabla \times \mathbf{E} = i\omega\mu_0\mathbf{H}, \quad (\text{A.10})$$

$$\nabla \cdot \mathbf{E} = -\mathbf{p} \cdot \nabla \delta(\mathbf{r}), \quad (\text{A.11})$$

$$\nabla \times \mathbf{H} = -i\omega\epsilon_0\epsilon_{\text{med}}\mathbf{E} - i\omega\mathbf{p}\delta(\mathbf{r}), \quad (\text{A.12})$$

$$\nabla \cdot \mathbf{H} = 0. \quad (\text{A.13})$$

Taking the curl of [Equation A.12](#) and using [Equation A.13](#), we can write down the wave equation using the identity of [Equation A.1](#):

$$\nabla \times \nabla \times \mathbf{H} = \omega^2\epsilon_0\epsilon_{\text{med}}\mu_0\mathbf{H} - i\omega\nabla \times [\mathbf{p}\delta(\mathbf{r})], \quad (\text{A.14})$$

$$\nabla^2 \mathbf{H} + \omega^2\epsilon_0\epsilon_{\text{med}}\mu_0\mathbf{H} = i\omega\nabla \times [\mathbf{p}\delta(\mathbf{r})] \quad (\text{A.15})$$

We see that the components of the magnetic field each satisfy the Helmholtz equation. The Greens function which satisfies the scalar Helmholtz equation

$$\nabla^2 G + k^2 G = \delta(\mathbf{r}). \quad (\text{A.16})$$

with a point source at the origin and radiates outwards is given by

$$G(r) = \frac{-e^{ikr}}{4\pi r}. \quad (\text{A.17})$$

The function G is called the free space Greens function. Let us now write out the right side of [Equation A.15](#), the x -component is given by

$$(i\omega\nabla \times [\mathbf{p}\delta(\mathbf{r})])_x = i\omega \left(p_z \frac{\partial \delta(\mathbf{r})}{\partial y} - p_y \frac{\partial \delta(\mathbf{r})}{\partial z} \right). \quad (\text{A.18})$$

The above looks like an operator acting on the delta function $\delta(\mathbf{r})$, we can recognize that [Equation A.15](#) is satisfied if

$$H_x = i\omega \left(p_z \frac{\partial G(r)}{\partial y} - p_y \frac{\partial G(r)}{\partial z} \right). \quad (\text{A.19})$$

By doing the same for the y and z component, we find that [Equation A.15](#) is satisfied for

$$\mathbf{H} = i\omega\nabla \times [\mathbf{p}G(r)]. \quad (\text{A.20})$$

Using the identity [Equation A.2](#), we arrive at the following expression for the magnetic field:

$$\mathbf{H}(\mathbf{r}) = \omega k \left[\left(1 - \frac{1}{ikr} \right) \frac{e^{ikr}}{4\pi r} \right] \hat{\mathbf{r}} \times \mathbf{p}. \quad (\text{A.21})$$

The electric field can be calculated according to [Equation A.12](#), by substituting [Equation A.20](#):

$$\mathbf{E}(\mathbf{r}) = \frac{i}{\omega\epsilon_0\epsilon_{\text{med}}} \nabla \times \mathbf{H} - \frac{\mathbf{p}}{\epsilon_0\epsilon_{\text{med}}} \delta(\mathbf{r}) \quad (\text{A.22})$$

$$= \frac{-1}{\epsilon_0\epsilon_{\text{med}}} \nabla \times \nabla \times [\mathbf{p}G(r)] - \frac{\mathbf{p}}{\epsilon_0\epsilon_{\text{med}}} \delta(\mathbf{r}) \quad (\text{A.23})$$

$$= \nabla^2(\mathbf{p}G(r)) - \nabla[\nabla \cdot (\mathbf{p}G(r))] - \frac{\mathbf{p}}{\epsilon_0\epsilon_{\text{med}}} \delta(\mathbf{r}). \quad (\text{A.24})$$

Using Equation A.16 we obtain

$$\mathbf{E}(\mathbf{r}) = -\frac{k^2}{\epsilon_0 \epsilon_{\text{med}}} \mathbf{p} G(r) - \nabla [\nabla \cdot (\mathbf{p} G(r))] \quad (\text{A.25})$$

$$= \frac{k^2}{\epsilon_0 \epsilon_{\text{med}}} \frac{e^{ikr}}{4\pi r} \mathbf{p} + \frac{1}{\epsilon_0 \epsilon_{\text{med}}} \nabla \left[\nabla \cdot \left(\mathbf{p} \frac{e^{ikr}}{4\pi r} \right) \right] \quad (\text{A.26})$$

$$= \left[k^2 \frac{\mathbf{r}}{r} \times \left(\mathbf{p} \times \frac{\mathbf{r}}{r} \right) + \left(3 \frac{\mathbf{r}}{r} \cdot \mathbf{p} \frac{\mathbf{r}}{r} - \mathbf{p} \right) \left(\frac{1}{r^2} - \frac{ik}{r} \right) \right] \frac{e^{ikr}}{4\pi \epsilon_0 \epsilon_{\text{med}} r}. \quad (\text{A.27})$$

A.3. ELECTRIC FIELD OF A GENERAL CURRENT DISTRIBUTION

For a general time-harmonic current distribution \mathbf{J} in a medium, the field is given by

$$\nabla \times \mathbf{E} = i\omega \mu_0 \mathbf{H} \quad (\text{A.28})$$

$$\nabla \times \mathbf{H} = -i\omega \epsilon_0 \epsilon_{\text{med}} \mathbf{E} + \mathbf{J} \quad (\text{A.29})$$

Let us assume the current distribution is bounded to some volume Ω . The current distribution can be then written as a linear superposition of electric dipoles:

$$\mathbf{J}(\mathbf{r}) = \int_{\Omega} \mathbf{J}(\mathbf{r}_0) \delta(\mathbf{r} - \mathbf{r}_0) d^3 r_0 \quad (\text{A.30})$$

with the dipole density given by

$$\mathbf{p}(\mathbf{r}) = \frac{\mathbf{J}(\mathbf{r})}{-i\omega}. \quad (\text{A.31})$$

Then, the total field generated by the current distribution is the linear superposition of the field radiated by the dipoles:

$$\mathbf{E}(\mathbf{r}) = \int \overline{G}_E(\mathbf{r} - \mathbf{r}_0) \frac{\mathbf{J}(\mathbf{r})}{-i\omega} d^3 r_0 \quad (\text{A.32})$$

with $\overline{G}_E(\mathbf{r} - \mathbf{r}_0)$ a 2-tensor which maps a dipole at the origin with dipole vector \mathbf{p} to the electric field in \mathbf{r} . Then, $\overline{G}_E(\mathbf{r}) \mathbf{p}$ is equal to the expression we found for a single dipole in the previous section (Equation A.27):

$$\overline{G}_E(\mathbf{r}) \mathbf{p} = \left[k^2 \frac{\mathbf{r}}{r} \times \left(\mathbf{p} \times \frac{\mathbf{r}}{r} \right) + \left(3 \frac{\mathbf{r}}{r} \cdot \mathbf{p} \frac{\mathbf{r}}{r} - \mathbf{p} \right) \left(\frac{1}{r^2} - \frac{ik}{r} \right) \right] \frac{e^{ikr}}{4\pi \epsilon_0 \epsilon_{\text{med}} r}. \quad (\text{A.33})$$

A.4. FAR FIELD APPROXIMATION

If we are only interested in the far field contributions where $r \gg \lambda$, we can simplify Equation A.33 to

$$\overline{G}_E(\mathbf{r} - \mathbf{r}_0) \mathbf{p} = k^2 \frac{\mathbf{r} - \mathbf{r}_0}{|\mathbf{r} - \mathbf{r}_0|} \times \left(\mathbf{p} \times \frac{\mathbf{r} - \mathbf{r}_0}{|\mathbf{r} - \mathbf{r}_0|} \right) \frac{e^{ik|\mathbf{r} - \mathbf{r}_0|}}{4\pi \epsilon_0 \epsilon_{\text{med}} |\mathbf{r} - \mathbf{r}_0|} \quad (\text{A.34})$$

$$= k^2 \hat{\mathbf{r}} \times (\mathbf{p} \times \hat{\mathbf{r}}) \frac{e^{ik|\mathbf{r} - \mathbf{r}_0|}}{4\pi \epsilon_0 \epsilon_{\text{med}} r} \quad (\text{A.35})$$

For the phase factor, we can use that

$$k|\mathbf{r} - \mathbf{r}_0| = k\sqrt{r^2 + r_0^2 - 2\mathbf{r} \cdot \mathbf{r}_0} \quad (\text{A.36})$$

$$= kr\sqrt{1 + \frac{r_0^2}{r^2} - 2\frac{\mathbf{r} \cdot \mathbf{r}_0}{r^2}} \quad (\text{A.37})$$

$$\approx kr\left(1 + \frac{r_0^2}{2r^2} - \frac{\mathbf{r} \cdot \mathbf{r}_0}{r^2}\right) \quad (\text{A.38})$$

$$= kr + k\frac{r_0^2}{2r^2} - k\frac{\mathbf{r} \cdot \mathbf{r}_0}{r} \quad (\text{A.39})$$

For large r which satisfies

$$\frac{r}{\lambda} > \left(\frac{D}{\lambda}\right)^2, \quad (\text{A.40})$$

with D the diameter of the smallest region that contains the scatterer, the second term in Equation A.39 disappears. So that we get

$$\bar{G}_E(\mathbf{r} - \mathbf{r}_0)\mathbf{p} = \frac{k^2}{4\pi\epsilon_0\epsilon_{\text{med}}r} e^{ikr} e^{-ik\hat{\mathbf{r}} \cdot \mathbf{r}_0} \hat{\mathbf{r}} \times (\mathbf{p} \times \hat{\mathbf{r}}) \quad (\text{A.41})$$

A.5. VECTOR SPHERICAL HARMONICS

The vector spherical harmonics are given by[34]

$$\begin{aligned} \mathbf{L}(kr, \theta, \varphi) = & \sqrt{\frac{(2l+1)(l-m)!}{4\pi(l+m)!}} \left\{ z_l'(kr) Y_l^m \hat{\mathbf{r}} + \right. \\ & \left. \frac{1}{kr} z_l(kr) e^{im\varphi} \left[\frac{dP_l^m(\cos\theta)}{d\theta} \hat{\boldsymbol{\theta}} + \frac{im}{\sin\theta} P_l^m(\cos\theta) \hat{\boldsymbol{\phi}} \right] \right\}, \quad (\text{A.42}) \end{aligned}$$

$$\begin{aligned} \mathbf{M}(kr, \theta, \varphi) = & \sqrt{\frac{(2l+1)(l-m)!}{4\pi l(l+1)(l+m)!}} z_l(kr) e^{im\varphi} \left[\frac{im}{\sin\theta} P_l^m(\cos\theta) \hat{\boldsymbol{\theta}} - \frac{dP_l^m(\cos\theta)}{d\theta} \hat{\boldsymbol{\phi}} \right], \quad (\text{A.43}) \end{aligned}$$

$$\begin{aligned} \mathbf{N}(kr, \theta, \varphi) = & \sqrt{\frac{(2l+1)(l-m)!}{4\pi l(l+1)(l+m)!}} \left\{ \frac{l(l+1)z_l(kr)}{kr} Y_l^m \hat{\mathbf{r}} + \right. \\ & \left. \frac{(kr z_l(kr))'}{kr} e^{im\varphi} \left[\frac{dP_l^m(\cos\theta)}{d\theta} \hat{\boldsymbol{\theta}} + \frac{im}{\sin\theta} P_l^m(\cos\theta) \hat{\boldsymbol{\phi}} \right] \right\}, \quad (\text{A.44}) \end{aligned}$$

where the ' signifies the derivative with respect to kr , and $z_l(kr)$ is any of the spherical Bessel functions j_l , y_l , the spherical Hankel function of the first kind $h_l^{(1)}$ and the second kind $h_l^{(2)}$ with order l .

A.6. LORENTZ RECIPROCITY

Throughout this thesis we have looked at the scattering by nanoparticles when a field is incident from a specific direction. We have not tried to see if we can design a nanoparticle which scatters light into a desired direction, independent of the direction of the incident field. There is a good reason for that, namely that Lorentz reciprocity prevents us from doing so.

Let us start by deriving the Lorentz reciprocity theorem[26]. Let us consider some time-harmonic current density \mathbf{j}_1 that produces an electric field \mathbf{E}_1 and magnetic field \mathbf{B}_1 . A second time-harmonic current density \mathbf{j}_2 similarly produces the fields \mathbf{E}_2 and \mathbf{B}_2 . From the Maxwell equations, we have

$$\nabla \times \mathbf{E} = i\omega \mathbf{B}, \quad (\text{A.45})$$

$$\nabla \times \mathbf{B} = \mu_0 \mathbf{j} - i\omega \mu_0 \epsilon \mathbf{E}. \quad (\text{A.46})$$

Integrating the dot product of \mathbf{E}_2 with the curl of \mathbf{B}_1 minus the dot product of \mathbf{E}_1 with the curl of \mathbf{B}_2 over a volume V , we get

$$\int_V (\mathbf{E}_2 \cdot \nabla \times \mathbf{B}_1 - \mathbf{E}_1 \cdot \nabla \times \mathbf{B}_2) d^3 r = \mu_0 \int_V (\mathbf{j}_1 \cdot \mathbf{E}_2 - \mathbf{j}_2 \cdot \mathbf{E}_1) d^3 r. \quad (\text{A.47})$$

Doing the same again, but now exchanging the electric and magnetic fields, we obtain

$$\int_V (\mathbf{B}_2 \cdot \nabla \times \mathbf{E}_1 - \mathbf{B}_1 \cdot \nabla \times \mathbf{E}_2) d^3 r = 0. \quad (\text{A.48})$$

Using the vector identities at the start of this Appendix, we have

$$\int_V \nabla \cdot (\mathbf{E}_1 \times \mathbf{B}_2 - \mathbf{E}_2 \times \mathbf{B}_1) d^3 r = \mu_0 \int_V (\mathbf{j}_1 \cdot \mathbf{E}_2 - \mathbf{j}_2 \cdot \mathbf{E}_1) d^3 r. \quad (\text{A.49})$$

Finally, using the divergence equation, we arrive at

$$\int_S (\mathbf{E}_1 \times \mathbf{B}_2 - \mathbf{E}_2 \times \mathbf{B}_1) \cdot d\mathbf{S} = \mu_0 \int_V (\mathbf{j}_1 \cdot \mathbf{E}_2 - \mathbf{j}_2 \cdot \mathbf{E}_1) d^3 r, \quad (\text{A.50})$$

where the volume V is bounded by the surface S .

The above is the general form of the reciprocity theorem. For our purpose, we will specialize this for a spherical volume which encloses both sources. Furthermore, we will assume that the volume is large enough so that the fields on the surface S can be regarded as radiation fields. In that case, for the integral over the surface S we have $d\mathbf{S} = \hat{\mathbf{r}} dS$ and $\hat{\mathbf{r}} \times \mathbf{E} = c\mathbf{B}$. Using the vector triple product (Equation A.6), we have

$$\int_S (\mathbf{E}_1 \times \mathbf{B}_2 - \mathbf{E}_2 \times \mathbf{B}_1) \cdot \hat{\mathbf{r}} dS = \int_S (\hat{\mathbf{r}} \times \mathbf{E}_1 \cdot \mathbf{B}_2 - \hat{\mathbf{r}} \times \mathbf{E}_2 \cdot \mathbf{B}_1) dS = 0 \quad (\text{A.51})$$

Then we can rewrite Equation A.50 into

$$\int_V \mathbf{j}_1 \cdot \mathbf{E}_2 d^3 r = \int_V \mathbf{j}_2 \cdot \mathbf{E}_1 d^3 r. \quad (\text{A.52})$$

A

We can interpret this equation as follows: the relationship between a source and its resulting electric field is unchanged if their positions are interchanged. We can apply this concept to the subject of scattering by nanoparticles. If we were able to design a nanoparticle that scatters into a specific direction for fields incident from all directions, following reciprocity, fields coming from that specific direction would scatter into all directions. This clearly creates a paradox and is therefore not possible.

More specifically, we can determine what the average scatter direction is for all incident angles in the form of an indent spherical waves centered on the nanoparticle. Following reciprocity, the resulting scattered field must then be a spherical wave. In other words; on average, a nanoparticle cannot have a preferential scattering direction¹.

A.7. ELECTRIC AND MAGNETIC OCTUPOLE EXPRESSIONS

Expressions for the electric and magnetic octupole resonances were obtained through the method outlined in ref.[37]. These expressions are used in the multipole analysis of nanostructures in [Chapter 3](#).

The scattering cross sections are given by

$$\sigma_{EO} = \frac{2k^2 k_0^6}{3780\pi\epsilon_0^2 |\mathbf{E}_{\text{inc}}|^2} |O^e + O^{e(t)}|^2 \quad (\text{A.53})$$

$$\sigma_{MO} = \frac{2k^2 k_0^6}{3780\pi\epsilon_0^2 |\mathbf{E}_{\text{inc}}|^2 c^2} |O^m|^2 \quad (\text{A.54})$$

¹Reciprocity can be broken in special circumstances, for example for non-linear media. However, these cases are not considered in this thesis.

The elements of the electric octupole tensor are given by

$$O_{xyz}^e = \frac{3i}{\omega} \int \frac{6}{5} (xyJ_z + zxJ_y + yzJ_x) \frac{j_2(kr)}{(kr)^2} d^3 \mathbf{r} \quad (\text{A.55})$$

$$O_{xxx}^e = \frac{3i}{\omega} \int [15x^2 J_x - 3r^2 J_x - 6x(\mathbf{r} \cdot \mathbf{J})] \frac{j_2(kr)}{(kr)^2} d^3 \mathbf{r} \quad (\text{A.56})$$

$$O_{yyy}^e = \frac{3i}{\omega} \int [15y^2 J_y - 3r^2 J_y - 6y(\mathbf{r} \cdot \mathbf{J})] \frac{j_2(kr)}{(kr)^2} d^3 \mathbf{r} \quad (\text{A.57})$$

$$O_{zzz}^e = \frac{3i}{\omega} \int [15z^2 J_z - 3r^2 J_z - 6z(\mathbf{r} \cdot \mathbf{J})] \frac{j_2(kr)}{(kr)^2} d^3 \mathbf{r} \quad (\text{A.58})$$

$$O_{xyy}^e = \frac{3i}{\omega} \int \left[(33yJ_y + 3zJ_z - 9(\mathbf{r} \cdot \mathbf{J}))x + (12y^2 - 3z^2)J_x \right] \frac{j_2(kr)}{(kr)^2} d^3 \mathbf{r} \quad (\text{A.59})$$

$$O_{xzz}^e = \frac{3i}{\omega} \int \left[(33zJ_z + 3yJ_y - 9(\mathbf{r} \cdot \mathbf{J}))x + (12z^2 - 3y^2)J_x \right] \frac{j_2(kr)}{(kr)^2} d^3 \mathbf{r} \quad (\text{A.60})$$

$$O_{yxx}^e = \frac{3i}{\omega} \int \left[(33xJ_x + 3zJ_z - 9(\mathbf{r} \cdot \mathbf{J}))y + (12z^2 - 3x^2)J_y \right] \frac{j_2(kr)}{(kr)^2} d^3 \mathbf{r} \quad (\text{A.61})$$

$$O_{yzz}^e = \frac{3i}{\omega} \int \left[(33zJ_z + 3xJ_x - 9(\mathbf{r} \cdot \mathbf{J}))y + (12z^2 - 3x^2)J_y \right] \frac{j_2(kr)}{(kr)^2} d^3 \mathbf{r} \quad (\text{A.62})$$

$$O_{zxx}^e = \frac{3i}{\omega} \int \left[(33xJ_x + 3yJ_y - 9(\mathbf{r} \cdot \mathbf{J}))z + (12y^2 - 3x^2)J_z \right] \frac{j_2(kr)}{(kr)^2} d^3 \mathbf{r} \quad (\text{A.63})$$

$$O_{zyy}^e = \frac{3i}{\omega} \int \left[(33yJ_y + 3xJ_x - 9(\mathbf{r} \cdot \mathbf{J}))z + (12x^2 - 3y^2)J_z \right] \frac{j_2(kr)}{(kr)^2} d^3 \mathbf{r} \quad (\text{A.64})$$

The elements of the electric toroidal octupole tensor are given by

$$O_{xyz}^{e(t)} = -k^2 \frac{135i}{4\omega} \int 2 \left[xy(x^2 + y^2)J_z + zx(x^2 + z^2)J_y + \right. \\ \left. yz(y^2 + z^2)J_x - 6xyz(\mathbf{r} \cdot \mathbf{J}) \right] \frac{j_4(kr)}{(kr)^4} d^3 \mathbf{r} \quad (\text{A.65})$$

$$O_{xxx}^{e(t)} = -k^2 \frac{135i}{4\omega} \int \left[r^2 x^2 J_x + xr^2(\mathbf{r} \cdot \mathbf{J}) - x^3(\mathbf{r} \cdot \mathbf{J}) - \frac{2}{5} r^4 J_x \right] \frac{j_4(kr)}{(kr)^4} d^3 \mathbf{r} \quad (\text{A.66})$$

$$O_{yyy}^{e(t)} = -k^2 \frac{135i}{4\omega} \int \left[r^2 y^2 J_y + yr^2(\mathbf{r} \cdot \mathbf{J}) - y^3(\mathbf{r} \cdot \mathbf{J}) - \frac{2}{5} r^4 J_y \right] \frac{j_4(kr)}{(kr)^4} d^3 \mathbf{r} \quad (\text{A.67})$$

$$O_{zzz}^{e(t)} = -k^2 \frac{135i}{4\omega} \int \left[r^2 z^2 J_z + zr^2(\mathbf{r} \cdot \mathbf{J}) - z^3(\mathbf{r} \cdot \mathbf{J}) - \frac{2}{5} r^4 J_z \right] \frac{j_4(kr)}{(kr)^4} d^3 \mathbf{r} \quad (\text{A.68})$$

$$O_{xyy}^{e(t)} = -k^2 \frac{135i}{4\omega} \int \left[r^2 y^2 J_x + 2xyr^2 J_y + xr^2(\mathbf{r} \cdot \mathbf{J}) - 7xy^2(\mathbf{r} \cdot \mathbf{J}) - \frac{1}{5} r^4 J_x \right] \frac{j_4(kr)}{(kr)^4} d^3 \mathbf{r} \quad (\text{A.69})$$

$$O_{xzz}^{e(t)} = -k^2 \frac{135i}{4\omega} \int \left[r^2 z^2 J_x + 2x zr^2 J_z + xr^2(\mathbf{r} \cdot \mathbf{J}) - 7xz^2(\mathbf{r} \cdot \mathbf{J}) - \frac{1}{5} r^4 J_x \right] \frac{j_4(kr)}{(kr)^4} d^3 \mathbf{r} \quad (\text{A.70})$$

$$O_{yxx}^{e(t)} = -k^2 \frac{135i}{4\omega} \int \left[r^2 x^2 J_y + 2xyr^2 J_x + yr^2(\mathbf{r} \cdot \mathbf{J}) - 7x^2 y(\mathbf{r} \cdot \mathbf{J}) - \frac{1}{5} r^4 J_y \right] \frac{j_4(kr)}{(kr)^4} d^3 \mathbf{r} \quad (\text{A.71})$$

$$O_{yzz}^{e(t)} = -k^2 \frac{135i}{4\omega} \int \left[r^2 z^2 J_y + 2y zr^2 J_z + yr^2(\mathbf{r} \cdot \mathbf{J}) - 7yz^2(\mathbf{r} \cdot \mathbf{J}) - \frac{1}{5} r^4 J_y \right] \frac{j_4(kr)}{(kr)^4} d^3 \mathbf{r} \quad (\text{A.72})$$

$$O_{zxx}^{e(t)} = -k^2 \frac{135i}{4\omega} \int \left[r^2 x^2 J_z + 2x zr^2 J_x + zr^2(\mathbf{r} \cdot \mathbf{J}) - 7x^2 z(\mathbf{r} \cdot \mathbf{J}) - \frac{1}{5} r^4 J_z \right] \frac{j_4(kr)}{(kr)^4} d^3 \mathbf{r} \quad (\text{A.73})$$

$$O_{zyy}^{e(t)} = -k^2 \frac{135i}{4\omega} \int \left[r^2 y^2 J_z + 2y zr^2 J_y + zr^2(\mathbf{r} \cdot \mathbf{J}) - 7y^2 z(\mathbf{r} \cdot \mathbf{J}) - \frac{1}{5} r^4 J_z \right] \frac{j_4(kr)}{(kr)^4} d^3 \mathbf{r} \quad (\text{A.74})$$

The elements of the magnetic octupole tensor are given by

$$O_{xyz}^m = \frac{63}{4} \int \frac{-5}{2} [xy(\mathbf{r} \times \mathbf{J})_z + yz(\mathbf{r} \times \mathbf{J})_x + xz(\mathbf{r} \times \mathbf{J})_y] \frac{j_3(kr)}{(kr)^3} d^3\mathbf{r} \quad (\text{A.75})$$

$$O_{xxx}^m = \frac{63}{4} \int [(r^2 - 6x^2)(\mathbf{r} \times \mathbf{J})_x] \frac{j_3(kr)}{(kr)^3} d^3\mathbf{r} \quad (\text{A.76})$$

$$O_{yyy}^m = \frac{63}{4} \int [(r^2 - 6y^2)(\mathbf{r} \times \mathbf{J})_y] \frac{j_3(kr)}{(kr)^3} d^3\mathbf{r} \quad (\text{A.77})$$

$$O_{zzz}^m = \frac{63}{4} \int [(r^2 - 6z^2)(\mathbf{r} \times \mathbf{J})_z] \frac{j_3(kr)}{(kr)^3} d^3\mathbf{r} \quad (\text{A.78})$$

$$O_{xyy}^m = \frac{63}{4} \int \left[(r^2 - 6y^2)(\mathbf{r} \times \mathbf{J})_x - \frac{5}{2}xy(\mathbf{r} \times \mathbf{J})_y \right] \frac{j_3(kr)}{(kr)^3} d^3\mathbf{r} \quad (\text{A.79})$$

$$O_{xzz}^m = \frac{63}{4} \int \left[(r^2 - 6z^2)(\mathbf{r} \times \mathbf{J})_x - \frac{5}{2}xy(\mathbf{r} \times \mathbf{J})_z \right] \frac{j_3(kr)}{(kr)^3} d^3\mathbf{r} \quad (\text{A.80})$$

$$O_{yxx}^m = \frac{63}{4} \int \left[(r^2 - 6x^2)(\mathbf{r} \times \mathbf{J})_y - \frac{5}{2}xy(\mathbf{r} \times \mathbf{J})_x \right] \frac{j_3(kr)}{(kr)^3} d^3\mathbf{r} \quad (\text{A.81})$$

$$O_{yzz}^m = \frac{63}{4} \int \left[(r^2 - 6z^2)(\mathbf{r} \times \mathbf{J})_y - \frac{5}{2}yz(\mathbf{r} \times \mathbf{J})_z \right] \frac{j_3(kr)}{(kr)^3} d^3\mathbf{r} \quad (\text{A.82})$$

$$O_{zxx}^m = \frac{63}{4} \int \left[(r^2 - 6x^2)(\mathbf{r} \times \mathbf{J})_z - \frac{5}{2}xz(\mathbf{r} \times \mathbf{J})_x \right] \frac{j_3(kr)}{(kr)^3} d^3\mathbf{r} \quad (\text{A.83})$$

$$O_{zyy}^m = \frac{63}{4} \int \left[(r^2 - 6y^2)(\mathbf{r} \times \mathbf{J})_z - \frac{5}{2}yz(\mathbf{r} \times \mathbf{J})_y \right] \frac{j_3(kr)}{(kr)^3} d^3\mathbf{r} \quad (\text{A.84})$$

B

FEM SIMULATIONS USING COMSOL

B.1. MODELLING OF CORE-SHELL PARTICLES

The scattering of the composite nanoparticles were modeled using COMSOL Multiphysics® v5.6. To determine the fields and scattering characteristics, the "Electromagnetic Waves, Frequency Domain (ewfd)" module was used.

For the core-shell nanoparticles, the 3D geometry was constructed using a single sphere with multiple layers. The radius of the sphere is the sum of the radius of the core of the nanoparticle (r_{core}), the thickness of the shell of the nanoparticle (t_{shell}), the thickness of the layer with the material properties of the medium (t_{med}) and the thickness of the layer of the perfectly matching layer (t_{PML}):

$$r = r_{\text{core}} + t_{\text{shell}} + t_{\text{med}} + t_{\text{PML}}. \quad (\text{B.1})$$

In order to properly simulate a nanoparticle in an infinite homogeneous space, the thickness of the medium was chosen to be at least half of the wavelength of the light inside that medium. For the perfectly matching layer (PML) the same considerations apply:

$$t_{\text{med}} = t_{\text{PML}} \geq \frac{\lambda_0}{2n_{\text{med}}}, \quad (\text{B.2})$$

where λ_0 is the wavelength of the light in vacuum, and n_{med} the refractive index of the medium.

Next the material properties were applied to the different components of the nanoparticle. When real materials were simulated, optical constants were used from the database that is included in the COMSOL installation. Specifically, for gold used in the simulations, data from McPeak et. al.[88] was used. For silica, data from Malitson[89] was used. For air, the optical constants of vacuum were used.

For the definition of the physics problem, a (incident) background electric field in the z -direction was defined by

$$\mathbf{E} = E_0 \exp(-ik_0 x) \hat{z}. \quad (\text{B.3})$$

Next, scattering boundary conditions were applied to the surface of the full sphere. Furthermore, the far field domain was defined over the boundary layer. The far field calculation was performed over the boundary surface between the medium and the PML.

A mesh was created using the default settings of COMSOL: a physics-controlled mesh with normal sized elements.

The solver was a direct stationary solver PARDISO; it was found that the simulation completed faster than the suggested iterative solver, producing equivalent results. Moreover, sometimes the iterative solver would not converge to a solution, where the PARDISO solver always produced plausible results.

To determine the scattered far field, the COMSOL plot group "2D Far Field" in combination with the "Radiation Pattern" was used. The normal vector was chosen to be in the z -direction and the reference direction in the x -direction. To determine the scattered far field produced by the core and shell separately, the "Polar Plot Group" was used, combined with a "Line Graph" for each point on the θ -axis of the produced polar plot. The scattered field was then calculated using the Lippmann-Schwinger integral equation (Equation 3.1). The location where the far field was evaluated, was at a distance of 1 m away from the nanoparticle at different angles. For calculating the scattered field over the core, a volume integration was defined, selecting the core part of the geometry. Similar steps were taken for the shell.

To validate these calculations, the scattered field by the entire particle was calculated, where the integration was defined over the core and shell. The results of this calculation was then compared to the results from the "2D Far Field" in combination with the "Radiation Pattern". The resulting scatter patterns were found to be equal.

The scattering (σ_{sca}), absorption (σ_{abs}) and extinction cross section (σ_{ext}) were calculated as follows:

$$\sigma_{\text{sca}} = \int_{\Omega} \frac{\hat{\mathbf{n}} \cdot \mathbf{S}_{\text{sca}}}{n_{\text{med}} E_0^2 / 2Z_0}, \quad (\text{B.4})$$

$$\sigma_{\text{abs}} = \int_V \frac{Q}{n_{\text{med}} E_0^2 / 2Z_0}, \quad (\text{B.5})$$

$$\sigma_{\text{ext}} = \sigma_{\text{sca}} + \sigma_{\text{abs}}, \quad (\text{B.6})$$

with Ω the surface used for the far field calculation, Z_0 is the impedance of free space, \mathbf{S}_{sca} the Poynting vector of the scattered field, V the volume of the entire particle and Q the total power dissipated. These calculations were then validated against available multi-layer Mie code [52], the results of the COMSOL simulations and Mie code was found to be equal.

B.2. COMSOL MODELLING OF CORE-SEMISHELL PARTICLES

Core-semishell particles were modelled by creating another sphere with the radius of the sum of the core radius and the shell thickness. Half of this sphere was removed by a block covering the xz -plane and extending to the negative y -direction using the intersection function. As a result, a core-semishell particle was constructed, with the shell present in the space with negative y . For clarity, the resulting geometry as obtained in COMSOL is shown in Figure B.1.

The cubic particle was made using similar techniques, making sure that the distance from the particle to the PML was large enough to provide accurate results.

Sweeps over the of the core and shell permittivity were done using the parametric sweep option in COMSOL. For each combination of core and shell permittivity, the angle at which the scattered field magnitude was greatest, was calculated using the "Derived Values" function. This maximum was calculated over the same surface as the surface used for the far field calculation.

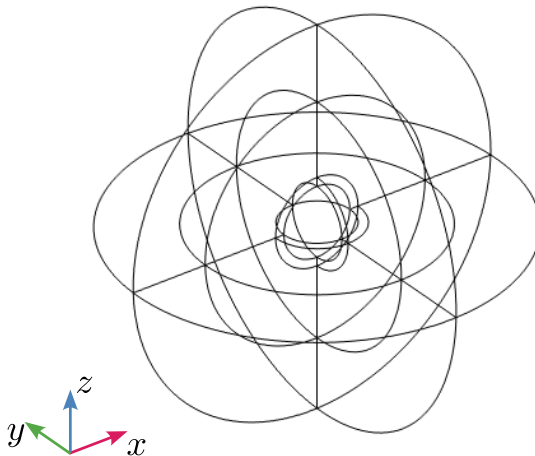


Figure B.1: Core-semishell geometry obtained in COMSOL. The outer layer is the PML, the next layer includes the medium and the core-semishell nanoparticle. Here, the semishell is on the $-y$ side of the core.

B.3. MODELLING OF A COMPOSITE NANOPARTICLE ON A SUBSTRATE

The modelling of a nanoparticle on top of a substrate is a bit more complicated than a particle floating in free space. First, the field is calculated in the case where only the substrate and no particle is present. Next, the calculated field is used as the background field when calculating the scattered field of the particle. In COMSOL this is done by having two "Physics Interfaces".

For the first interface, two wave equation domains are introduced. For the first domain, which encompasses everything except the particle, no changes are made. For the second domain, which is the particle, the refractive index is made equal to the medium. This effectively removes the particle in this case.

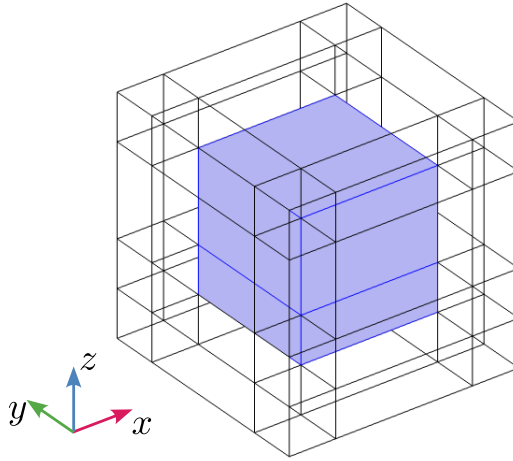
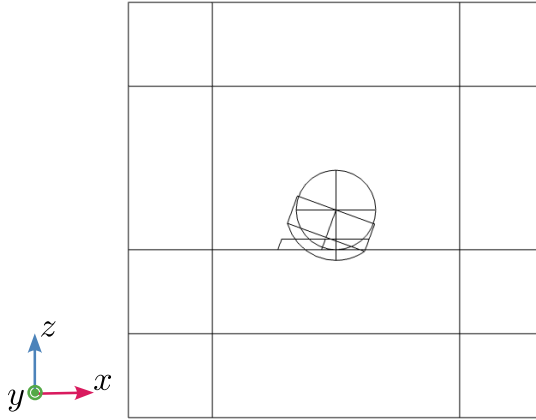


Figure B.2: Geometry used in COMSOL, the outer wire-frame consists of a PML, only used in the second Physics Interface. On the side of the blue box, periodic boundary conditions are applied. On the bottom and top respectively, a periodic input and output port is placed.

The geometry of the space surrounding the particle is a cube as can be seen in [Figure B.2](#). The outer cube consists of a PML, which will only be used for the second step when calculating the scattered field. Periodic boundary conditions are applied to the inner cube to simulate a substrate that extends into infinity in the xy -plane. The incident field is produced using a periodic port on the bottom of the inner cube. The field can exit the geometry on the top through another periodic port. Performing this simulations, we know the background field to use in the next "Physics Interface".

In the second interface is formulated as a scattered field problem, the same settings are used as with a particle in free space. With the exception that the substrate is of course still present. To determine the intensity in the far field with which the measurements are compared, a plane above the particle is defined over which the electric far field is calculated. Because we know the distance of this plane to the particle, using a simple MATLAB script we can determine the angular scatter pattern from here.

The particle itself is constructed similarly to how it is fabricated. First, a sphere is placed on top of a rectangle making up the substrate. A second sphere is placed at the same spot with a radius of $r = r_{\text{core}} + t_{\text{shell}}$. Furthermore, a rectangle with a thickness of t_{shell} is placed on top of the substrate. This is analogous to result of the sputtering step. Next, a cylinder is placed over the core of the nanoparticle. Its center coincides with that of the core and the angle of the symmetry axis is equal to the etching angle. The radius of which is slightly larger than that of the core, to avoid meshing problems. The intersection operation is used to remove everything of the "sputtered" shell material except for what is inside the cylinder. A side view of the result can be seen in [Figure B.3](#) and [Figure B.4](#). Part of the constructed shell protrudes inside the substrate, for this part the substrate material is assigned.



B

Figure B.3: Side view of the geometry of the constructed composite nanoparticle, which sits on top of a substrate. The PML consist of the outer layer.

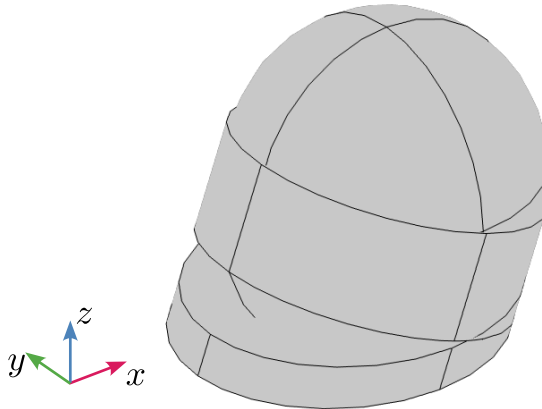


Figure B.4: 3D Geometry of the constructed composite nanoparticle.

B.4. GRATING SIMULATIONS

B.4.1. SIMULATIONS OF A SINGLE GRATING ELEMENT

The simulations of a single grating elements are not trivial, due to the presence of a substrate. The scattering of the grating element was simulated as a response to an incident field E_{inc} . From this, the total field E_{tot} was calculated using the COMSOL routines. From here, the scattered field (and radiation pattern) can be calculated according to:

$$E_{sca} = E_{tot} - E_{inc} \quad (B.7)$$

Without a substrate, the incident field would be given by a plane wave as input for the simulation. To account for the presence of a substrate, the incident field was modified. To start, a rectangular geometry was made with periodic boundary conditions and an input and output port. For this simulation, only the substrate was present. The geometry is shown in [Figure B.5](#). Using a input plane wave, the total field due to the presence of the substrate could be calculated.

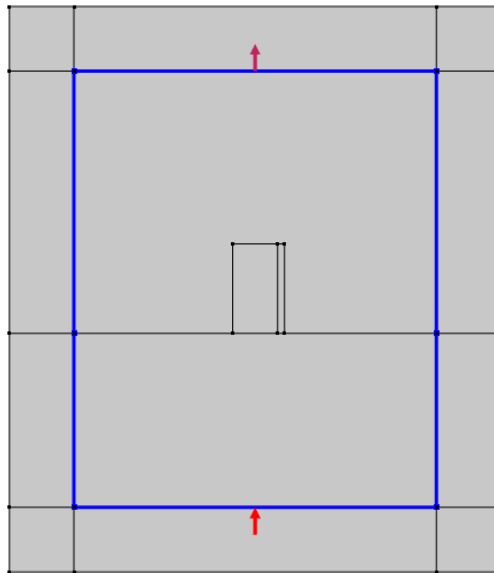
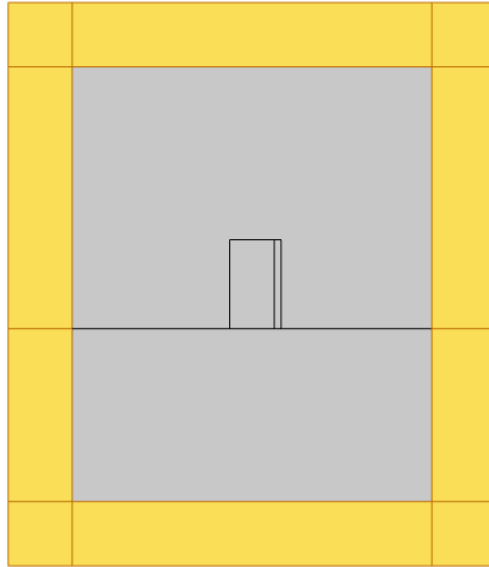


Figure B.5: Geometry used for the first part of the simulation. The blue boundaries are periodic boundary conditions and input and output ports (marked by the arrows). For this part of the simulation, the grating element has the same refractive index as the medium. This is to calculate the total field to be used in the second part of the simulation.

The result of this simulation was then used as the incident field for the simulation where the grating element was present. The periodic boundary conditions and ports were replaced by perfectly matching layers. The geometry is shown in [Figure B.6](#).

From here, the problem is approached as a standard scattering problem where the scattered field and related radiation pattern is calculated.



B

Figure B.6: Geometry used for the second part of the simulation. The yellow parts are the perfectly matching layers. The presence of the substrate is accounted for by using the calculated total field of the first part of the simulation as the incident field.

B.4.2. SIMULATIONS OF GRATINGS

Gratings were simulated similar to part one of the simulations for a single grating element. A geometry was made with a pitch equal to the grating pitch. The bottom half of the geometry is the substrate and the top half is the medium. The grating element was placed on top of the substrate. Periodic boundary conditions were applied to the side walls of the geometry. An input port was placed at the bottom, driven by a plane wave. At the top an output port was placed. The geometry is shown in [Figure B.7](#).

Using COMSOL, the diffraction orders were calculated and included in the top and bottom port, such that they are not reflected at those boundaries and the diffraction efficiency of each order can be calculated.

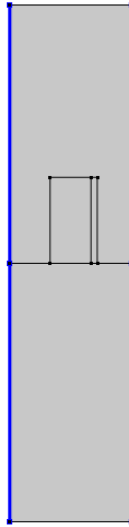


Figure B.7: Geometry used for the second part of the simulation. The yellow parts are the perfectly matching layers. For this part of the simulation, the substrate has the same refractive index as the medium. The presence of the substrate is accounted for by using the calculated total field of the first part of the simulation as the incident field.

ACKNOWLEDGEMENTS

First of all, I would like to thank my daily supervisor Aurèle Adam for all the support he has given me. When I was looking for a PhD position, he was the one who made me aware of the project I ended up doing. During my PhD, he was always happy to give me valuable advice and I always really enjoyed talking physics together. I fondly look back on the scientific discussions we had, starting from your -in your own words- dumb questions leading to great insights. Of course, talking about other things like French politics was very enjoyable as well. Also, he was really good at reminding me how much progress I had made in my experiments when things were not going as fast as I would have liked. I am quite envious of the infectious joy you are able to share, and think it is your greatest power as an educator.

Thanks to Paul Urbach for being my promotor, providing me with suggestions of in which direction to take my research and helping me a lot with the mathematics in this thesis.

A large part of the nanofabrication I could not have done without the help of Anne Nurmohamed. You were always standing ready to help despite your very full agenda. I am very impressed by the amount of knowledge you have on nanofabrication and have learned a lot from you. You are a great teacher and I always enjoyed working together in the cleanroom.

Thanks to Carel Heerkens for providing me with some great ideas on how to tackle some of the nanofabrication challenges on how to actually make what I designed in the simulation software.

I would also like to thank Roald van der Kolk, as he has helped me a great deal with the nanofabrication part of my project. He was always very approachable and enthusiastic to help with all the instruments in the cleanroom. He has a great deal of knowledge and is happy to share it. Now that he is also working on his PhD, I wish him all the best.

Also thanks to Alex Heemels, my direct colleague on the FFSO project. You were a great help with getting started with the PhD and all the way throughout it. It always helped to vent our frustration with certain aspects of the PhD journey, but we could also have enough laughs. Thanks for your help, despite all your problems ;).

I want to thank Luuk Zonneveld, who became my lab mate around halfway into the PhD. It was nice to not always have to sit in the dark alone and be able to troubleshoot our experimental setups together.

Thanks to my office mates Thomas van der Sijs, Sven Weerdenburg and Dmytro Kolenov. I really enjoyed sharing an office together and having some good laughs. Even though some of Thomas' jokes were so bad it would make me wish it was the weekend already. Thanks in particular to Dmytro, who I had the pleasure of knowing even back when I was doing my Masters. You have given me some great pieces of advice over the years, and I hope I have been able to give you some in return as well.

Many thanks to the technical support staff, who were also of critical importance of the success of my PhD: Roland Horsten, Thomas Scholte and Thim Zuidwijk. Roland, beside the help with the electronic and software parts of the project (and your LabView enthusiasm), I believe you play an important part in all of the project of the (PhD) students in bringing the group together and always being there for students when they need someone to talk to. Thomas, thank you for the 3D prints you were able to create for my experimental setups. I am always amazed by your vast knowledge of 3D printing and your interest in analogue photography, you fit perfectly in the Optics cluster. Thanks to Thim for his great help with the optical setup for my experiments. It was great brainstorming together and also troubleshooting problems with the setup. I think I have learned a great deal from you regarding this over the time of my PhD.

Thanks to Lidija Nikolic for all her help with many of the administrative things that needed to be taken care of. I always enjoyed talking to you and have missed your positive energy when saying hi in the morning. I heard you are leaving the Optics cluster, which I think is a great loss. I wish you the best for your next endeavour.

Thanks to the (at the time) bachelor and master students Pieter van der Spek, Haoyang Yin, Jeroen van de Velde and Ekim Yildirim who have contributed to this thesis and my research through their Bachelor and Master projects.

Of course, many thanks to all the other people of the Optics grou... -ahem- cluster, with whom I had the pleasure of talking to and learning from. Everyone was always ready to help each other, which made it a really fun and stimulating environment to work in.

I also would like to thank everybody involved in the FFSO project. With the funding of NWO Perspectief Program (P15-36) it was possible for me to do this research. In addition, it was always really interesting to know what the other PhD students were working on. It was nice to visit some of the companies and learn from the people who work there. Thanks to the organization of the FFSO project, I was able to do research that I very much enjoyed.

Thanks to the Kavli staff who all together made it possible for me to make my nanostructure designs a reality in a safe way.

Thanks to my friends who provided me with the distractions that I sometimes needed and also for being there when I needed to vent some of my frustrations.

Thanks to my parents who made it possible for me to study physics in the first place and who have always encouraged and supported me to pursue my interests.

Finally, I would like to thank my girlfriend Liesbeth Veugen. You have supported me in so many ways, from the (almost) start until the end of my PhD journey. Being able to call you my girlfriend has been my greatest achievement.

LIST OF PUBLICATIONS

Papers

1. **T.P.S. Kotte**, A.J.L. Adam, T. Zuidwijk, C.T.H. Heerkens, M. Xu, and H.P. Urbach, *Broadband directional scattering through a phase difference acquired in composite nanoparticles*, [Optics Express Vol. 31 Issue 23](#), pp. 38815-38830 (2023).
2. **T.P.S. Kotte**, A. Nurmohamed, T. Zuidwijk, R. Horsten, and A.J.L. Adam, *Method for designing highly efficient composite transmission gratings*, [Journal of the Optical Society of America A Vol. 42 Issue 1](#), pp. 25-30 (2025).

Conference presentations

1. **T.P.S. Kotte**, A.J.L. Adam, and H.P. Urbach, *Directional scattering by dielectric core-semishell nanoparticles*, [European Optical Society Annual Meeting 2021, Rome, Italy](#). Oral presentation
2. **T.P.S. Kotte**, A.J.L. Adam, and H.P. Urbach, *Directional scattering by dielectric core-semishell nanoparticles*, [Face2Phase3 2022, Delft, the Netherlands](#). Poster presentation
3. **T.P.S. Kotte**, A.J.L. Adam, and H.P. Urbach, *Achieving directional scattering using SiO₂/Au nanoparticles*, [NWO Physics 2023, Veldhoven, the Netherlands](#). Poster presentation
4. **T.P.S. Kotte**, A.J.L. Adam, and H.P. Urbach, *Achieving directional scattering using SiO₂/Au nanoparticles*, [CLEO US 2023, San Jose, California, United States of America](#). Poster presentation
5. **T.P.S. Kotte**, A.J.L. Adam, and H.P. Urbach, *Directional scattering by composite SiO₂/Au nanoparticles*, [META 2023, Paris, France](#). Poster presentation
6. **T.P.S. Kotte**, A.J.L. Adam, and H.P. Urbach, *Highly efficient transmission diffraction grating through the use of composite elements*, [NNV-AMO annual meeting 2023, Egmond aan Zee, the Netherlands](#). Oral presentation

DATA AVAILABILITY

Models and measurement data used in this thesis ([Chapter 3](#) and [Chapter 5](#)) can be found at doi:

[10.4121/6ea07f88-0905-498a-a4a5-cb777edce069](https://doi.org/10.4121/6ea07f88-0905-498a-a4a5-cb777edce069).

Python code for the Monte Carlo simulations ([Chapter 6](#)) can be found at:

gitlab.tudelft.nl/optica/monte-carlo-scattering.

REFERENCES

- [1] N. Yu, P. Genevet, M. a. Kats, F. Aieta, J.-P. Tetienne, F. Capasso, and Z. Gaburro, *Light Propagation with Phase Discontinuities: Generalized Laws of Reflection and Refraction*, [Science](#) **334**, 333 (2011).
- [2] A. Arbabi and A. Faraon, *Advances in optical metalenses*, [Nature Photonics](#) **17**, 16 (2022).
- [3] S. Murai, M. A. Verschuuren, G. Lozano, G. Pirruccio, S. R. K. Rodriguez, and J. G. Rivas, *Hybrid plasmonic-photonic modes in diffractive arrays of nanoparticles coupled to light-emitting optical waveguides*, [Optics Express](#) **21**, 4250 (2013).
- [4] A. Nikitin, M. Remezani, and J. G. Rivas, *Luminescent Metamaterials for Solid State Lighting*, [ECS Journal of Solid State Science and Technology](#) **5**, R3164 (2016).
- [5] G. Perrakis, G. Kakavelakis, G. Kenanakis, C. Petridis, E. Stratakis, M. Kafesaki, and E. Kymakis, *Efficient and environmental-friendly perovskite solar cells via embedding plasmonic nanoparticles: an optical simulation study on realistic device architectures*, [Optics Express](#) **27**, 31144 (2019).
- [6] M. De, P. S. Ghosh, and V. M. Rotello, *Applications of nanoparticles in biology*, [Advanced Materials](#) **20**, 4225 (2008).
- [7] G. Guerrini, D. Magri, S. Gioria, D. Medaglini, and L. Calzolari, *Characterization of nanoparticles-based vaccines for COVID-19*, [Nature Nanotechnology](#) **17**, 570 (2022).
- [8] N. K. Ojha, G. V. Zyryanov, A. Majee, V. N. Charushin, O. N. Chupakhin, and S. Santra, *Copper nanoparticles as inexpensive and efficient catalyst: A valuable contribution in organic synthesis*, [Coordination Chemistry Reviews](#) **353**, 1 (2017).
- [9] C. Gaiher and A. Cavazos-Gaiher, *Physically Speaking: A Dictionary of Quotations on Physics and Astronomy* (Taylor & Francis, 1997).
- [10] A. Pors, M. Willatzen, O. Albrektsen, and S. I. Bozhevolnyi, *From plasmonic nanoantennas to split-ring resonators: tuning scattering strength*, [Journal of the Optical Society of America B](#) **27**, 1680 (2010).
- [11] T. Shegai, S. Chen, V. D. Miljković, G. Zengin, P. Johansson, and M. Käll, *A bimetallic nanoantenna for directional colour routing*, [Nature Communications](#) **2**, 481 (2011).
- [12] D. Vercruyse, Y. Sonnefraud, N. Verellen, F. B. Fuchs, G. Di Martino, L. Lagae, V. V. Moshchalkov, S. A. Maier, and P. Van Dorpe, *Unidirectional side scattering of light by a single-element nanoantenna*, [Nano Letters](#) **13**, 3843 (2013).

- [13] N. S. King, M. W. Knight, N. Large, A. M. Goodman, P. Nordlander, and N. J. Halas, *Orienting nanoantennas in three dimensions to control light scattering across a dielectric interface*, [Nano Letters](#) **13**, 5997 (2013).
- [14] A. E. Krasnok, C. R. Simovski, P. A. Belov, and Y. S. Kivshar, *Superdirective dielectric nanoantennas*, [Nanoscale](#) **6**, 7354 (2014).
- [15] C. Xu, K. Cheng, Q. Li, X. Shang, C. Wu, Z. Wei, X. Zhang, and H. Li, *The dual-frequency zero-backward scattering realized in a hybrid metallo-dielectric nanoantenna*, [AIP Advances](#) **9**, 075121 (2019).
- [16] N. Li, Y. Lai, S. H. Lam, H. Bai, L. Shao, and J. Wang, *Directional Control of Light with Nanoantennas*, [Advanced Optical Materials](#) **2001081**, 1 (2020).
- [17] X. Zhang, Q. Zhang, Y. Yuan, J. Liu, and X. Liu, *Ultra-directional forward scattering by a high refractive index dielectric T-shaped nanoantenna in the visible*, [Physics Letters, Section A: General, Atomic and Solid State Physics](#) **384**, 126696 (2020).
- [18] S. Campione, L. I. Basilio, L. K. Warne, and M. B. Sinclair, *Tailoring dielectric resonator geometries for directional scattering and Huygens' metasurfaces*, [Optics Express](#) **23**, 2293 (2015).
- [19] R. Verre, M. Svedendahl, N. O. Länk, Z. J. Yang, G. Zengin, T. J. Antosiewicz, and M. Käll, *Directional Light Extinction and Emission in a Metasurface of Tilted Plasmonic Nanopillars*, [Nano Letters](#) **16**, 98 (2016).
- [20] E. Arbabi, A. Arbabi, S. M. Kamali, Y. Horie, and A. Faraon, *Multiwavelength polarization-insensitive lenses based on dielectric metasurfaces with meta-molecules*, [Optica](#) **3**, 628 (2016).
- [21] I. Koirala, S.-S. Lee, and D.-Y. Choi, *Highly transmissive subtractive color filters based on an all-dielectric metasurface incorporating TiO₂ nanopillars*, [Optics Express](#) **26**, 18320 (2018).
- [22] V. Neder, Y. Ra'di, A. Alù, and A. Polman, *Combined Metagratings for Efficient Broad-Angle Scattering Metasurface*, [ACS Photonics](#) **6**, 1010 (2019).
- [23] W. Kim, G. Yoon, J. Kim, H. Jeong, Y. Kim, H. Choi, T. Badloe, J. Rho, and H. Lee, *Thermally-curable nanocomposite printing for the scalable manufacturing of dielectric metasurfaces*, [Microsystems and Nanoengineering](#) **8**, 73 (2022).
- [24] Z. Li, G. Geng, J. Cheng, W. Liu, S. Yu, B. Xie, H. Cheng, J. Li, W. Zhou, J. Tian, and S. Chen, *Flexible Confinement and Manipulation of Mie Resonances via Nano Rectangular Hollow Metasurfaces*, [Advanced Optical Materials](#) **2200185**, 2200185 (2022).
- [25] H. C. Van de Hulst, *Light scattering by small particles* (Dover Publications Inc., New York, 1981).
- [26] A. Zangwill, *Modern Electrodynamics* (Cambridge University Press, 2013).

- [27] J. Jackson, *Classical Electrodynamics*, 3rd ed. (Wiley, 1999).
- [28] T. A. Van Der Sijs, O. El Gawhary, and H. P. Urbach, *Electromagnetic scattering beyond the weak regime: Solving the problem of divergent Born perturbation series by Padé approximants*, *Physical Review Research* **2**, 1 (2020).
- [29] G. Mie, *Beiträge zur Optik trüber Medien, speziell kolloidaler Metallösungen*, *Annalen der Physik* **330**, 377 (1908).
- [30] C. F. Bohren and D. R. Huffman, *Absorption and scattering of light by small particles* (1983).
- [31] P. C. Waterman, *Matrix Formulation of Electromagnetic Scattering*, *Proceedings of the IEEE* **53**, 805 (1965).
- [32] P. C. Waterman, *New Formulation of Acoustic Scattering*, *The Journal of the Acoustical Society of America* **45**, 1417 (1969).
- [33] P. C. Waterman, *Symmetry, unitarity, and geometry in electromagnetic scattering*, *Physical Review D* **3**, 825 (1971).
- [34] L. Tsang, J. A. Kong, and R. T. Shin, *Theory of microwave remote sensing* (Wiley, New York, 1985).
- [35] P. Barber and C. Yeh, *Scattering of electromagnetic waves by arbitrarily shaped dielectric bodies*, *Applied Optics* **14**, 2864 (1975).
- [36] C. A. Balanis, *Advanced Engineering Electromagnetics* (Wiley, 1989).
- [37] I. Fernandez-Corbaton, S. Nanz, R. Alae, and C. Rockstuhl, *Exact dipolar moments of a localized electric current distribution*, *Optics Express* **23**, 33044 (2015).
- [38] R. Alae, C. Rockstuhl, and I. Fernandez-Corbaton, *An electromagnetic multipole expansion beyond the long-wavelength approximation*, *Optics Communications* **407**, 17 (2018).
- [39] R. Alae, C. Rockstuhl, and I. Fernandez-Corbaton, *Exact Multipolar Decompositions with Applications in Nanophotonics*, *Advanced Optical Materials* **7**, 1800783 (2019).
- [40] A. J. Devaney and E. Wolf, *Multipole expansions and plane wave representations of the electromagnetic field*, *Journal of Mathematical Physics* **15**, 234 (1974).
- [41] E. Whittaker, *On the partial differential equations of mathematical physics*, *Mathematische Annalen* **57**, 333 (1903).
- [42] A. B. Evlyukhin, C. Reinhardt, and B. N. Chichkov, *Multipole light scattering by nonspherical nanoparticles in the discrete dipole approximation*, *Physical Review B - Condensed Matter and Materials Physics* **84**, 235429 (2011).

- [43] A. B. Evlyukhin, C. Reinhardt, E. Evlyukhin, and B. N. Chichkov, *Multipole analysis of light scattering by arbitrary-shaped nanoparticles on a plane surface*, [*Journal of the Optical Society of America B* **30**, 2589 \(2013\)](#).
- [44] M. Kerker, D.-S. Wang, and C. L. Giles, *Electromagnetic scattering by magnetic spheres*, [*J. Opt. Soc. Am* **73**, 765 \(1983\)](#).
- [45] T. Kotte, A. Adam, T. Zuidwijk, C. Heerkens, M. Xu, and H. Urbach, *Broadband directional scattering through a phase difference acquired in composite nanoparticles*, [*Optics Express* **31**, 38815 \(2023\)](#).
- [46] T. Kotte, A. Nurmohamed, T. Zuidwijk, R. Horsten, and A. Adam, *Method for designing highly efficient composite transmission gratings*, [*Journal of the Optical Society of America A* **42**, 25 \(2025\)](#).
- [47] J. P. Camden, J. A. Dieringer, J. Zhao, and R. P. Van Duyne, *Controlled Plasmonic Nanostructures for Surface-Enhanced Spectroscopy and Sensing*, [*Accounts of Chemical Research* **41**, 1653 \(2008\)](#).
- [48] T. W. Odom and G. C. Schatz, *Introduction to Plasmonics*, [*Chemical Reviews* **111**, 3667 \(2011\)](#).
- [49] I. Staude and J. Schilling, *Metamaterial-inspired silicon nanophotonics*, [*Nature Photonics* **11**, 274 \(2017\)](#).
- [50] F. Cano-Renteria, M. Tegmark, M. Soljacic, J. D. Joannopoulos, J. Peurifoy, Y. Shen, L. Jing, Y. Yang, and B. G. DeLacy, *Nanophotonic particle simulation and inverse design using artificial neural networks*, in [*Physics and Simulation of Optoelectronic Devices XXVI*](#), June (SPIE, 2018) p. 6.
- [51] Y. Chen, S. Chen, T. M. Shih, J. Wang, W. Yang, L. Qian, and Z. Yang, *Broadband unidirectional scattering in visible ranges and controllable hot-spot spatial transfer via a single nanoparticle*, [*Applied Surface Science* **528**, 146489 \(2020\)](#).
- [52] K. Ladutenko, U. Pal, A. Rivera, and O. Peña-Rodríguez, *Mie calculation of electromagnetic near-field for a multilayered sphere*, [*Computer Physics Communications* **214**, 225 \(2017\)](#).
- [53] R. Fujimura, R. Zhang, Y. Kitamoto, M. Shimojo, and K. Kajikawa, *Modeling of semi-shell nanostructures formed by metal deposition on dielectric nanospheres and numerical evaluation of plasmonic properties*, [*Japanese Journal of Applied Physics* **53**, 035201 \(2014\)](#).
- [54] N. A. Mirin and N. J. Halas, *Light-bending nanoparticles*, [*Nano Letters* **9**, 1255 \(2009\)](#).
- [55] N. a. Mirin, a. A. Tamer, P. Nordlander, and N. J. Halas, *Perforated Semishells : Far-Field*, [*ACS nano* **4**, 2701 \(2010\)](#).

- [56] T. Hinamoto, H. Sugimoto, and M. Fujii, *Metal-Core/Dielectric-Shell/Metal-Cap Composite Nanoparticle for Upconversion Enhancement*, *Journal of Physical Chemistry C* **122**, 17465 (2018).
- [57] J. Ye, N. Verellen, W. Van Roy, L. Lagae, G. Maes, G. Borghs, and P. Van Dorpe, *Plasmonic modes of metallic semishells in a polymer film*, *ACS Nano* **4**, 1457 (2010).
- [58] M. B. Cortie, J. Giddings, and A. Dowd, *Optical properties and plasmon resonances of titanium nitride nanostructures*, *Nanotechnology* **21**, 115201 (2010).
- [59] F. Lütolf, M. Stalder, and O. J. F. Martin, *Up-scalable method to amplify the diffraction efficiency of simple gratings*, *Optics Letters* **39**, 6557 (2014).
- [60] K. Chatterjee, S. Sarkar, K. Jagajjanani Rao, and S. Paria, *Core/shell nanoparticles in biomedical applications*, *Advances in Colloid and Interface Science* **209**, 8 (2014).
- [61] R. Ghosh Chaudhuri and S. Paria, *Core/Shell Nanoparticles: Classes, Properties, Synthesis Mechanisms, Characterization, and Applications*, *Chemical Reviews* **112**, 2373 (2012).
- [62] S. Malynych, I. Luzinov, and G. Chumanov, *Poly(vinyl pyridine) as a universal surface modifier for immobilization of nanoparticles*, *Journal of Physical Chemistry B* **106**, 1280 (2002).
- [63] S. Kord and D. Kalai, *Synthesis of silica Janus nanoparticles with metal semishells*, Ph.D. thesis, Freie Universität Berlin (2018).
- [64] D. Mann, S. Voogt, R. Van Zandvoort, H. Keul, M. Möller, M. Verheijen, D. Nascimento-Duplat, M. Xu, H. P. Urbach, A. J. Adam, and P. Buskens, *Protecting patches in colloidal synthesis of Au semishells*, *Chemical Communications* **53**, 3898 (2017).
- [65] P. Van Dorpe and J. Ye, *Semishells: Versatile plasmonic nanoparticles*, *ACS Nano* **5**, 6774 (2011).
- [66] L. Chen, C. P. Deming, Y. Peng, P. Hu, J. Stofan, and S. Chen, *Gold core@silver semishell Janus nanoparticles prepared by interfacial etching*, *Nanoscale* **8**, 14565 (2016).
- [67] Y. Zhang, A. Barhoumi, J. B. Lassiter, and N. J. Halas, *Orientation-preserving transfer and directional light scattering from individual light-bending nanoparticles*, *Nano Letters* **11**, 1838 (2011).
- [68] J. Schmitt, A. Meier, U. Wallrabe, and E. Völklein, *Reactive ion etching (CF₄/Ar) and ion beam etching of various glasses for diffractive optical element fabrication*, *International Journal of Applied Glass Science* **9**, 499 (2018).
- [69] P. W. Leech, *Reactive ion etching of quartz and silica-based glasses in CF₄/CHF₃ plasmas*, *Vacuum* **55**, 191 (1999).

- [70] H. Du, J. Q. Xiao, Y. S. Zou, T. G. Wang, J. Gong, C. Sun, and L. S. Wen, *Optical properties of ultrathin aluminum films deposited by magnetron sputtering in visible band*, *Optical Materials* **28**, 944 (2006).
- [71] G. J. Lee, Y. P. Lee, B. Y. Jung, S. G. Jung, C. K. Hwangbo, J. H. Kim, and C. S. Yoon, *Microstructural and nonlinear optical properties of thin silver films near the optical percolation threshold*, *Journal of the Korean Physical Society* **51**, 1555 (2007).
- [72] H. Kangarlou and M. M. Aghgonbad, *Deposition-rate dependence of optical properties of titanium nanolayers*, *Ukrainian Journal of Physical Optics*, **4** (2012).
- [73] M. Zhou, Y. P. Li, S. Zhou, and D. Q. Liu, *Optical Properties and Surface Morphology of Thin Silver Films Deposited by Thermal Evaporation*, *Chinese Physics Letters* **32**, 077802 (2015).
- [74] D. I. Yakubovsky, A. V. Arsenin, Y. V. Stebunov, D. Y. Fedyanin, and V. S. Volkov, *Optical constants and structural properties of thin gold films*, *Optics Express* **25**, 25574 (2017).
- [75] M. Emami and R. Goodarzi, *Optoelectronic correlations for gold thin films in different annealing temperature*, *Optik* **171**, 397 (2018).
- [76] J. A. Taylor and S. B. Desu, *Interaction of Titanium with Silica After Rapid Thermal Annealing in Argon, Nitrogen, and Oxygen*, *Journal of the American Ceramic Society* **72**, 1947 (1989).
- [77] L. Y. Beliaev, E. Shkondin, A. V. Lavrinenko, and O. Takayama, *Optical properties of plasmonic titanium nitride thin films from ultraviolet to mid-infrared wavelengths deposited by pulsed-DC sputtering, thermal and plasma-enhanced atomic layer deposition*, *Optical Materials* **143**, 114237 (2023).
- [78] J. Chaves, *Introduction to Nonimaging Optics*, 2nd ed. (CRC Press, 2016).
- [79] R. Boyd, *Radiometry and the Detection of Optical Radiation* (John Wiley & Sons, 1983).
- [80] P. Van der Spek, *Light Transport in Scattering Media*, (2020).
- [81] E. Yildirim, *Monte-Carlo simulation of polarized photons scattering in volumes with half-shell nanoparticles*, (2022).
- [82] A. Vaskin, R. Kolkowski, A. F. Koenderink, and I. Staude, *Light-emitting metasurfaces*, *Nanophotonics* **8**, 1151 (2019).
- [83] A. Devilez, B. Stout, and N. Bonod, *Compact metallo-dielectric optical antenna for ultra directional and enhanced radiative emission*, *ACS Nano* **4**, 3390 (2010).
- [84] E. Rusak, I. Staude, M. Decker, J. Sautter, A. E. Miroshnichenko, D. A. Powell, D. N. Neshev, and Y. S. Kivshar, *Hybrid nanoantennas for directional emission enhancement*, *Applied Physics Letters* **105**, 221109 (2014).

- [85] J. Ho, Y. H. Fu, Z. Dong, R. Paniagua-Dominguez, E. H. Koay, Y. F. Yu, V. Valuckas, A. I. Kuznetsov, and J. K. Yang, *Highly directive hybrid metal-dielectric yagi-uda nanoantennas*, [ACS Nano](#) **12**, 8616 (2018).
- [86] M. Currie, M. A. Mastro, and V. D. Wheeler, *Characterizing the tunable refractive index of vanadium dioxide*, [Optical Materials Express](#) **7**, 1697 (2017).
- [87] H. P. Urbach, *Lecture notes Advanced Photonics*, (2020).
- [88] K. M. McPeak, S. V. Jayanti, S. J. Kress, S. Meyer, S. Iotti, A. Rossinelli, and D. J. Norris, *Plasmonic films can easily be better: Rules and recipes*, [ACS Photonics](#) **2**, 326 (2015).
- [89] I. H. Malitson, *Interspecimen Comparison of the Refractive Index of Fused Silica*, [Journal of the Optical Society of America](#) **55**, 1205 (1965).

CURRICULUM VITÆ

Thomas Pieter Sebastiaan KOTTE

19-06-1993 Born in Zwolle, the Netherlands.

EDUCATION

2005–2011 Secondary School (VWO)
Thorbecke Scholengemeenschap Zwolle

2011–2015 Bachelor Applied Physics
Delft University of Technology

2015–2018 Master Applied Physics
Delft University of Technology

WORK EXPERIENCE

2017–2018 Development Engineer
Research and Development
Anteryon

2018–2019 Design Engineer
D&E DUV Illumination, Sources and Dose Control
ASML

2019–2024 PhD candidate
Applied Sciences, ImPhys, Optics Research Group
Delft University of Technology

